A thesis for the degree of Doctor of Philosophy

Dual Symmetry Classification and $\mathbb{Z}_2$ Point-gap Topology in Non-Hermitian Systems

非エルミート系における双対対称性分類と $\mathbb{Z}_2$ ポイントギャップ・トポロジカル相

Zhiyu Jiang

Graduate School of Engineering

Hokkaido University

February, 2025

Contents

Chapter 1

Introduction

In condensed matter physics, the classification of phases has traditionally relied on Landau's symmetry-breaking theory [1, 2]. However, following the discovery of the quantum Hall effect in the 1980s [3], an entirely new framework for phase classification emerged, placing topological properties at the forefront of defining distinct phases [4–10]. A hallmark of such topological phases is that their physical properties are governed by global topological invariants, such as the Chern number in quantum Hall systems, which remains robust against local perturbations. Among the most canonical representatives of topological phases are topological insulators [11, 12], whose bulk remains insulating while their edges (or surfaces) host topologically protected conducting states. Such edge states are robust against impurity scattering, thereby ensuring effectively dissipationless transport.

In 2005, Kane and Mele proposed the quantum spin Hall (QSH) insulator [8, 9] by introducing time-reversal symmetric spin-orbit coupling between two Haldane models [6]. In QSH insulators, electrons of opposite spin propagate in opposite directions along the boundaries, forming Kramers-degenerate pairs of helical edge states. The topological nature of these states is characterized by a $\mathbb{Z}_2$ topological invariant. Shortly thereafter, the QSH insulator was experimentally realized in HgTe/CdTe quantum wells [13], providing one of the earliest direct experimental validations of topological insulators, thus solidifying the conceptual foundation of topological matter. In recent years, research has extended to three-dimensional topological insulators [14–17], and the exploration of topological phases has expanded across various platforms, including photonic crystals [18, 19], phononic systems [20, 21], and cold atomic systems [22, 23], significantly broadening the scope and impact of topological physics.

However, in realistic physical scenarios, systems are inevitably coupled to their external environment, thereby exhibiting the characteristics of open systems. In open systems, non-equilibrium phenomena such as particle inelastic scattering and gain-loss processes render the system's dynamics incompatible with traditional Hermitian Hamiltonian frameworks. Consequently, it becomes necessary to employ non-Hermitian Hamiltonians to accurately capture the underlying physics [24]. The study of non-Hermitian systems has gained significant attention in recent years, especially relating to topological phases [25]. The eigenenergies of non-Hermitian Hamiltonians generically become complex. For classical systems, non-Hermitian Hamiltonians are frequently employed to describe optical systems with gain and loss [26–31], topological circuit systems [32–38], etc. In open quantum systems, a non-Hermitian Hamiltonian can be used to describe the dynamics of a system without quantum jumps [39–42]. In such cases, the system follows the Schrödinger equation with a non-Hermitian Hamiltonian.

In Ref. [43], symmetry in non-Hermitian systems, which is important to the topological phases, has been studied by extending the symmetry relations for Hermitian Hamiltonians. Then, they showed that there are 38 symmetry classes in non-Hermitian systems. Furthermore, in non-Hermitian systems, the energy gaps can be classified into two types: line gaps and point gaps [43, 44]. On one hand, the topological invariant for the line gap is related to the number of edge states appearing in the gap through the bulk-boundary correspondence (BBC) in the same fashion in Hermitian systems.

On the other hand, the point gap is unique to non-Hermitian systems and $\mathbb{Z}$ topological invariant defined as the winding number in the complex energy plane for the system with periodic boundary conditions (PBC) predicts that spectra for the system with open boundary conditions (OBC) collapse into arcs within the closed curves of the PBC spectra. The corresponding eigenstates are localized near the open boundaries, known as the non-Hermitian skin effect (NHSE) [40, 45–63]. One of the famous examples is the Hatano-Nelson model [64–66]. It is also known that a system with spinful time-reversal symmetry exhibits $\mathbb{Z}_2$ topological invariant for the point gap [54]. This class of $\mathbb{Z}_2$ point-gap topology is fundamentally analogous to the $\mathbb{Z}_2$ topological phases characterizing the QSH insulator, and both are associated with Kramers-degenerate pairs. Within Hermitian systems, $\mathbb{Z}_2$ topological phases have been extensively investigated. For instance, the QSH insulator has played a pivotal role in advancing our understanding of topolog-

ical insulators [13, 14, 67–72], while Majorana fermions in $\mathbb{Z}_2$ topological superconductors have attracted considerable interest in quantum computational applications [73–77]. In contrast, the concept of $\mathbb{Z}_2$ point-gap topology in non-Hermitian systems was proposed only recently, leading to a limited body of theoretical work and, as yet, no experimental realizations.

Given the profound impact that $\mathbb{Z}_2$ topological phases have had in Hermitian systems, it is thus reasonable to anticipate that non-Hermitian $\mathbb{Z}_2$ topological phases will likewise possess considerable research value and potential applications. Consequently, this doctoral thesis seeks to undertake a theoretical exploration of $\mathbb{Z}_2$ point-gap topologies across various non-Hermitian systems, and to propose potential experimental schemes and practical applications.

The rest of this doctoral thesis is structured as follows. In Chapter 2, we introduce two frameworks for describing the evolution of open quantum systems: the Lindblad master equation and the non-Hermitian Hamiltonian formalism. In Chapters 3 and 4, we provide overviews of topological phases in closed (Hermitian) systems and open (non-Hermitian) systems, along with their respective symmetry classifications. The main results of this thesis are detailed in Chapters 5, 6, and 7. In Chapter 5, we extend the symmetry classification for non-Hermitian systems by unifying the classifications of Hamiltonians and time-evolution operators under the concept of dual symmetry classification, according to the fact that Hamiltonians and time-evolution operators lack clear mathematical distinctions in non-Hermitian systems. In Chapter 6, we define a nonunitary quantum walk characterized by $\mathbb{Z}_2$ point-gap topology based on the dual symmetry classification and investigate its topological and dynamical properties. In Chapter 7, we examine an application of the $\mathbb{Z}_2$ point-gap topology by analyzing the robustness of the $\mathbb{Z}_2$ topology in Hermitian systems under stacking. We propose a systematic explanation for this robustness by adopting a non-Hermitian perspective. We demonstrate that the observed topological behavior arises from level repulsion between Kramers pairs within a non-Hermitian framework. Finally, Chapter 8 gives a summary and outlook.

Chapter 2

Open Quantum Systems

2.1 Introduction

In most practical physical systems, almost all systems inevitably interact with their environment, leading to phenomena such as dissipation and decoherence. In such cases, the quantum system is referred to as an open quantum system, and the theoretical framework for closed quantum systems no longer applies. In this chapter, we introduce three important methods for describing open quantum systems: the quantum master equation, quantum trajectories, and non-Hermitian quantum mechanics, along with the close connections between these approaches.

2.2 Quantum master equation

In this section, we introduce the concepts of quantum states and density matrices from a systems-based perspective. Building on these concepts, we present a key method for describing the evolution of open quantum systems, known as the quantum master equation.

2.2.1 Density matrix

In quantum mechanics, a collection of quantum systems that are prepared under identical experimental conditions but may be in different quantum states is known as a quantum ensemble. If every system within the ensemble is in the state $|\psi\rangle$, the ensemble is referred to as a pure state ensemble. Conversely, if the systems are in various states $|\psi_i\rangle$, each with an associated probability p_i, the ensemble is called a mixed state ensemble. Thus, the state of a mixed state ensemble cannot be represented by a single state vector, whereas a pure state ensemble is simply a special

case of a mixed state ensemble. To effectively describe the state of an ensemble, the concept of the density matrix is introduced [78].

The density matrix for a pure state ensemble in the state $|\psi\rangle$ is defined as

$$\rho_{\mathrm{p}} = |\psi\rangle\langle\psi|, \tag{2.1}$$

while for a mixed state ensemble, it is given by

$$\rho_{\mathrm{m}} = \sum_i p_i \rho_i, \quad \rho_{\mathrm{i}} = |\psi_i\rangle\langle\psi_i|. \tag{2.2}$$

Here, p_i represents the probability of the state $|\psi_i\rangle$ occurring in the ensemble, and it satisfies $\sum_i p_i = 1$. The density matrix is a Hermitian operator ($\rho^\dagger = \rho$), and it exhibits semi-positivity ($\langle\psi|\rho|\psi\rangle \geq 0$) and unit trace ($\mathrm{Tr}\,\rho = 1$). An important distinction between the density matrices of pure and mixed states lies in the trace of the squared density matrix: a pure state satisfies $\mathrm{Tr}\,\rho^2 = 1$, whereas a mixed state satisfies $\mathrm{Tr}\,\rho^2 \leq 1$.

According to the density matrix, the expectation value of a given observable can be obtained. For a pure state system, the expectation value of an observable O is given by

$$\langle O\rangle = \langle\psi|O|\psi\rangle = \sum_n \langle\psi|n\rangle\langle n|O|\psi\rangle = \sum_n \langle n|O|\psi\rangle\langle\psi|n\rangle = \mathrm{Tr}\,(\rho_{\mathrm{p}} O), \tag{2.3}$$

whereas for a mixed state system, it is given by

$$\langle O\rangle = \mathrm{Tr}\,(\rho_{\mathrm{m}} O) = \mathrm{Tr}\,(\sum_i p_i |\psi_i\rangle\langle\psi_i|O) = \sum_i p_i \langle\psi_i|O|\psi_i\rangle = \sum_i p_i \langle O\rangle_i, \tag{2.4}$$

where $\langle O\rangle_i = \langle\psi_i|O|\psi_i\rangle$ represents the expectation value of the observable O in the pure state $|\psi_i\rangle$. Theoretically, if two systems share the same density matrix, all observable information obtainable from them will be identical.

When studying composite systems made up of multiple subsystems, we often only need to focus on the properties of observables in a particular subsystem. For instance, consider a system composed of two subsystems, A and B, with $\{\phi_i\}$ and $\{\chi_j\}$ being the basis vectors of subsystems A and B, respectively. If the density matrix of the composite system is ρ, then the density matrix

of subsystem A can be obtained by

$$\rho_A = \mathrm{Tr}_B\, \rho = \sum_n \langle \chi_j | \rho | \chi_j \rangle. \tag{2.5}$$

Here, ρ_A is referred to as the reduced density matrix of subsystem A [79, 80]. The expectation value of an observable O_A in subsystem A is then given by

$$\langle O_A \rangle = \mathrm{Tr}_A\, (\rho_A O). \tag{2.6}$$

2.2.2 Lindblad master equation

In general, a closed quantum system is always in a pure state, and its time evolution is described by the Schrödinger equation and the time evolution operator U. For convenience, we assume that the Hamiltonian of the system is time-independent:

$$i\hbar \frac{\partial}{\partial t} |\Psi(t)\rangle = H|\Psi(t)\rangle, \quad U = e^{-iHt}. \tag{2.7}$$

This evolution process is unitary. However, in reality, a truly "isolated system" does not exist, as nearly all systems inevitably interact with their environment, as shown in Fig. 2.1. A pure state ensemble, when interacting with its environment, undergoes energy dissipation and decoherence, often evolving into a mixed state ensemble. In this case, the evolution of the system state is no longer unitary and reversible. A commonly used approach to study the dynamical evolution of open systems is the quantum master equation method. The basic idea is to treat the system and environment as a closed system, whose state evolution follows the Schrödinger equation. By solving the Schrödinger equation, the state of the entire system at any given time can be determined. A partial trace can then be taken to eliminate the environmental degrees of freedom, allowing the state of the system of interest to be obtained.

The dynamics of open quantum systems can generally be divided into Markovian [81, 82] and non-Markovian processes [83]. A Markovian process is a memoryless dynamic process, where the timescale of the environment's memory and feedback is much shorter than that of the system's evolution. In contrast, in a non-Markovian process, information can flow back into the system during its interaction with the environment, causing the current dynamics to depend on the system's evolution history.

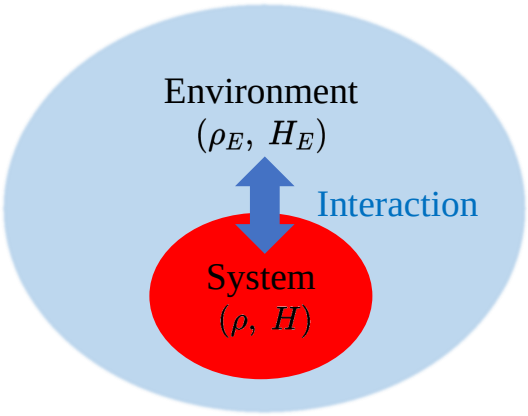

Figure 2.1: A schematic diagram of an open quantum system, showing the density matrix ρ and Hamiltonian H of both the system and environment, as well as their interaction.

In this section, we focus on the Markovian quantum master equation. By applying the Born approximation [84], Markov approximation [81, 82], and rotating wave approximation [85], one can derive the time evolution of the system's density operator ρ, known as the Lindblad master equation [82]:

$$\dot{\rho} = -i[H,\rho] + \sum_k \left(L_k \rho L_k^\dagger - \frac{1}{2}\left\{ L_k^\dagger L_k, \rho \right\} \right). \tag{2.8}$$

Here, the operator L_k is referred to as the Lindblad operator or quantum jump operator, representing the dissipative part of the system when interacting with the environment. The first term on the right side of the Lindblad-form quantum master equation is the unitary term, which describes the unitary evolution of the system in the absence of dissipation, while the remaining terms describe the nonunitary evolution of the system.

The Lindblad master equation is the most general form of a quantum dynamical equation that ensures complete positivity (the property that the density matrix remains positive semi-definite) and trace preservation (the trace of ρ remains 1), which are necessary for the physical consistency of the density matrix over time. Moreover, the Lindblad master equation has a wide range of applications across fields such as quantum optics [86–88], quantum information [89–95], condensed matter physics [96–98], and more. It is used to model phenomena like thermalization, decoherence, particle loss, and various interactions between a quantum system and its environment.

2.3 Quantum trajectory

Traditionally, open quantum systems are described by master equations, such as the Lindblad master equation, which describe the average evolution of the system's density matrix. In this section, we introduce an alternative theoretical framework for describing the dynamics of open quantum systems that examines the evolution of the system state from the perspective of stochastic processes, referred to as quantum trajectories.

To introduce the concept of quantum trajectories, we start with the Lindblad master equation [Eq. (2.8)]. By defining a non-Hermitian effective Hamiltonian:

$$H_{\text{eff}} = H - \frac{i}{2}\sum_k L_k^\dagger L_k, \tag{2.9}$$

the Lindblad master equation in Eq. (2.8) can be rewritten as

$$\dot{\rho} = -i\left(H_{\text{eff}}\rho - \rho H_{\text{eff}}^\dagger\right) + \sum_k L_k \rho L_k^\dagger. \tag{2.10}$$

In this expression, the first term on the right-hand side describes a nonunitary evolution governed by the effective Hamiltonian H_{eff}, while the second term represents the stochastic quantum jump.

In quantum trajectory theory, the system's evolution consists of both deterministic evolution and stochastic jumps [99, 100]. The deterministic evolution is governed by the non-Hermitian Hamiltonian H_{eff}. In the absence of any quantum jumps, the pure state $|\psi(t)\rangle$ of the system evolves according to the Schrödinger equation:

$$i\frac{d}{dt}|\psi(t)\rangle = H_{\text{eff}}|\psi(t)\rangle. \tag{2.11}$$

Because H_{eff} is non-Hermitian, the norm of the state vector is not conserved, meaning its magnitude changes over time. When the system interacts with the environment, it may undergoes sudden jump, described by:

$$|\psi(t)\rangle \to \frac{L_k|\psi(t)\rangle}{|L_k|\psi(t)\rangle|}, \tag{2.12}$$

where the probability density of a jump event is given by $\sum_k \langle\psi(t)|L_k^\dagger L_k|\psi(t)\rangle$.

As shown in Fig. 2.2, the system's state evolves smoothly under the non-Hermitian Hamiltonian H_{eff} until a stochastic quantum jump occurs, after which the state undergoes a sudden

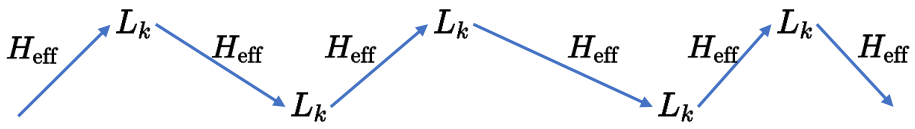

Figure 2.2: A schematic diagram of a single quantum trajectory of the quantum state $|\psi\rangle$, showing its evolution under a smooth non-Hermitian Hamiltonian H_{eff} before experiencing a stochastic quantum jump L_k.

transformation. This alternation between smooth evolution and stochastic jumps forms the complete quantum trajectory. By averaging over all possible quantum trajectories, one recovers the evolution of the density matrix ρ, which is governed by the Lindblad master equation.

To clarify this process, we consider a simple model of an optical cavity described by the Hamiltonian:

$$H_{\text{p}} = \hbar\omega a^\dagger a, \tag{2.13}$$

where ω represents the frequency of the cavity while $a^\dagger$ and a are the creation and annihilation operators, respectively.

In this model, a photon may occasionally escape from the cavity into the surrounding environment. This process can be phenomenologically described using the Lindblad operator:

$$L = a, \tag{2.14}$$

and the Lindblad master equation of such an open quantum system can be written as

$$\dot{\rho} = -i[H_{\text{p}}, \rho] + \kappa\left(2a\rho a^\dagger - \left\{a^\dagger a, \rho\right\}\right), \tag{2.15}$$

where κ represents the photon loss rate. Using Eq. (2.9), we can reformulate this master equation with an effective Hamiltonian:

$$H_{\text{p-eff}} = \left(\hbar\omega - i\frac{\kappa}{2}\right)a^\dagger a. \tag{2.16}$$

The reformulated dynamical equation is then written as:

$$\dot{\rho} = -i\left(H_{\text{p-eff}}\rho - \rho H_{\text{p-eff}}^\dagger\right) + \kappa a\rho a^\dagger. \tag{2.17}$$

The second term on the right-hand side is known as the quantum jump term. If the system is

initially in the Fock state $|n\rangle$ with n photons, the quantum jump term corresponds to the density matrix of a new state:

$$\rho' = |n'\rangle\langle n'|, \tag{2.18}$$

where

$$|n'\rangle = a|n\rangle = \sqrt{n}|n-1\rangle, \tag{2.19}$$

describes the process of photon loss. In other words, the system can be effectively described by the non-Hermitian Hamiltonian $H_{\text{p-eff}}$, following the Schrödinger equation when no photons escape to the environment.

The role of the non-Hermitian Hamiltonian is to introduce nonunitary effects that account for dissipation and decoherence before a jump occurs, which arise from the system's interaction with its environment. The non-Hermitian Hamiltonian H_{eff} acts as a bridge in quantum trajectory theory, linking the stochastic evolution of individual pure states to the overall evolution of the density matrix. Notably, if the timescale of interest is much shorter than the average time between quantum jumps, the dynamics of the open system can be effectively described by the non-Hermitian Hamiltonian and the Schrödinger equation. This approximation significantly simplifies the dynamical equations of open quantum systems, a topic that will be explained in detail in the next section.

2.4 Non-Hermitian quantum mechanics

In open quantum systems, interactions between the system and its external environment cause the system's evolution to be neither closed nor unitary. As discussed in Sec. 2.3, a non-Hermitian Hamiltonian can describe open quantum systems, provided the timescale is short enough to prevent quantum jumps.

Non-Hermitian quantum mechanics, an extension of traditional quantum mechanics, in which the Hamiltonian is not required to be Hermitian, has gained significant attention in recent years due to its potential for novel physical phenomena. Non-Hermitian quantum mechanics allows for Hamiltonians where $H^\dagger \neq H$, leading to complex energy spectra and enabling the description

of a broader range of physical phenomena, particularly those involving dissipation, gain, decoherence, and other effects that arise in open quantum systems. In this section, we introduce some fundamental concepts and properties of non-Hermitian systems.

2.4.1 Eigenstates of non-Hermitian Hamiltonian

In Hermitian systems, the eigenstates possess key properties such as orthogonality, normalization, and completeness. These properties ensure that the quantum states of the system can be expressed as linear combinations of the eigenstates, forming a complete basis. Unlike Hermitian systems, where these properties hold naturally, they require modifications in non-Hermitian systems due to their altered inner product structure. Instead, the concepts of orthogonality, normalization, and completeness are generalized and described using biorthogonality, bi-normalization, and bi-completeness.

Biorthogonality

In non-Hermitian systems, we typically define two distinct sets of eigenstates: right eigenstates $|\psi\rangle$ and left eigenstates $|\psi\rangle\rangle$, as they are not equivalent. These are defined as follows:

$$H|\psi_n\rangle = E_n|\psi_n\rangle, \quad \langle\psi_n|H^\dagger = E_n^*\langle\psi_n| \tag{2.20}$$

$$H^\dagger|\psi_n\rangle\rangle = E_n^*|\psi_n\rangle\rangle, \quad \langle\langle\psi_n|H = E_n\langle\langle\psi_n|. \tag{2.21}$$

Here, the right eigenstates $|\psi\rangle$ and left eigenstates $|\psi\rangle\rangle$ are generally not orthogonal to one another in the usual sense. Instead, they satisfy the biorthogonality condition:

$$\langle\langle\psi_m|\psi_n\rangle = 0 \quad (n \neq m). \tag{2.22}$$

This condition implies that the left and right eigenstates corresponding to different eigenvalues are orthogonal, similar to the orthogonality seen in Hermitian systems. However, the key difference is that this orthogonality occurs between the left and right eigenstates, rather than between eigenstates of the same type (i.e., either left or right eigenstates alone).

Bi-normalization

In non-Hermitian systems, both the right and left eigenstates can be normalized to ensure consistency, leading to the bi-normalization condition:

$$\langle\langle\psi_n|\psi_n\rangle = 1. \tag{2.23}$$

This condition ensures that the left and right eigenstates with the same eigenenergy E_n are properly scaled, analogous to the normalization applied to eigenstates in Hermitian systems. However, in non-Hermitian systems, both the left and right eigenstates must be normalized, rather than just a single set of states.

It is important to note that in non-Hermitian systems, the norm of the individual right eigenstates $|\psi\rangle$ or left eigenstates $|\psi\rangle\rangle$ may not be conserved during the system's evolution. However, the bi-normalization between the two sets ensures that the overall system's states remain properly normalized, preserving consistency in the description of the system's dynamics.

Bi-completeness

In Hermitian systems, completeness refers to the property that the eigenstates form a complete basis, allowing any state to be expressed as a linear combination of these eigenstates. In non-Hermitian systems, we have bi-completeness, which involves both the left and right eigenstates.

The bi-completeness condition is given by:

$$\sum_n |\psi_n\rangle\langle\langle\psi_n| = I. \tag{2.24}$$

This condition is analogous to the completeness property in Hermitian systems, but it requires contributions from both the right and left eigenstates. It ensures that any arbitrary state in the system can be expanded in terms of these biorthogonal eigenstates, maintaining the completeness of the basis in non-Hermitian quantum mechanics.

2.4.2 Dynamics of non-Hermitian systems

In non-Hermitian quantum mechanics, the Schrödinger equation remains unchanged, but the Hamiltonian is non-Hermitian. As a result, the eigenvalue E_n of the non-Hermitian Hamiltonian

is generally complex and can be expressed as $E_n = \varepsilon_n + i\gamma_n$, where ε_n and γ_n are real. The dynamics of the system is influenced by both the real and imaginary parts of E_n. The real part ε_n governs the oscillatory (or coherent) evolution of the quantum state, similar to what occurs in Hermitian systems, while the imaginary part γ_n controls the exponential growth or decay of the quantum state.

The nonunitary time evolution of an eigenstate $|\psi_n(t)\rangle$, associated with the eigenvalue E_n, behaves as:

$$|\psi_n(t)\rangle = e^{-iE_n t}|\psi_n(0)\rangle = e^{\gamma_n t}e^{-i\varepsilon_n t}|\psi_n(0)\rangle. \tag{2.25}$$

Here, $e^{\gamma_n t}$ introduces either exponential growth or decay, resulting in nonunitary time evolution and non-conservation of probability in the system. Consequently, the norm of the eigenstate is no longer conserved and can increase or decrease over time, depending on the imaginary part of the eigenvalue:

$$\langle\psi(t)|\psi(t)\rangle = e^{2\gamma_n t}\langle\psi(0)|\psi(0)\rangle. \tag{2.26}$$

This non-conservation of probability reflects the open nature of the system, where energy or particles can flow in or out, leading to gain or loss.

2.4.3 $\mathcal{PT}$ symmetry

In general, a non-Hermitian Hamiltonian typically has complex eigenvalues. However, its energy spectrum can remain real if the system possesses $\mathcal{PT}$ symmetry (Parity-Time symmetry) [101], which is a fundamental concept in non-Hermitian quantum mechanics. $\mathcal{PT}$ symmetry combines two operations: parity symmetry ($\mathcal{P}$) and time-reversal symmetry ($\mathcal{T}$).

The parity operator $\mathcal{P}$ reverses the spatial coordinates and satisfies the following condition:

$$\mathcal{P}H\mathcal{P}^{-1} = H, \tag{2.27}$$

where $\mathcal{P}$ is a unitary operator. The time-reversal operator reverses time and complex conjugates

all complex numbers. For time reversal:

$$\mathcal{T} H^* \mathcal{T}^{-1} = H, \tag{2.28}$$

where $\mathcal{T}$ is a unitary operator which obeys $\mathcal{T}\mathcal{T}^* = \pm 1$.

By defining an anti-unitary operator as the combination of the unitary $\mathcal{PT}$-symmetry operator and the complex conjugation operator $\mathcal{K}$, a $\mathcal{PT}$-symmetric Hamiltonian H remains invariant under the combined $\mathcal{PTK}$ operation:

$$(\mathcal{PTK}) H (\mathcal{PTK})^{-1} = H, \tag{2.29}$$

$$(\mathcal{PT}) H^* (\mathcal{PT})^{-1} = H. \tag{2.30}$$

If the anti-unitary operator $\mathcal{PTK}$ shares the same eigenstates as the Hamiltonian

$$\mathcal{PTK}|\psi_n\rangle = \lambda_n |\psi_n\rangle, \tag{2.31}$$

the eigenvalue becomes real.

Using the eigenvalue equation for the Hamiltonian and applying the $\mathcal{PT}$ operation, we get:

$$H\mathcal{PTK}|\psi_n\rangle = \mathcal{PTK} E_n |\psi_n\rangle. \tag{2.32}$$

Since the operator $\mathcal{K}$ reverses the sign of the imaginary part of the eigenvalue, we get

$$H\left(\mathcal{PTK}|\psi_n\rangle\right) = E_n^* \left(\mathcal{PTK}|\psi_n\rangle\right), \tag{2.33}$$

From Eq. (2.31), it follows that

$$H|\psi_n\rangle = E_n^* |\psi_n\rangle, \tag{2.34}$$

indicating the eigenenergies $E_n = E_n^*$ are real, provided the $\mathcal{PT}$ symmetry is preserved.

$\mathcal{PT}$ symmetry is often used to describe physical systems with balanced gain and loss, providing a framework for describing non-Hermitian quantum systems where the energy spectrum can remain real, similar to Hermitian systems, as long as the $\mathcal{PT}$ symmetry is unbroken. However, when $\mathcal{PT}$ symmetry is broken, the energy spectrum becomes complex, leading to gain and loss

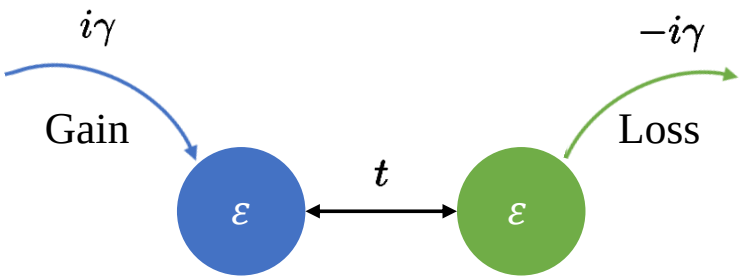

Figure 2.3: A schematic diagram of the $\mathcal{PT}$-symmetric system, with its Hamiltonian given in Eq. 2.35. The system exhibits a balance between in-coming and out-going energy.

effects. As an example, we consider a $\mathcal{PT}$ symmetric non-Hermitian Hamiltonian, expressed as

$$H = \begin{pmatrix} \varepsilon + i\gamma & t \\ t & \varepsilon - i\gamma \end{pmatrix}. \tag{2.35}$$

The $\mathcal{PT}$ operator can be written as

$$\mathcal{PT} = \begin{pmatrix} 0 & 1 \\ 1 & 0 \end{pmatrix}, \tag{2.36}$$

As shown in Fig. 2.3, the gain and loss of the system from the environment are balanced, resulting in the conservation of the system's energy.

The $\mathcal{PT}$ symmetry has important applications in various fields, including quantum optics [102–104], acoustics [105, 106], electronic circuits [107, 108], and other systems where non-Hermitian dynamics, such as dissipation or amplification, are present. For example, in optical systems, $\mathcal{PT}$-symmetric structures can be designed to control light propagation with balanced gain and loss, enabling unique behaviors such as unidirectional light transport and enhanced sensing [102].

2.4.4 Exceptional points

Exceptional points (EPs) in non-Hermitian systems refer to special degeneracies where two or more eigenvalues and their corresponding eigenstates coalesce. Different from standard degeneracies in Hermitian systems, where eigenvalues can become degenerate while their eigenstates remain linearly independent, at EPs, both the eigenvalues and eigenstates merge. We consider

the non-Hermitian Hamiltonian introduced in Eq. (2.35). The eigenvalues can be solved as

$$E_{\pm} = \varepsilon \pm \sqrt{t^2 - \gamma^2}, \tag{2.37}$$

and the eigenenergies become degenerate when $t = \pm\gamma$. In the case of $t = \gamma$, according to the characteristic equation,

$$\begin{pmatrix} i & 1 \\ 1 & -i \end{pmatrix} \begin{pmatrix} c_1 \\ c_2 \end{pmatrix} = 0. \tag{2.38}$$

the solution for both eigenstates is

$$(c_1, c_2) \propto (i, 1). \tag{2.39}$$

This means that at the non-Hermitian degeneracy point, not only do the eigenenergies degenerate, but the eigenstates also coalesce into the same state. Moreover, after applying a transformation to the matrix in Eq. 2.38,

$$\begin{pmatrix} i & 1 \\ 1 & 0 \end{pmatrix}^{-1} \begin{pmatrix} i & 1 \\ 1 & -i \end{pmatrix} \begin{pmatrix} i & 1 \\ 1 & 0 \end{pmatrix} = \begin{pmatrix} 0 & 1 \\ 0 & 0 \end{pmatrix}, \tag{2.40}$$

we obtain a Jordan block structure, indicating that the Hamiltonian at such an EP is no longer diagonalizable.

Additionally, EPs exhibit unique mathematical [109], dynamical [110], and topological properties [111], including the breakdown of adiabatic evolution, mode switching, and enhanced sensitivity to gain and loss. EPs have applications in various fields, particularly in optical, acoustic, and electronic systems, where they can be exploited for high-precision sensing [104, 112] and non-reciprocal signal transmission [113–116]. The study of EPs provides deep insights into the topological structure of non-Hermitian systems, making them a key area of research in modern physics.

Chapter 3

Topological Phases in Closed Quantum Systems

3.1 Introduction

The traditional understanding of the phases of matter is based on the concept of symmetry breaking. According to the Landau theory of phase transitions, phases are primarily classified by the way symmetries are broken in the system's ground state [1, 2]. For example, in a ferromagnet, when atomic spins align in one direction, the system's rotational symmetry is broken, resulting in the ferromagnetic (FM) phase [117–119]. Similarly, superconductors and crystals exhibit the breaking of gauge symmetry and translational symmetry, respectively [120]. In this framework, local order parameters are typically used to describe different phases. For instance, magnetization is an order parameter for ferromagnets [118], and the density wave is an order parameter for crystals [121].

The discovery of the quantum Hall effect in 1980 by Klaus von Klitzing revealed that not all phases can be explained solely by local symmetry breaking. He observed that a two-dimensional electron gas in a strong magnetic field exhibits quantized Hall conductance at low temperatures, despite the absence of symmetry breaking [3]. It was soon realized that this quantized conductance could be explained using a topological invariant known as the Chern number [122]. Unlike local order parameters, the Chern number characterizes the global properties of the system. The integer nature of the Hall conductance is directly linked to the Chern number, a topological property that remains unchanged as long as the system's topology is preserved. This discovery, which

introduced new phases of matter governed by global topological properties rather than local order parameters, was a major breakthrough in the understanding of topological phases.

In this chapter, we mainly introduce the basic concepts and theories of topological phases in a closed system, including Bloch band theory (Sec. 3.2), Berry phase (Sec. 3.3), topological invariants (Sec. 3.4), as well as important topological properties such as bulk-boundary correspondence (Sec. 3.5). Finally, we discuss the symmetries and the 10-fold classification of Hermitian Hamiltonians, also known as the Altland-Zirnbauer (AZ) classification in Sec. 3.6.

3.2 Bloch band theory

Band theory is a fundamental framework for studying the behavior of electron motion and energy levels in solids [123]. Developed from quantum mechanics, it provides a theoretical basis for understanding the energy levels and physical properties of crystalline systems [124–126]. Band theory establishes the basic principles of electron motion in crystals and, through the analysis of energy level structures, reveals the microscopic mechanisms underlying the properties of conductors, insulators, and other materials. This has greatly advanced the development and application of semiconductor theory. Furthermore, the emergence of topological band theory, building on this foundation, has become a crucial tool for discovering and studying new topological systems and analyzing novel topological materials.

A Bloch wave (or Bloch state) refers to the wavefunction of an electron moving in a periodic potential field. In a lattice with a periodic structure, the wave's propagation is influenced by the periodic potential of the lattice, $V(\boldsymbol{r}+\boldsymbol{R}) = V(\boldsymbol{R})$, where $\boldsymbol{R}$ represents a lattice vector. This periodic potential leads to the Hamiltonian $h(\boldsymbol{r}) = h(\boldsymbol{r}+\boldsymbol{R})$ also varies periodically. The eigenstates of these systems can be expressed using Bloch functions, as

$$\psi_{n,\boldsymbol{k}}(\boldsymbol{r}) = u_{n,\boldsymbol{k}}(\boldsymbol{r})e^{i\boldsymbol{k}\cdot\boldsymbol{r}}. \tag{3.1}$$

Here, n represents the band index, while $\boldsymbol{k}$ denotes the crystal momentum. The wavefunction $u_{n,\boldsymbol{k}}$ inherits the periodicity of the lattice, satisfying $u_{n,\boldsymbol{k}}(\boldsymbol{r}) = u_{n,\boldsymbol{k}}(\boldsymbol{r}+\boldsymbol{R})$. This wavefunction serves as the eigenstate of $H(\boldsymbol{k}) = e^{-i\boldsymbol{k}\cdot\boldsymbol{r}}h(\boldsymbol{r})e^{i\boldsymbol{k}\cdot\boldsymbol{r}}$, and its eigenvalue satisfies $E_n(\boldsymbol{k}) = E_n(\boldsymbol{k}+\boldsymbol{K})$, where $\boldsymbol{K}$ denotes the reciprocal lattice vector. $E_n(\boldsymbol{k})$ associated with the band index n varies continuously

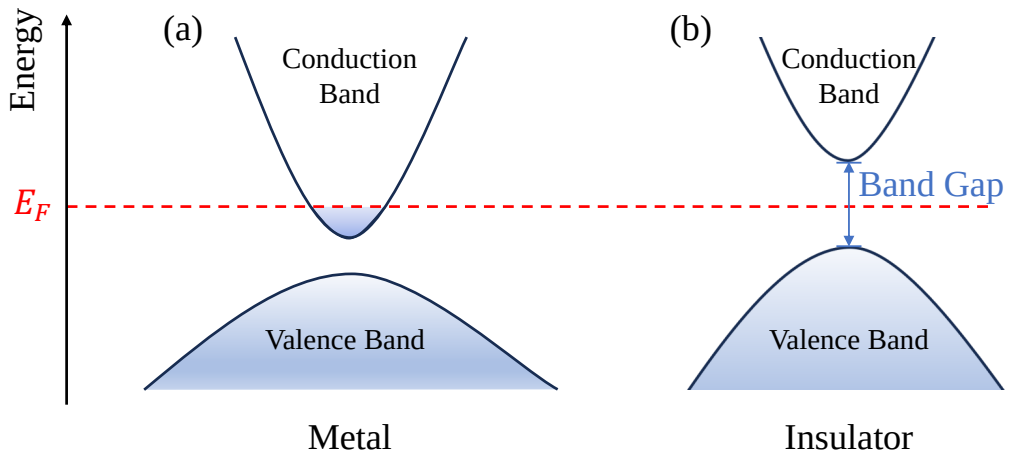

Figure 3.1: A schematic diagram of (a) metals and (b) insulators from the perspective of band theory. Here, E_F represents the Fermi energy.

with the wavevector $\boldsymbol{k}$, forming energy bands characterized by n. For a given n, the eigenvalues are periodic with respect to $\boldsymbol{k}$.

Bloch's theorem expresses this periodicity mathematically as:

$$\psi_{n,\boldsymbol{k}}(\boldsymbol{r}+\boldsymbol{R}) = \psi_{n,\boldsymbol{k}}(\boldsymbol{r})e^{i\boldsymbol{k}\cdot\boldsymbol{R}}, \tag{3.2}$$

indicating that the difference between the wavefunctions at positions $\boldsymbol{r}$ and $\boldsymbol{r}+\boldsymbol{R}$ is only a phase factor $e^{i\boldsymbol{k}\cdot\boldsymbol{r}}$. Bloch's theorem tells us that in a crystalline system with a periodic potential field, the wavefunction of the electrons also exhibits periodicity. It can be viewed as a plane wave whose amplitude is periodically modulated by the structure of the lattice.

According to the Pauli exclusion principle, each quantum state can be occupied by at most one electron. Electrons tend to fill the lowest available energy states first, creating an "electron sea" with a finite electron density. Depending on how the electrons occupy these states, energy bands are classified into valence bands (fully filled) and conduction bands (partially filled). The gap between the conduction and valence bands, where no electron states are present, is known as the band gap, and its size is referred to as the energy gap.

Materials can be classified as metals or insulators based on whether electronic states cross the Fermi energy E_F, which corresponds to the energy of the highest occupied state at zero temperature. As illustrated in Fig. 3.1, in typical metals, the Fermi energy lies within a partially filled energy band, meaning there exist available electronic states arbitrarily close to E_F. This

allows electrons to be easily excited within the same band under an external perturbation, leading to electrical conductivity. In contrast, insulators have a finite energy gap between the highest occupied (valence) band and the lowest unoccupied (conduction) band, preventing low-energy excitations and thus inhibiting electrical conductivity.

3.3 Berry phase

In topological band theory, the Berry phase is a crucial concept [122, 127–130]. In quantum mechanics, when the Hamiltonian of a system changes slowly, the quantum state of the system undergoes adiabatic evolution. According to the quantum adiabatic theorem, if the system initially starts in a particular eigenstate, it will remain in the instantaneous eigenstate throughout the evolution. However, when the system undergoes evolution along a closed path, the final quantum state acquires not only the usual dynamical phase but also an additional geometric phase known as the Berry phase. Unlike the conventional dynamical phase, the Berry phase depends on the evolution path of the system rather than the time. Below, we provide the expression for the Berry phase when the Hamiltonian undergoes adiabatic periodic changes.

We consider a Hamiltonian H that depends on a parameter vector $\boldsymbol{R} = (R_1, R_2, ...)$, which changes slowly over time, such that $\boldsymbol{R} = \boldsymbol{R}(t)$. The term "slowly" has two important implications in this context. First, it means that the change is slow enough so that, at any given moment, we can still identify a set of orthogonal and complete eigenstates for the system's Hamiltonian $H(\boldsymbol{R}(t))$:

$$H(\boldsymbol{R}(t))|n(\boldsymbol{R}(t))\rangle = \varepsilon_n(\boldsymbol{R}(t))|n(\boldsymbol{R}(t))\rangle. \tag{3.3}$$

Second, the "slowly" changing nature of $\boldsymbol{R}(t)$ ensures that the adiabatic approximation holds. This means the system remains in the same eigenstate $|n(\boldsymbol{R})\rangle$ throughout the evolution, without "jumping" to a different eigenstate associated with another band index n'.

We assume that the initial state at time $t = 0$ is $|n(\boldsymbol{R}(0))\rangle$. The state at time t denoted by $\psi_n(t)$, can be expressed as the eigenstate $|n(\boldsymbol{R}(t))\rangle$ multiplied by a phase factor:

$$|\psi_n(t)\rangle = e^{i\gamma_n(t)}\exp\left[-i\int_0^t dt'\varepsilon_n(\boldsymbol{R}(t'))\right]|n(\boldsymbol{R}(0))\rangle. \tag{3.4}$$

Here, the phase term can be divided into two parts: the first part, $e^{i\gamma_n(t)}$, is of primary interest to us, while the second part, $\exp\left[-i\int_0^t dt'\varepsilon_n(\boldsymbol{R}(t'))\right]$, is known as the dynamical phase factor. Substituting $|\psi_n(t)\rangle$ into the time-dependent Schrödinger equation

$$i\frac{\partial}{\partial t}|\psi_n(t)\rangle = H\left(\boldsymbol{R}(t)\right)|\psi_n(t)\rangle \tag{3.5}$$

and left-multiplying by $\langle n(\boldsymbol{R}(t))|$, using $\langle n(\boldsymbol{R}(t))|\boldsymbol{R}(t)\rangle = 1$ and Eq. (3.3), we find that γ_n satisfies:

$$\gamma_n(t) = i\int_0^t dt'\langle n(\boldsymbol{R}(t'))|\frac{d}{dt'}|\boldsymbol{R}(t')\rangle = i\int_{\boldsymbol{R}(0)}^{\boldsymbol{R}(t)} d\boldsymbol{R}\langle n(\boldsymbol{R})|\nabla_{\boldsymbol{R}}|n(\boldsymbol{R})\rangle. \tag{3.6}$$

Assuming that the system's evolution corresponds to a path C in parameter space $\boldsymbol{R} = (R_1, R_2, ...)$, the corresponding integral becomes a path integral:

$$\gamma_n = \int_C d\boldsymbol{R}\mathcal{A}_n(\boldsymbol{R}), \tag{3.7}$$

where

$$\mathcal{A}_n(\boldsymbol{R}) = i\langle n(\boldsymbol{R})|\nabla_{\boldsymbol{R}}|n(\boldsymbol{R})\rangle \tag{3.8}$$

is known as the Berry connection or Berry potential. It is important to note that the Berry connection depends on the choice of gauge. If a gauge transformation $|n(\boldsymbol{R})\rangle \to e^{-\zeta(\boldsymbol{R})}|n(\boldsymbol{R})\rangle$ is applied to the basis we initially chose, the Berry connection will change as follows:

$$\mathcal{A}_n(\boldsymbol{R}) \to \mathcal{A}_n(\boldsymbol{R}) - \frac{\partial}{\partial \boldsymbol{R}}\zeta(\boldsymbol{R}), \tag{3.9}$$

and the change in γ_n due to this gauge transformation can be expressed as $\zeta(\boldsymbol{R}(0))-\zeta(\boldsymbol{R}(T))$. If the evolution of the Hamiltonian in parameter space follows a closed loop and exhibits periodicity, then after a time T, we have $\boldsymbol{R}(0) = \boldsymbol{R}(T)$. Under these conditions, when a gauge transformation is applied, the single-valuedness of the wave function requires that:

$$\zeta(\boldsymbol{R}(0)) - \zeta(\boldsymbol{R}(T)) = 2m\pi, \tag{3.10}$$

where m is an integer. As a result, for a closed path C, γ_n is gauge-invariant and is known as the

Berry phase:

$$\gamma_n = \oint_C d\boldsymbol{R}\mathcal{A}_n(\boldsymbol{R}). \tag{3.11}$$

By applying Stokes' theorem, the Berry phase can be expressed as a surface integral over a surface S bounded by the path C:

$$\gamma_n = \int_S d\boldsymbol{S} \cdot \boldsymbol{\Omega}^{(n)}(\boldsymbol{R}), \tag{3.12}$$

where $\boldsymbol{\Omega}^{(n)}(\boldsymbol{R}) = \nabla_{\boldsymbol{R}} \times \boldsymbol{A}_n(\boldsymbol{R})$ is known as the Berry curvature. In component form, the Berry curvature can be written as:

$$\boldsymbol{\Omega}^{(n)}_{\mu\nu} = \partial_\mu(\boldsymbol{A}_n)_\nu - \partial_\nu(\boldsymbol{A}_n)_\mu \tag{3.13}$$

$$= i(\langle\partial_\mu u_n(\boldsymbol{R})|\partial_\nu u_n(\boldsymbol{R})\rangle - \langle\partial_\nu u_n(\boldsymbol{R})|\partial_\mu u_n(\boldsymbol{R})\rangle), \tag{3.14}$$

where ∂_μ denotes $\partial/\partial\boldsymbol{R}_\mu$. Using the completeness relation, $\sum_n |u_n(\boldsymbol{R})\rangle\langle u_n(\boldsymbol{R})| = 1$, and identity:

$$\langle u_m(\mathbf{R})|\,\nabla_{\mathbf{R}}\,|u_n(\mathbf{R})\rangle = \frac{\langle u_m(\mathbf{R})|\,\nabla_{\mathbf{R}} H(\mathbf{R})\mid u_n(\mathbf{R})\rangle}{E_n - E_m} \quad (m \neq n), \tag{3.15}$$

the Berry curvature can also be expressed in the following alternative form:

$$\boldsymbol{\Omega}^{(n)} = \mathrm{Im}\sum_{m\neq n} \frac{\langle u_n(\mathbf{R})|\,\nabla_{\mathbf{R}} H(\mathbf{R})\,|u_m(\mathbf{R})\rangle \times \langle u_m(\mathbf{R})|\,\nabla_{\mathbf{R}} H(\mathbf{R})\,|u_n(\mathbf{R})\rangle}{(E_n - E_m)^2}. \tag{3.16}$$

The introduction to the Berry phase above is based on the periodic variation of the Hamiltonian over time. In crystalline systems, the Hamiltonian in momentum space also exhibits a periodic form, meaning it changes periodically with crystal momentum $\boldsymbol{k}$. This periodicity in $\boldsymbol{k}$ can be seen as analogous to the periodicity in time, allowing the definition of a Berry phase in momentum space, known as the Zak phase. In this context, the Berry phase over a Brillouin zone can be expressed as:

$$\gamma_n = \oint_{\mathrm{BZ}} d\boldsymbol{k} \cdot \langle u_n(\boldsymbol{k})|i\nabla_{\boldsymbol{k}}|u_n(\boldsymbol{k})\rangle. \tag{3.17}$$

On the Bloch band, the Berry curvature is defined as

$$\boldsymbol{\Omega}^{(n)}(\boldsymbol{k}) = \nabla_{\boldsymbol{k}} \times \langle u_n(\boldsymbol{k})|i\nabla_{\boldsymbol{k}}|u_n(\boldsymbol{k})\rangle. \tag{3.18}$$

Since the points $\boldsymbol{k}$ and $\boldsymbol{k}+\boldsymbol{K}$ (where $\boldsymbol{K}$ is a reciprocal lattice vector) are equivalent in the Brillouin zone, sweeping k across the entire Brillouin zone can be viewed as a closed path. The integral of the Berry curvature over a closed surface yields a quantized integer known as the Chern number, which serves as a topological invariant that characterizes topological systems.

The Berry phase is often referred to as a geometric phase because it depends solely on the geometric properties of the parameter path. This geometric or topological invariance is a fundamental aspect in physics, playing a crucial role in phenomena such as the quantum Hall effect, topological insulators, topological order, and topological quantum computing. These topological phases are robust against local perturbations, making them significant for understanding and developing new materials and technologies in condensed matter physics.

3.4 Topological invariant

In topological physics, topological invariants are quantities used to describe and distinguish different topological phases in quantum systems, playing a crucial role in various applications. Different topological invariants help us understand the properties of quantum Hall effects, topological insulators, topological superconductors, and other topological materials. These invariants remain unchanged when system parameters change continuously without a phase transition, making them essential tools for studying the robustness of topological phases. Common topological invariants include the winding number [131–135], TKNN number [122, 136–138] (or Chern number [12, 122, 129]), etc. In this section, we will briefly introduce some of the topological invariants that will be used in this thesis.

3.4.1 Winding number

Mathematically, the winding number describes the total number of times a closed curve winds around a fixed point on a plane. The sign of the winding number depends on the direction of the winding: if the curve winds counterclockwise around the fixed point, the winding number is a positive integer, as shown in Fig. 3.2(d-f); if it winds clockwise, the winding number is a negative integer, as shown in Fig. 3.2(a,b). If the curve does not enclose the fixed point, the winding number is zero, as shown in Fig. 3.2(c). In topological physics, the winding number

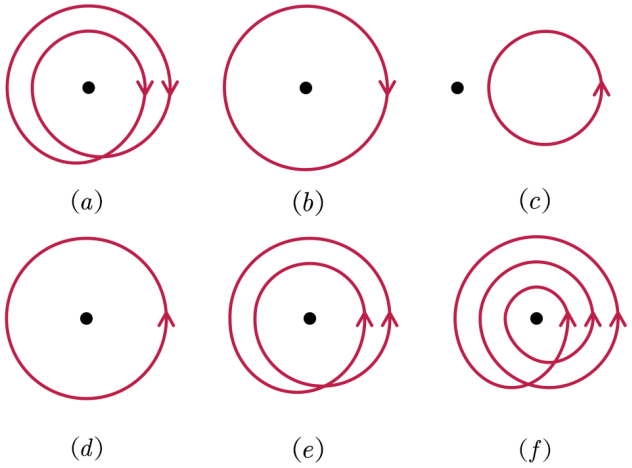

Figure 3.2: The winding number is the total number of times a closed curve in the plane winds around a given point, and it is always an integer (Figure from WIKIPEDIA). The winding numbers for (a) to (f) are -2, -1, 0, 1, 2, and 3, respectively.

is a $\mathbb{Z}$ topological invariant that is commonly used to describe the topological properties of odd-dimensional systems. To illustrate the specific characteristics of the winding number, we consider a one-dimensional two-band system.

For a one-dimensional two-band system, the Hamiltonian in momentum space can always be expressed as a two-dimensional matrix, whose generators are the Pauli matrices. The Hamiltonian is given by:

$$H = \boldsymbol{h}(k) \cdot \boldsymbol{\sigma} = \begin{pmatrix} h_z(k) & h_x(k) - ih_y(k) \\ h_x(k) + ih_y(k) & -h_z(k) \end{pmatrix}, \tag{3.19}$$

where $\boldsymbol{h}(k) = \big(h_x(k), h_y(k), h_z(k)\big)^T$ is a vector function of the wavevector k, and $\boldsymbol{\sigma} = (\sigma_x, \sigma_y, \sigma_z)$ are the Pauli matrices. The dispersion relation of the system is given by

$$E_\pm = \pm\sqrt{h_x^2(k) + h_y^2(k) + h_z^2(k)}, \tag{3.20}$$

while the corresponding eigenstates are:

$$\psi_\pm = \frac{1}{\mathcal{N}_\pm} \begin{pmatrix} h_z(k) + E_\pm \\ h_x(k) - ih_y(k) \end{pmatrix}, \tag{3.21}$$

where $\mathcal{N}_\pm$ is a normalization constant.

Now, we consider the case where the component $h_z(k) = 0$. In this situation, the wavefunction is given by:

$$\psi_{\pm} = \frac{1}{\sqrt{2}} \begin{pmatrix} \pm 1 \\ \hat{h}^*(k) \end{pmatrix}, \quad \hat{h}(k) \equiv \frac{h(k)}{|h(k)|}, \tag{3.22}$$

where $h(k) = h_x(k) + ih_y(k)$ represents one of the off-diagonal elements of the Hamiltonian.

According to Eq. (3.17), the Berry phase of the system can be obtained by

$$\gamma(C) = \oint_C dk\, A(k), \tag{3.23}$$

where the Berry connection

$$A(k) = i\langle \psi_- | \partial_k | \psi_- \rangle, \tag{3.24}$$

so that

$$\gamma(C) = \frac{i}{2} \oint_C dk \langle \psi_- | \partial_k | \psi_- \rangle = i \oint_C \hat{h}(k) \partial_k \hat{h}^*(k) dk. \tag{3.25}$$

The normalized $\hat{h}(k)$ obeys $\hat{h}(k)\hat{h}^*(k) = 1$, allowing the Berry phase to be written as:

$$\gamma = \frac{i}{2} \oint_C \frac{d\hat{h}^*(k)}{\hat{h}^*(k)} = \frac{i}{2} \oint_C \frac{d\hat{h}(k)}{\hat{h}(k)}. \tag{3.26}$$

In one-dimensional systems, the Berry connection has only one component, enabling the definition of the winding number as:

$$w = \frac{1}{2\pi i} \oint_C \frac{d\hat{h}(k)}{\hat{h}(k)}. \tag{3.27}$$

We can understand the meaning of the winding number from a mathematical perspective. For a Hamiltonian without diagonal elements ($h_z(x) = 0$), the vector representing the Hamiltonian has only two components, $\boldsymbol{h}(k) = \left(h_x(k), h_y(k), 0\right)^T$. The matrix elements corresponding to the Pauli matrix σ_y contain imaginary parts. This allows the Hamiltonian to be mapped onto the complex plane, where the x-axis and y-axis correspond to the components $h_x(k)$ and $h_y(k)$ of the Hamiltonian, respectively. In this case, the number of times that the curve C winds around the

origin point is given by

$$W = \frac{1}{2\pi i} \oint_C \frac{dh}{h}, \tag{3.28}$$

which corresponds precisely to the winding number.

Such coincidence can be understood from a physical perspective. For points where the energy gap opens and closes (in this model, corresponds to the original point), these points are non-analytic. As the momentum k sweeps across the entire Brillouin zone, the integration path on the complex plane forms a closed circle, with its specific shape and size determined by the model and parameters. If the closed circle does not enclose a singularity, the integral value is zero, indicating that the system is topologically trivial. However, if the circle encloses a singularity, the integral yields a non-zero integer, indicating that the system is topologically nontrivial. This understanding leads to an alternative formula for calculating the winding number:

$$w = \frac{1}{2\pi i} \int_0^{2\pi} dk \frac{d}{dk} \log h(k), \tag{3.29}$$

where

$$\log h(k) = \log \left(|h(k)| e^{i\phi(k)} \right) = \log |h(k)| + i\phi(k). \tag{3.30}$$

Here, $\phi(k)$ is the argument of $h(k)$. In the contour integral on the complex plane, the term $\log |h(k)|$ does not contribute, while the term $i\phi(k)$ represents the angle around the singularity. Consequently, this gives the number of times the path winds around the singularity, also corresponding to the winding number.

3.4.2 Chern number

The Chern number is a type of topological invariant that describes the geometric properties of "bundles". Similar to the winding number, the Chern number also belongs to $\mathbb{Z}$ topological invariants, which can only take integer values. Physically, the Chern number is typically used to describe the topological properties of even-dimensional systems. For topological systems of different dimensions, the first and second Chern numbers correspond to phenomena such as two-dimensional systems and four-dimensional quantum Hall effect, respectively. In this section, we

briefly introduce the first Chern number.

We consider a two-dimensional system with N energy bands, whose Berry curvature is $\Omega_{ij}(\boldsymbol{k})$. The Chern number of the system is defined as the integral of the Berry curvature over the Brillouin zone:

$$C = \frac{1}{2\pi} \int_{\mathrm{BZ}} d^2\boldsymbol{k} \ \mathrm{Tr}\ \Omega_{ij}(\boldsymbol{k}), \tag{3.31}$$

where

$$\mathrm{Tr}\ \Omega_{ij}(\boldsymbol{k}) = \sum_{\alpha=1}^{N} (\mathrm{Tr}\ \Omega_{\alpha\alpha}(\boldsymbol{k}))_{ij}. \tag{3.32}$$

One important application of the Chern number is in explaining the integer quantum Hall effect (IQHE). The IQHE refers to the phenomenon where, under strong magnetic fields and extremely low temperatures, the Hall conductivity of a two-dimensional electron gas exhibits perfect quantization. Under certain conditions, the Hall conductivity σ_{xy} no longer changes continuously but instead shows a step-like, discrete, and integer-quantized behavior. In this effect, when electrons in a two-dimensional electron gas are subjected to a strong magnetic field, the Hall conductivity can be expressed as:

$$\sigma_{xy} = C\frac{e^2}{h}, \tag{3.33}$$

where e is the electron charge, h is the Planck constant, and C is Chern number. This relationship indicates that the Hall conductivity is quantized, with the Chern number determining the level of quantization.

3.4.3 $\mathbb{Z}_2$ invariant

As mentioned above, the integer quantum Hall insulator can generally be classified using the first Chern number. However, for two-dimensional topological insulators with time-reversal symmetry, the first Chern number is always zero, regardless of whether the system has other topological properties. Therefore, it cannot be used to classify systems with time-reversal symmetry. In 2005, Kane and Mele introduced the $\mathbb{Z}_2$ topological invariant, to characterize the topological properties of systems with time-reversal symmetry [8]. In this section, we introduce the Pfaffian

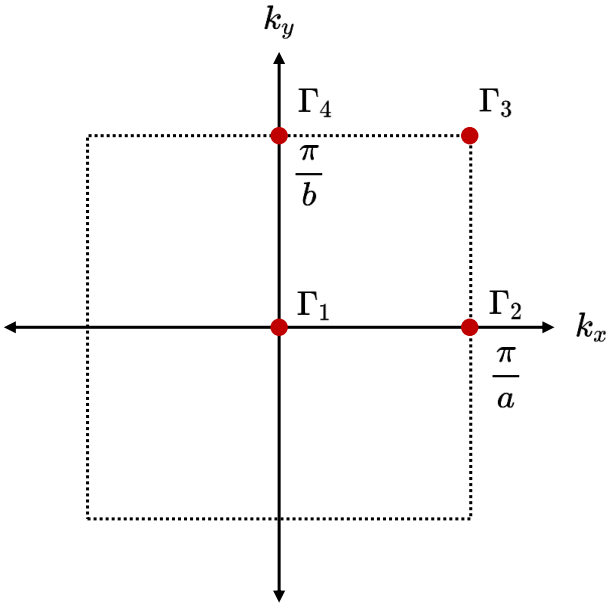

Figure 3.3: Two-dimensional Brillouin zone with four red points representing the time-reversal invariant momenta (TRIM).

method for calculating $\mathbb{Z}_2$ topological invariant.

For a system with time-reversal symmetry, Kramers degeneracy occurs, meaning the number of energy bands must be even. We consider a system with $2N$ occupied energy bands and define the following unitary matrix

$$\omega_{mn}(\boldsymbol{k}) = \langle u_{m,-\boldsymbol{k}} | \mathcal{T} | u_{n,\boldsymbol{k}} \rangle, \tag{3.34}$$

where $m, n = 1, 2, ..., 2N$ denote the indices of the energy bands, $\mathcal{T}$ represents the time-reversal operator, and $|u_{n,\boldsymbol{k}}\rangle$ is the periodic part of the Bloch function. Here, the matrix ω has an important property:

$$\omega_{mn}(-\boldsymbol{k}) = -\omega_{nm}(-\boldsymbol{k}). \tag{3.35}$$

For a two-dimensional topological insulator, the system has four time-reversal invariant momenta (TRIM), which are positioned at specific points in the Brillouin zone as shown in Fig. 3.3. These TRIM points, listed counterclockwise, are:

$$\Gamma_1 = (0,0), \quad \Gamma_2 = \left(\frac{\pi}{a}, 0\right), \quad \Gamma_3 = \left(\frac{\pi}{a}, \frac{\pi}{b}\right), \quad \Gamma_4 = \left(0, \frac{\pi}{b}\right), \tag{3.36}$$

where a and b are the lattice constants in the two spatial directions. At these TRIM points, the matrix ω is anti-symmetric, satisfying $\omega^T(\Gamma_i) = -\omega(\Gamma_i)$. Mathematically, for an even-dimensional anti-symmetric matrix A, its Pfaffian can be defined as:

$$\mathrm{Pf}(A) = \frac{1}{2^N N!} \sum_P \mathrm{sgn}(P) A_{P(1)P(2)} A_{P(3)P(4)} \dots A_{P(2N-1)P(2N)}. \tag{3.37}$$

Here, P represents the permutation group elements of $(1, 2, ..., 2N-1, 2N)$. The sign $\mathrm{sgn}(P) = -1$ for an odd number of permutations and $\mathrm{sgn}(P) = 1$ for an even number of permutations. Mathematically, it can also be shown that the determinant of an anti-symmetric matrix equals the square of its Pfaffian, expressed as $\det(A) = [\mathrm{Pf(A)}]^2$. Based on this property, a $\mathbb{Z}_2$ topological invariant can be defined by

$$(-1)^\nu = \prod_{i=1}^{4} \delta_i, \tag{3.38}$$

where

$$\delta_i = \frac{\mathrm{Pf}\left[\omega\left(\Gamma_i\right)\right]}{\sqrt{\det\left[\omega\left(\Gamma_i\right)\right]}} = \pm 1, \tag{3.39}$$

and ν refers to the $\mathbb{Z}_2$ invariant.

From the above definition, we note that the topological invariant $\nu \in \{0, 1\}$, belonging to a $\mathbb{Z}_2$ group. Therefore, two-dimensional topological insulators with time-reversal symmetry can be classified into two types: $\nu = 0$ corresponds to a normal insulator, while $\nu = 1$ corresponds to a topological insulator.

This concept can also be extended to three-dimensional systems with time-reversal symmetry, where four $\mathbb{Z}_2$ topological invariants (one strong topological invariant and three weak topological invariants) are used to describe the system's topological properties. According to this classification, three-dimensional time-reversal invariant insulator systems can be divided into three types: trivial normal insulators, weak topological insulators, and strong topological insulators. Determining whether a time-reversal symmetric system has nontrivial topological properties can be done by calculating its $\mathbb{Z}_2$ topological invariants.

3.5 Bulk-boundary correspondence

In conventional insulators, the bulk and boundary states of the material are independent of each other. However, in topological insulators, the situation is entirely different. Although the bulk states of these materials behave as insulators, their boundaries exhibit conductivity. This conductivity is not only directly related to the topological properties of the material but also remains robust against slight disorder or defects. This characteristic arises from the bulk-boundary correspondence (BBC) in topological systems [122, 139].

The BBC is a core concept in topological physics that describes the close relationship between the topological properties of bulk states and the conductive states at the boundaries. This principle states that when the bulk of a material exhibits nontrivial topological properties, topologically protected conductive edge states will emerge at its boundaries, and the number of these boundary states is directly related to the value of the topological invariant. This phenomenon is observed in systems such as the Su-Schrieffer-Heeger (SSH) model [140–143], IQHI, QSHI, and even three-dimensional topological insulators, playing a crucial role in understanding and designing novel quantum materials.

According to the BBC, for a one-dimensional system described by a winding number, if the winding number w of the bulk Hamiltonian (which can be thought of as the Hamiltonian under periodic boundary conditions) is non-zero, there will be edge states at the boundaries of the system. This principle can be extended to junction systems: if a system consists of two homogeneous subsystems with different parameters, and these two subsystems have different winding numbers w_1 and w_2, there must be topologically protected zero-energy states at the junction interface, and the number of these states is given by $|w_1 - w_2|$. This result can also be generalized to other $\mathbb{Z}$ topological invariants, such as the Chern number in two-dimensional systems, where the difference in Chern numbers between regions leads to the presence of chiral edge states.

The BBC for systems described by $\mathbb{Z}_2$ invariants is a bit different. The $\mathbb{Z}_2$ invariant ν can only take the values 0 or 1. When the $\mathbb{Z}_2$ invariant ν of the bulk Hamiltonian equals 1, this indicates a topologically nontrivial phase, and an odd number of Kramers pairs will emerge at the boundaries as a helical edge state which is robust against symmetry-preserving perturbations. Conversely, when $\nu = 0$, the system is in a topologically trivial phase, and an even number (including zero) of Kramers pairs will appear at the boundaries. However, these states are unstable against per-

turbations and can be absorbed into the bulk bands. This distinction is crucial for understanding systems with time-reversal symmetry, such as quantum spin Hall insulators, where the presence of an odd number of Kramers pairs is a hallmark of nontrivial $\mathbb{Z}_2$ topology.

3.6 Symmetry and AZ classification

In physics, the symmetry of a system plays a crucial role. System symmetry refers to a property that remains unchanged when the system undergoes certain transformations. If a system possesses a particular continuous symmetry, there is necessarily a corresponding conservation law [144, 145]. For example, if a system has time translation symmetry, it conserves energy; if it has spatial translation symmetry, it conserves momentum; and if it has $U(1)$ global symmetry, it corresponds to the conservation of charge. Symmetry also plays a vital role in topological physics. In Hermitian systems, the classification of topological systems is associated with three types of symmetries: time-reversal symmetry (TRS), particle-hole symmetry (PHS), and chiral symmetry (CS) [146, 147]. These symmetries are defined as follows:

$$\mathcal{T}H^*\mathcal{T}^{-1} = H \qquad \text{(TRS)}, \tag{3.40a}$$

$$\Xi H^*\Xi^{-1} = -H \qquad \text{(PHS)}, \tag{3.40b}$$

$$\Gamma H\Gamma^{-1} = -H \qquad \text{(CS)}, \tag{3.40c}$$

where $\mathcal{T}$, Ξ and Γ are TRS operator, PHS operator and CS operator, respectively. These are unitary operators that satisfy $\mathcal{T}\mathcal{T}^* = \pm 1$, and $\Xi\Xi^* = \pm 1$. In Hermitian systems, where $H^\dagger = H$, chiral symmetry (CS) is also referred to as sublattice symmetry (SLS).

By applying a Fourier transformation $|x\rangle = \frac{1}{\sqrt{N}}\sum_k e^{-ikx}|k\rangle$, a one-dimensional real-space Hamiltonian $H(x)$ can be diagonalized in momentum space as $H(x) = \sum_k |k\rangle\langle k| \otimes H(k)$. The symmetries in momentum space can then be expressed as:

$$\mathcal{T}H^*(k)\mathcal{T}^{-1} = H(-k) \qquad \text{(TRS)}, \tag{3.41a}$$

$$\Xi H^*(k)\Xi^{-1} = -H(-k) \qquad \text{(PHS)}, \tag{3.41b}$$

$$\Gamma H(k)\Gamma^{-1} = -H(k) \qquad \text{(CS)}. \tag{3.41c}$$

Note that the CS operator can be obtained by combining the THS operator and PHS operator,

Table 3.1: The table of the 10-fold AZ classification [146, 147]. The first column shows the names of the symmetry classes. For TRS and PHS, ±1 indicate the value of $\mathcal{T}\mathcal{T}^*$ or $\Xi\Xi^*$, while 0 represents the absence of the symmetry. For CS, 1 and 0 denote whether the system has CS or not. The right part shows the type of topology of a d-dimensional system, where $\mathbb{Z}$, $\mathbb{Z}_2$ and 0 indicate that the system exhibits $\mathbb{Z}$ topology, $\mathbb{Z}_2$ topology, or is topologically trivial. Specifically, $2\mathbb{Z}$ indicates that the system possesses an even $\mathbb{Z}$ topological invariant.

Class	TRS	PHS	CS	$d=0$	$d=1$	$d=2$	$d=3$	$d=4$	$d=5$	$d=6$	$d=7$
A	0	0	0	$\mathbb{Z}$	0	$\mathbb{Z}$	0	$\mathbb{Z}$	0	$\mathbb{Z}$	0
AIII	0	0	1	0	$\mathbb{Z}$	0	$\mathbb{Z}$	0	$\mathbb{Z}$	0	$\mathbb{Z}$
AI	+1	0	0	$\mathbb{Z}$	0	0	0	$2\mathbb{Z}$	0	$\mathbb{Z}_2$	$\mathbb{Z}_2$
BDI	+1	+1	1	$\mathbb{Z}_2$	$\mathbb{Z}$	0	0	0	$2\mathbb{Z}$	0	$\mathbb{Z}_2$
D	0	+1	0	$\mathbb{Z}_2$	$\mathbb{Z}_2$	$\mathbb{Z}$	0	0	0	$2\mathbb{Z}$	0
DIII	-1	+1	1	0	$\mathbb{Z}_2$	$\mathbb{Z}_2$	$\mathbb{Z}$	0	0	0	$2\mathbb{Z}$
AII	-1	0	0	$2\mathbb{Z}$	0	$\mathbb{Z}_2$	$\mathbb{Z}_2$	$\mathbb{Z}$	0	0	0
CII	-1	-1	1	0	$2\mathbb{Z}$	0	$\mathbb{Z}_2$	$\mathbb{Z}_2$	$\mathbb{Z}$	0	0
C	0	-1	0	0	0	$2\mathbb{Z}$	0	$\mathbb{Z}_2$	$\mathbb{Z}_2$	$\mathbb{Z}$	0
CI	+1	-1	1	0	0	0	$2\mathbb{Z}$	0	$\mathbb{Z}_2$	$\mathbb{Z}_2$	$\mathbb{Z}$

as $\Gamma = \Xi\mathcal{T}$. For a system that possesses both TRS and PHS, we have:

$$\Gamma H \Gamma^{-1} = \Xi\mathcal{T} H \mathcal{T}^{-1}\Xi^{-1} = \Xi H^* \Xi^{-1} = -H, \tag{3.42}$$

which indicates that the system must also possess CS, with $\Gamma = \Xi\mathcal{T}$. This relationship shows that the presence of both TRS and PHS ensures the existence of CS, linking these symmetries together in topological classification.

In 1997, Alexander Altland and Martin R. Zirnbauer proposed a classification of disordered systems based on symmetry [146]. For TRS, a system can have three possibilities: $\mathcal{T}\mathcal{T}^* = \pm 1$ or no TRS. Similarly, for PHS, there are also three possibilities: $\Xi\Xi^* = \pm 1$ or no PHS. By combining these options, we obtain nine possible combinations of symmetry properties for system Hamiltonians.

Since CS can be defined as a combination of TRS and PHS, it does not need to be considered separately when both are present. However, when the system lacks both THS and PHS, CS must still be considered in two cases: either satisfying CS or not satisfying CS. Therefore, the combination of these three symmetries results in $9 - 1 + 2 = 10$ types, known as 10-fold Altland-Zirnbauer (AZ) classification [146, 147].

Table 3.1 lists the 10-fold classifications, each corresponding to a different combination of

symmetries and the associated symmetries of the Hamiltonian. Different spatial dimensions correspond to different systems, and the topological properties of these systems can be characterized by $\mathbb{Z}$ or $\mathbb{Z}_2$ topological invariants. Among them, classes A and AIII are relatively special because they are only related to CS and are referred to as complex symmetry classes. The remaining 8 classes are known as real symmetry classes.

These 10 symmetry classes correspond to a variety of models. For example, the well-known one-dimensional SSH model belongs to the BDI class and is described by the winding number ($\mathbb{Z}$ topological invariant). The IQH insulator and QSH insulator correspond to the two-dimensional A and AII classes, characterized by $\mathbb{Z}$ and $\mathbb{Z}_2$ topological phases, respectively. In Chapter 4, we will study the $\mathbb{Z}_2$ topological phase of a one-dimensional DIII class system in detail, focusing on its robustness in stacked systems.

Chapter 4

Topological Phases in Non-Hermitian Systems

4.1 Introduction

The study of non-Hermitian systems has gained significant attention in recent years due to its potential for novel physical phenomena, especially relating to topological phases, and practical applications. In this chapter, we extend the discussion of topological phases to non-Hermitian systems. The presence of complex eigenenergies positions the energy spectrum on the complex plane, allowing the energy gap to be classified into two types: line gaps and point gaps. In Sec. 4.2, we introduce these two types of energy gaps and their unique topological properties. This thesis focuses on the point-gap topology, which gives rise to the non-Hermitian skin effect — a phenomenon in which all eigenstates become localized at the system boundaries, as discussed in Sec. 4.4. This effect is naturally explained within the framework of non-Bloch band theory, an extension of Bloch band theory tailored for non-Hermitian systems, covered in Sec. 4.3. Finally, we examine the symmetries and the 38-fold classification of non-Hermitian Hamiltonians.

4.2 Line gap and point gap

The concept of an energy gap in non-Hermitian systems significantly differs from its counterpart in Hermitian systems. In Hermitian systems, the energy gap refers to regions in the energy spectrum where no states are present, as illustrated in Fig. 4.1(a). Because the energy spectrum in Hermitian systems lies on the real axis, the gap region can reduce to a single zero-dimensional

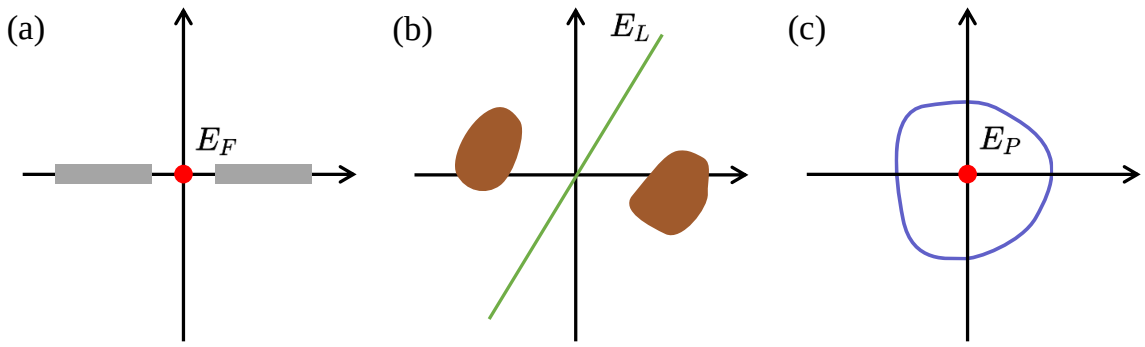

Figure 4.1: Schematic diagram of energy gaps in Hermitian and non-Hermitian systems. (a) Real energy gap for a Hermitian Hamiltonian. The energy gap opens if and only if the energy bands do not cross the Fermi energy E_F. (b) Line gap for a non-Hermitian Hamiltonian. A line gap exists if and only if the complex energy spectrum does not cross a reference line E_L. (c) Point gap for a non-Hermitian Hamiltonian. A point gap exists if and only if the complex energy spectrum does not cross a reference point E_P.

point, $E = E_F$, known as the Fermi energy. An open energy gap occurs when no energy bands cross the Fermi energy, and a topological phase transition takes place if and only if the energy gap closes or reopens.

In non-Hermitian systems, however, the energy spectrum extends to two dimensions in the complex plane, allowing energy gaps to be defined in terms of either a zero-dimensional point or a one-dimensional line, corresponding to point gaps and line gaps, respectively [43, 44]. The concepts of point gaps and line gaps are essential for understanding the various types of topological phases that emerge due to the complex nature of these spectra.

A non-Hermitian Hamiltonian is defined to have a line gap if and only if its complex-energy bands do not cross a reference line E_L in the complex plane, as shown in Fig. 4.1(b). For a spectrum with an open line gap at E_L, it can be continuously deformed into a similar spectrum of a Hermitian Hamiltonian without closing the line gap. This property suggests that the line gap can be viewed as an extension of the Hermitian energy gap, describing the persistence of conventional topological phases under non-Hermitian perturbations, a property that is particularly relevant to the design of topological lasers.

In contrast, a point gap is defined as a condition where the complex energy spectrum of a Hamiltonian does not cross a reference point $E = E_P$, as shown in Fig. 4.1(c). Different from a line gap, the spectrum of a Hamiltonian with an open point gap cannot be continuously deformed

into the spectrum of a Hermitian Hamiltonian without closing the point gap. This suggests that point-gap topology is an intrinsic feature of non-Hermitian systems, giving rise to unique physical phenomena. For example, in a one-dimensional system with a point gap, we can define a winding number for the point-gap topology, which describes how the energy spectrum encircles the reference point E_P. This winding number directly affects the distribution of eigenstates, often resulting in phenomena like the non-Hermitian skin effect, where all eigenstates become localized near the system boundaries. We will discuss this phenomenon in detail in the next section.

4.3 Non-Bloch band theory

In Hermitian systems, the bulk-boundary correspondence accurately predicts the boundary states of a system based on the topology of the bulk Hamiltonian. However, in non-Hermitian systems, the traditional bulk-boundary correspondence has been shown to break down in several studies [148]. In this section, we examine the reasons behind this failure: the Bloch band theory, effective in Hermitian systems, no longer applies in non-Hermitian contexts. By rigorously analyzing the Hatano-Nelson model, we extend Bloch band theory to non-Hermitian systems, known as non-Bloch band theory. This extension leads to the concept of the generalized Brillouin zone, which replaces the conventional Brillouin zone in non-Hermitian systems.

The Hatano-Nelson (HN) model serves as a prototypical example of a one-dimensional non-Hermitian system [64–66]. It introduces asymmetric hopping, resulting in a non-Hermitian Hamiltonian. Here, we consider a HN model without on-site potentials. The Hamiltonian under arbitrary boundary conditions is given by

$$H = \sum_{i=1}^{N-1} \left[(t+g) a_i^\dagger a_{i+1} + (t-g) a_{i+1}^\dagger a_i \right] + \lambda \left[(t+g) a_N^\dagger a_1 + (t-g) a_1^\dagger a_N \right], \tag{4.1}$$

where $t, g \in \mathbb{R}$ represent the asymmetric hopping strengths, and N is the length of the chain. The parameter $\lambda = 1$ indicates periodic boundary conditions, while $\lambda = 0$ indicates open boundary

conditions. The eigenvalue equation of H can be written as

$$\begin{pmatrix} 0 & t+g & 0 & \dots & 0 & \lambda(t-g) \\ t-g & 0 & t+g & \dots & 0 & 0 \\ 0 & t-g & 0 & \dots & 0 & 0 \\ \vdots & \vdots & \vdots & \ddots & \vdots & \vdots \\ 0 & 0 & 0 & \dots & 0 & t+g \\ \lambda(t+g) & 0 & 0 & \dots & t-g & 0 \end{pmatrix} \begin{pmatrix} \phi_1 \\ \phi_2 \\ \phi_3 \\ \vdots \\ \phi_{N-1} \\ \phi_N \end{pmatrix} = E \begin{pmatrix} \phi_1 \\ \phi_2 \\ \phi_3 \\ \vdots \\ \phi_{N-1} \\ \phi_N \end{pmatrix}, \tag{4.2}$$

where $\Phi = (\phi_1, \phi_2, \dots, \phi_N)^T$ is the eigenstate vector. This equation leads to the bulk equation

$$(t+g)\phi_{i+1} + (t-g)\phi_{i-1} = E\phi_i \tag{4.3}$$

for the interior sites of the chain. From the theory of linear difference equations, the solution of Eq. (4.3) can be written in the form

$$\Phi(\beta) = \left(\beta, \beta^2, \dots, \beta^N\right)^T. \tag{4.4}$$

Substituting Eq. (4.4) into bulk equation Eq. (4.3) yields

$$(t+g)\beta^2 - E\beta + t - g = 0. \tag{4.5}$$

Thus, for any energy E, there are two solutions, $\Phi(\beta_1)$ and $\Phi(\beta_2)$, for the bulk equation, given by

$$\beta_{1/2} = \frac{E \pm \sqrt{E^2 - 4(t^2 - g^2)}}{2(t+g)}. \tag{4.6}$$

The wave function can then be expressed as a superposition of $\Phi(\beta_1)$ and $\Phi(\beta_2)$

$$\Phi = c_1\Phi(\beta_1) + c_2\Phi(\beta_2). \tag{4.7}$$

In the case of open boundary conditions, substituting this solution into Eq. (4.2) yields the boundary conditions at the edges:

$$(t+g)(c_1\beta_1^2 + c_2\beta_2^2) = E(c_1\beta_1 + c_2\beta_2), \tag{4.8}$$

$$(t-g)(c_1\beta_1^{N-1} + c_2\beta_2^{N-1}) = E(c_1\beta_1^N + c_2\beta_2^N). \tag{4.9}$$

Combining with Eq. (4.5), we get

$$-(t-g)c_1-(t-g)c_2=0, \tag{4.10}$$

$$-(t+g)\beta_1^{N+1}c_1-(t+g)\beta_2^{N+1}c_2=0. \tag{4.11}$$

By multiplying the left and right sides of Eq. (4.10) and Eq. (4.11) separately, we obtain

$$\beta_1^{N+1}=\beta_2^{N+1}. \tag{4.12}$$

Here, we consider a very long chain. To ensure that this relation holds in the limit as $N\to\infty$, we require that

$$|\beta_1|=|\beta_2|. \tag{4.13}$$

Using Eq. (4.5), which gives $\beta_1\beta_2=(t-g)/(t+g)$, we can solve for β_1 and β_2:

$$\beta_{1/2}=\sqrt{\left|\frac{t-g}{t+g}\right|}e^{\pm ik},\quad k=\frac{n\pi}{N+1},\quad n=1,2,\cdots,N. \tag{4.14}$$

As $N\to\infty$, the solutions for β_1 and β_2 in the complex plane form a closed curve:

$$\beta_=\sqrt{\left|\frac{t-g}{t+g}\right|}e^{ik},\quad k\in(0,\ 2\pi), \tag{4.15}$$

which is known as the generalized Brillouin zone (GBZ) [52, 148–150].

In this model, the GBZ forms a circle that lies either inside or outside the standard Brillouin zone, with a radius given by $r=|\beta|$. The energy spectrum under OBC, denoted σ_{OBC}, can be determined from Eq. (4.5) as

$$E_{\mathrm{OBC}}=2\sqrt{t^2-g^2}\cos k, \tag{4.16}$$

which forms an arc on the real axis. In contrast, the energy spectrum under PBC, σ_{PBC}, is given by

$$E_{\mathrm{PBC}}=2t\cos k+2gi\sin k, \tag{4.17}$$

which traces out an ellipse that encloses σ_{OBC}. Here, the boundary conditions cannot be treated as a mere perturbation, as the energy spectrum is highly sensitive to them. As for the wavefunc-

tions, when $g > 0$ ($g < 0$), the eigenstates take the form $\phi_E \propto \left(\sqrt{\left|\frac{t-g}{t+g}\right|}e^{ik}, \left(\sqrt{\left|\frac{t-g}{t+g}\right|}e^{ik}\right)^2, ..., \left(\sqrt{\left|\frac{t-g}{t+g}\right|}e^{ik}\right)^N\right)^T$, with all eigenstates localized at the left (right) boundary. These states, known as non-Hermitian skin modes, exhibit exponential localization at the system boundaries. This phenomenon is called the non-Hermitian skin effect, which we will discuss in detail in the next section.

Notably, in the Hermitian limit where $g = 0$, the GBZ coincides with the standard Brillouin zone, suggesting that the GBZ serves as a natural extension of the Brillouin zone. By replacing all points on the Brillouin zone with those on the GBZ, via the transformation $e^{ik} \to \beta$, we can obtain the non-Bloch Hamiltonian $H(\beta)$ and the corresponding non-Bloch wavefunctions $|\psi(\beta)\rangle$. The non-Bloch Hamiltonian accurately describes the energy spectrum properties of non-Hermitian systems with open boundary conditions in the thermodynamic limit. The energy spectrum is then obtained by diagonalizing the non-Bloch Hamiltonian, and the winding number is defined through an integral along the GBZ.

For the HN model, the characteristic equation Eq. (4.5) has only two roots, and the GBZ is given by Eq. (4.13). In Ref. [149], this result has been extended to multi-band systems. For a one-dimensional tight-binding model with l bands, where each lattice site has m internal degrees of freedom, the characteristic equation

$$\det(H(\beta) - E) = 0 \tag{4.18}$$

has $2ml$ roots. Arranging all roots in order of increasing modulus, we have

$$|\beta_1| \leqslant \cdots \leqslant |\beta_{ml}| \leqslant |\beta_{ml+1}| \leqslant \cdots \leqslant |\beta_{2ml}|\,, \tag{4.19}$$

and the GBZ is given by

$$|\beta_{ml}| = |\beta_{ml+1}|\,, \tag{4.20}$$

which is known as the non-Bloch band theory.

Unlike the simple HN model, the GBZ in general forms irregular closed curves on the complex plane that encircles the origin and may even intersect with the Brillouin zone (the unit circle). The shape of the GBZ provides insight into the distribution of the system's eigenstates. According to the translational symmetry in non-Bloch band theory, if a point on the GBZ lies inside the

Brillouin zone, the corresponding wave function is a left-skin mode, while a point on the GBZ located outside the Brillouin zone corresponds to a right-skin mode. Specifically, points where the GBZ intersects the Brillouin zone correspond to non-skin modes.

However, as pointed out in Ref. [150], the standard non-Bloch band theory requires modifications for symplectic class systems (class AII†). Such a system exhibits spinful TRS† ($\mathcal{T}H^T(\beta)\mathcal{T}^{-1} = H(\beta^{-1})$, where $\mathcal{T}\mathcal{T}^* = -1$, see Sec. 4.5 for details). If β is one of the roots of Eq. (4.18), we have

$$\det(H(\beta^{-1}) - E) = \det(\mathcal{T}H^T(\beta)\mathcal{T}^{-1} - E) = \det(H(\beta) - E) = 0, \tag{4.21}$$

indicating that β^{-1} is another root of Eq. (4.18). Thus, the characteristic equation has $4ml$ roots, which can be ordered by modulus as follows:

$$|\beta_1| \leqslant \cdots \leqslant |\beta_{2ml}| \leqslant 1 \leqslant \left|\beta_{2ml}^{-1}\right| \leqslant \cdots \leqslant \left|\beta_1^{-1}\right|. \tag{4.22}$$

According to the standard non-Bloch band theory, the GBZ is given by $|\beta_{2ml}| = \left|\beta_{2ml}^{-1}\right| = 1$, indicating the GBZ collapses onto the Brillouin zone, what means that there is no skin modes. However, this is impossible for the following reason: $\mathcal{T}H^T(\beta)\mathcal{T}^{-1} = H(\beta^{-1})$ implies that the system has at least a two-fold degeneracy, corresponding to eigenstates $|\psi\rangle$ and $\mathcal{T}|\psi\rangle\rangle^*$, where $|\psi\rangle$ and $\langle\langle\psi|$ are the right and left eigenstate, respectively. These eigenstates correspond to β and β^{-1} on the GBZ, meaning they localize at different edges of the system. In general, the system's energy spectrum is non-degenerate, implying that these two eigenstates are equivalent. However, the condition $\mathcal{T}\mathcal{T}^* = -1$ requires that

$$\langle\langle\psi|\mathcal{T}|\psi\rangle\rangle^* = \langle\langle\psi|\mathcal{T}^T|\psi\rangle\rangle^* = -\langle\langle\psi|\mathcal{T}|\psi\rangle\rangle^* = 0, \tag{4.23}$$

which indicates that $|\psi\rangle$ and $\mathcal{T}|\psi\rangle\rangle^*$, associated with the same eigenenergy, are bi-orthogonal and linearly independent. These states form skin modes that are localized at opposite boundaries of the system. Such pairs of eigenstates are referred to as Kramers pairs. The modified non-Bloch band theory provides the GBZ applicable to symplectic systems, given by:

$$|\beta_{2ml-1}| = |\beta_{2ml}|. \tag{4.24}$$

In symplectic systems with Kramers pairs, the GBZ consists of pairs of points located inside and outside the Brillouin zone, ensuring that the numbers of left- and right-skin modes are equal. This phenomenon, known as the $\mathbb{Z}_2$ non-Hermitian skin effect, arises from a nontrivial $\mathbb{Z}_2$ point-gap topology. In the next section, we use the HN model and the symplectic HN model as examples to explore the relationship between point-gap topology and the non-Hermitian skin effect.

4.4 Non-Hermitian skin effect

In Sec. 4.3, we introduced non-Bloch band theory and the GBZ to explain the unique localization of eigenstates in non-Hermitian systems under OBC, known as the non-Hermitian skin effect (NHSE) [40, 45–63]. However, Ref. [54] provides a topological perspective, suggesting that the origin of the NHSE lies in the presence of a nontrivial point-gap topology in the bulk Hamiltonian. They demonstrated that the OBC spectrum of a non-Hermitian system σ_{OBC} forms an arc without enclosed area, indicating that the Hamiltonian under OBC is always topologically trivial. Consequently, the non-Hermitian skin effect inevitably accompanies a topological phase transition whenever the Hamiltonian under PBC exhibits a nontrivial point-gap topology. In this case, the PBC spectrum σ_{PBC} forms a closed curve with a finite enclosed area, and a complex energy point E within this area can be assigned a non-zero winding number, defined as

$$W(E) = \int_0^{2\pi} \frac{dk}{2\pi \mathrm{i}} \frac{d}{dk} \log \det[H(k) - E], \tag{4.25}$$

where $W(E) \in \mathbb{Z}$ represents the number of times σ_{PBC} winds around the point E.

To demonstrate this theory, we once again consider the HN model without on-site potential, whose momentum Hamiltonian is given by

$$H(k) = (t + g)e^{ik} + (t - g)e^{-ik}. \tag{4.26}$$

In the case $g > 0$, the winding number calculated by Eq. (4.25) is equal to +1, indicating that the PBC spectrum, which forms an ellipse in the complex plane, encloses a finite area in an anticlockwise direction. Under OBC, the spectrum appears as a line on the real axis, lying within the topologically nontrivial region defined by the PBC spectrum, as shown in Fig. 4.2(a). According

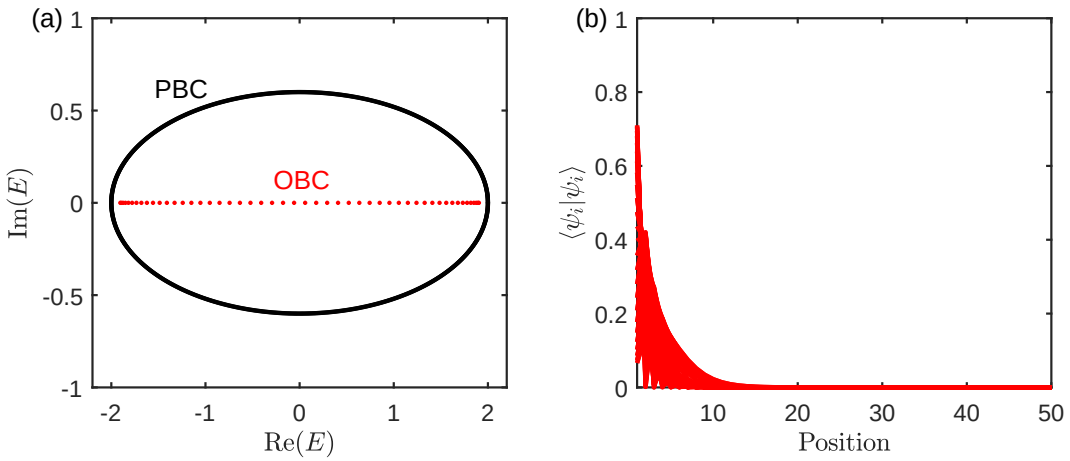

Figure 4.2: Non-Hermitian skin effect in a HN model with size $L = 50$, $t = 1$ and $g = 0.3$. (a) Eigenenergy spectrum under PBC (black curve) and OBC (red dots) (b) Spatial distribution of eigenstates, showing all eigenstates localized at the left boundary.

to the theory, the emergence of a nontrivial point-gap topology in the PBC Hamiltonian signals the presence of the NHSE, where all eigenstates are localized at the left boundary of the system, as illustrated in Fig. 4.2(b).

Next, we consider a time-reversal symmetric system H_c, formed by coupling the HN chain $H(k)$ with its time-reversal symmetric partner $H^T(-k)$. Analogous to the QSHI, we introduce a spin-orbit coupling between $H(k)$ and $H^T(-k)$, and the momentum-space Hamiltonian of the coupled HN model is defined as:

$$H_c(k) = \begin{pmatrix} H(k) & 2\Delta \sin k \\ 2\Delta \sin k & H^T(-k) \end{pmatrix}, \tag{4.27}$$

with $\Delta \in \mathbb{R}$ represents the coupling strength. We note that $H_c(k)$ belongs to the AII† symmetry class, which possesses spinful TRS†. According to Eq. (4.23), in an AII† system, any eigenenergy E has two associated eigenstates $|\psi\rangle$ and $\mathcal{T}|\psi\rangle\rangle^*$, which form a Kramers pair. This results in a double-degenerate spectrum.

When calculating the winding number $W(E)$ for this system, we find that $W(E) \equiv 0$ even if E is enclosed by the PBC spectrum of $H_c(k)$. This occurs because each Kramers pair contributes an opposite winding number, meaning that the degenerate energy spectrum consists of two identical closed curves winding in opposite directions, effectively canceling each other's contribution to the total winding number.

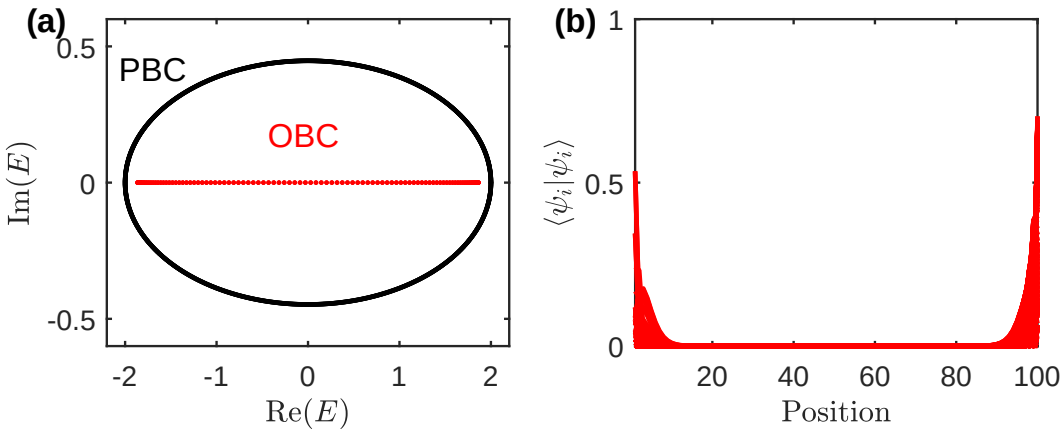

Figure 4.3: Non-Hermitian skin effect in a coupled HN model with size $L = 100$, $t = 1$, $g = 0.3$ and $\Delta = 0.2$. (a) Eigenenergy spectrum under PBC (black curve) and OBC (red dots) (b) Spatial distribution of eigenstates, showing all eigenstates localized at the both boundaries.

Although the winding number is zero, the energy spectrum of this coupled system still encloses a finite area, indicating that point-gap topology can be defined. The topological number is characterized by the $\mathbb{Z}_2$ invariant, which is defined as

$$(-1)^{\nu(E)} = \mathrm{sgn}\left\{\frac{\mathrm{Pf}[(H(\pi)-E)T]}{\mathrm{Pf}[(H(0)-E)T]} \times \exp\left[-\frac{1}{2}\int_{k=0}^{k=\pi} dk\, \partial_k \log\det[(H(k)-E)T]\right]\right\}. \tag{4.28}$$

Here, Pf denotes the Pfaffian, and $\nu(E) \in \{0, 1\}$ represents the $\mathbb{Z}_2$ invariant.

The energy spectrum of H_c is depicted in Fig. 4.3(a). Under PBC, the spectrum forms an elliptical contour, and for energy points enclosed by this ellipse, $\nu = 1$. Under OBC, the spectrum forms an arc lying within the topologically nontrivial region of the PBC spectrum. All eigenstates form Kramers pairs and exhibit boundary localization at both ends of the system, as shown in Fig. 4.3(b). This phenomenon is referred to as the $\mathbb{Z}_2$ non-Hermitian skin effect.

4.5 Symmetry and classification for non-Hermitian systems

In Hermitian systems, a system is classified into the 10-fold AZ symmetry class by considering the presence or absence of three symmetries; time-reversal symmetry (TRS), partical-hole symmetry (PHS) and chiral symmetry (CS) or sublattice symmetry (SLS). In Ref.[43], because of the absence of Hermiticity ($H^* \neq H^T$), it is shown that the non-Hermitian systems possess the additional symmetry class called AZ† symmetry class where TRS and PHS are ramified as TRS†

and PHS†, respectively. These symmetry relations are summarized as

$$\mathcal{T}_+ H^* \mathcal{T}_+^{-1} = +H \qquad \text{(TRS)}, \tag{4.29a}$$

$$\mathcal{T}_- H^T \mathcal{T}_-^{-1} = +H \qquad \text{(TRS}^\dagger\text{)}, \tag{4.29b}$$

$$\Xi_+ H^T \Xi_+^{-1} = -H \qquad \text{(PHS)}, \tag{4.29c}$$

$$\Xi_- H^* \Xi_-^{-1} = -H \qquad \text{(PHS}^\dagger\text{)}, \tag{4.29d}$$

$$\Gamma H^\dagger \Gamma^{-1} = -H \qquad \text{(CS)}, \tag{4.29e}$$

$$S H S^{-1} = -H \qquad \text{(SLS)}, \tag{4.29f}$$

where H stands a non-Hermitian Hamiltonian in the real space and $\mathcal{T}_\pm, \Xi_\pm, \Gamma$, and S are unitary operators. Then the symmetries in momentum space can then be expressed as:

$$\mathcal{T}_+ H^*(k) \mathcal{T}_+^{-1} = +H(-k) \qquad \text{(TRS)}, \tag{4.30a}$$

$$\mathcal{T}_- H^T(k) \mathcal{T}_-^{-1} = +H(-k) \qquad \text{(TRS}^\dagger\text{)}, \tag{4.30b}$$

$$\Xi_+ H^T(k) \Xi_+^{-1} = -H(-k) \qquad \text{(PHS)}, \tag{4.30c}$$

$$\Xi_- H^*(k) \Xi_-^{-1} = -H(-k) \qquad \text{(PHS}^\dagger\text{)}, \tag{4.30d}$$

$$\Gamma H^\dagger(k) \Gamma^{-1} = -H(+k) \qquad \text{(CS)}, \tag{4.30e}$$

$$S H(k) S^{-1} = -H(+k) \qquad \text{(SLS)}. \tag{4.30f}$$

Similar to Hermitian systems, non-Hermitian systems can also be classified based on TRS (TRS†), PHS (PHS†) and CS. Due to the additional symmetries involved in topological classification, non-Hermitian systems exhibit a richer variety of topological phases, increasing from 10 classes in Hermitian systems to 38 classes [43, 44].

The symmetry classification of non-Hermitian systems is summarized in Table 4.1. Categories lacking time-reversal symmetry and particle-hole symmetry are collectively referred to as the Complex AZ class. In contrast, categories incorporating TRS and PHS, along with chiral symmetry (CS), are termed the Real AZ class. Notably, classifications based on TRS† and PHS†, together with CS, are referred to as the Real AZ† class, which is unique to non-Hermitian systems.

Table 4.1: The table of AZ and AZ† classification for non-Hermition Hamiltonians. For TRS (TRS†) and PHS (PHS†), ±1 indicate the value of $\mathcal{T}_\pm\mathcal{T}_\pm^*$ or $\Xi_\pm\Xi_\pm^*$, while 0 represents the absence of the symmetry. For CS, 1 and 0 denote whether the system has CS or not.

Symmetry class		TRS ($\mathcal{T}_+$)	PHS ($\mathcal{C}_+$)	TRS† ($\mathcal{T}_-$)	PHS† ($\mathcal{C}_-$)	CS (Γ)
Complex AZ	A	0	0	0	0	0
	AIII	0	0	0	0	1
Real AZ	AI	+1	0	0	0	0
	BDI	+1	+1	0	0	1
	D	0	+1	0	0	0
	DIII	-1	+1	0	0	1
	AII	-1	0	0	0	0
	CII	-1	-1	0	0	1
	C	0	-1	0	0	0
	CI	+1	-1	0	0	1
Real AZ†	AI†	0	0	+1	0	0
	BDI†	0	0	+1	+1	1
	D†	0	0	0	+1	0
	DIII†	0	0	-1	+1	1
	AII†	0	0	-1	0	0
	CII†	0	0	-1	-1	1
	C†	0	0	0	-1	0
	CI†	0	0	+1	-1	1

Table 4.2 summarizes the types of point-gap topology, real line-gap topology, and imaginary line-gap topology in AZ† class systems across different dimensions, along with their corresponding classification spaces. The coupled HN model introduced in Sec. 4.4 exhibits only spinful TRS†, which places it in class AII†, leading to a $\mathbb{Z}_2$ point-gap topology.

For non-Hermitian systems with SLS, the topological phases can be further classified based on the AZ symmetry classes, incorporating additional SLS. This classification depends on the relationship between the TRS or PHS operators and the SLS operator, specifically whether they commute or anti-commute:

$$S\mathcal{X} = \pm\mathcal{X}S^*, \tag{4.31}$$

where $\mathcal{X}$ represents a symmetry operator (e.g., TRS or PHS), and S denotes the SLS operator. To be convenient, we use the notation $S_\pm$ to indicate the sign on the right-hand side of the equation.

Table 4.2: Classification of topological types for d-dimensional non-Hermitian systems in the real AZ† class.Here, P represents point gaps, and L denotes line gaps, with the subscripts r and i indicating real and imaginary line gaps, respectively. The notation $2\mathbb{Z}$ signifies an even $\mathbb{Z}$ topological invariant, while $\mathbb{Z}\oplus\mathbb{Z}$ ($\mathbb{Z}_2\oplus\mathbb{Z}_2$) indicates the presence of two independent $\mathbb{Z}$ ($\mathbb{Z}_2$) topological invariants.

AZ† class	Gap	Classifying space	$d=0$	$d=1$	$d=2$	$d=3$	$d=4$
AI†	P	$\mathcal{R}_7$	0	0	0	$2\mathbb{Z}$	0
	L	$\mathcal{R}_0$	$\mathbb{Z}$	0	0	0	$2\mathbb{Z}$
BDI†	P	$\mathcal{R}_0$	$\mathbb{Z}$	0	0	0	$2\mathbb{Z}$
	$\mathrm{L_r}$	$\mathcal{R}_1$	$\mathbb{Z}_2$	$\mathbb{Z}$	0	0	0
	$\mathrm{L_i}$	$\mathcal{R}_0\times\mathcal{R}_0$	$\mathbb{Z}\oplus\mathbb{Z}$	0	0	0	$2\mathbb{Z}\oplus2\mathbb{Z}$
D†	P	$\mathcal{R}_1$	$\mathbb{Z}_2$	$\mathbb{Z}$	0	0	0
	$\mathrm{L_r}$	$\mathcal{R}_2$	$\mathbb{Z}_2$	$\mathbb{Z}_2$	$\mathbb{Z}$	0	0
	$\mathrm{L_i}$	$\mathcal{R}_0$	$\mathbb{Z}$	0	0	0	$2\mathbb{Z}$
DIII†	P	$\mathcal{R}_2$	$\mathbb{Z}_2$	$\mathbb{Z}_2$	$\mathbb{Z}$	0	0
	$\mathrm{L_r}$	$\mathcal{R}_3$	0	$\mathbb{Z}_2$	$\mathbb{Z}_2$	$\mathbb{Z}$	0
	$\mathrm{L_i}$	C_0	$\mathbb{Z}$	0	$\mathbb{Z}$	0	$\mathbb{Z}$
AII†	P	$\mathcal{R}_3$	0	$\mathbb{Z}_2$	$\mathbb{Z}_2$	$\mathbb{Z}$	0
	L	$\mathcal{R}_4$	$2\mathbb{Z}$	0	$\mathbb{Z}_2$	$\mathbb{Z}_2$	$\mathbb{Z}$
CII†	P	$\mathcal{R}_4$	$2\mathbb{Z}$	0	$\mathbb{Z}_2$	$\mathbb{Z}_2$	$\mathbb{Z}$
	$\mathrm{L_r}$	$\mathcal{R}_5$	0	$2\mathbb{Z}$	0	$\mathbb{Z}_2$	$\mathbb{Z}_2$
	$\mathrm{L_i}$	$\mathcal{R}_4\times\mathcal{R}_4$	$2\mathbb{Z}\oplus2\mathbb{Z}$	0	$\mathbb{Z}_2\oplus\mathbb{Z}_2$	$\mathbb{Z}_2\oplus\mathbb{Z}_2$	$\mathbb{Z}\oplus\mathbb{Z}$
C†	P	$\mathcal{R}_5$	0	$2\mathbb{Z}$	0	$\mathbb{Z}_2$	$\mathbb{Z}_2$
	$\mathrm{L_r}$	$\mathcal{R}_6$	0	0	$2\mathbb{Z}$	0	$\mathbb{Z}_2$
	$\mathrm{L_i}$	$\mathcal{R}_4$	$2\mathbb{Z}$	0	$\mathbb{Z}_2$	$\mathbb{Z}_2$	$\mathbb{Z}$
CI†	P	$\mathcal{R}_6$	0	0	$2\mathbb{Z}$	0	$\mathbb{Z}_2$
	$\mathrm{L_r}$	$\mathcal{R}_7$	0	0	0	$2\mathbb{Z}$	0
	$\mathrm{L_i}$	C_0	$\mathbb{Z}$	0	$\mathbb{Z}$	0	$\mathbb{Z}$

Table 4.3 summarizes the symmetry classification for non-Hermitian systems with SLS. For Hamiltonians possessing both TRS and PHS, each class can be divided into four cases based on whether SLS commutes or anti-commutes with the TRS and PHS operators, denoted as $S_{\pm\pm}$. However, some of these cases overlap with other symmetry classes (e.g., DII+S_{-+}), leaving only 12 unique classes in this category.

For symmetry classes with only one of TRS or PHS, each class exhibits two types of SLS. However the class AI+S_- is duplicated. In systems that lack both TRS and PHS, there are two symmetry types depending on the presence or absence of CS. Within the AIII class, which includes CS, two cases emerge depending on whether SLS commutes or anti-commutes with the

Table 4.3: Classification of topological phases for non-Hermitian systems with SLS based on the AZ symmetry classes. For TRS and PHS, ±1 indicate the value of $\mathcal{TT}^*$ or $\Xi\Xi^*$, while 0 represents the absence of the symmetry. $S_{\pm\pm}$ specifies whether TRS and PHS operators commute or anti-commute with SLS operator. Notably, in the A+S case, SLS is not distinguished due to the absence of both TRS and PHS.

TRS \ PHS	+1	-1	0
+1	BDI + S_{++} S_{+-} S_{-+} S_{--}	CI + S_{++} S_{+-} S_{-+} S_{--}	AI + S_+
-1	DII + S_{++} S_{+-}	CII + S_{++} S_{+-}	AII + S_+ S_-
0	D + S_+ S_-	C + S_+ S_-	A + S AIII + S_+ S_-

CS operator. In contrast, for the A class, which lacks all symmetries, we do not distinguish S_+ and S_-.

Overall, non-Hermitian systems with SLS exhibit 22 distinct symmetry classes. When combined with the 10 classes of the AZ symmetry classification and the 6 classes of the AZ† symmetry classification, the total number of symmetry classes for non-Hermitian systems amounts to 38. Similar to Hermitian systems, symmetry classification plays a crucial role in understanding the topological properties of non-Hermitian systems. However, our recent research indicates that the classification of non-Hermitian topological systems extends beyond these 38 classes. In Chapter 5, starting from Floquet systems, we expand the symmetry classification of non-Hermitian systems into what we term dual symmetry classification.

4.6 Purpose of this thesis

In the preceding chapters, we have explained both Hermitian and non-Hermitian topological phases, highlighting their novel physical phenomena. Notably, $\mathbb{Z}_2$ topology plays a pivotal role in a wide range of Hermitian systems. For instance, the proposal of the QSHI in 2005 [8, 9] has significantly advanced the study of topological phases, while Majorana fermions in $\mathbb{Z}_2$ topological superconductors are essential candidates for fault-tolerant quantum computing. Building

on these developments, we believe that the non-Hermitian analogue, $\mathbb{Z}_2$ point-gap topology, also holds considerable promise for practical applications. However, the concept of $\mathbb{Z}_2$ point-gap topology has only recently been introduced in [43, 54]; it has yet to be experimentally observed, and even theoretical investigations remain scarce. Therefore, this doctoral thesis aims to establish the theoretical framework, explore potential experimental realizations, and investigate possible applications of $\mathbb{Z}_2$ point-gap topology from several complementary perspectives.

A key experimental challenge in non-Hermitian systems is that the eigenenergies of the Hamiltonian are complex, making direct observation and measurement more demanding. In recent years, nonunitary quantum walks have emerged as a promising platform for probing non-Hermitian dynamics and topological phenomena, as they incorporate multiple controllable parameters with high precision. In a standard (unitary) quantum walk, a walker moves on a lattice through successive unitary operations. By contrast, nonunitary quantum walks introduce gain and loss, resulting in non-Hermitian dynamics. Such systems have already been experimentally realized using temporally alternating photon losses. Despite this progress, most current research in the context of quantum walks focuses on systems characterized by $\mathbb{Z}$ point-gap topology, leaving the $\mathbb{Z}_2$ invariant relatively unexplored. One of the objectives of this thesis is thus to design a nonunitary quantum walk that exhibits $\mathbb{Z}_2$ point-gap topology and propose a feasible experimental setup, thereby opening a pathway for the first direct observation of $\mathbb{Z}_2$ point-gap topology.

Beyond experimental realizations, non-Hermitian topological phases can offer conceptual advantages over their Hermitian counterparts. Because the eigenenergy spectrum of non-Hermitian Hamiltonians lies in the complex plane, topological invariants in one-dimensional systems can be defined directly in terms of the relationship between the energy spectrum and a reference point, which is often more intuitive than defining topological invariants in Hermitian systems. If a one-to-one correspondence can be established between the real-energy gap in a Hermitian Hamiltonian and the point gap in a non-Hermitian Hamiltonian, the Hermitian system itself can be understood more intuitively by mapping it onto a corresponding non-Hermitian framework. Accordingly, this thesis also investigates a Hermitian system in which non-Hermitian concepts elucidate the physical behavior. In particular, we focus on a stacked system comprising a $\mathbb{Z}_2$ topological insulator and demonstrate how the robustness of $\mathbb{Z}_2$ topology is preserved under stacking. Through this analysis, we aim to provide deeper insight into how non-Hermitian physics can

inform the understanding of Hermitian topological phases.

Overall, this work endeavors to bridge theoretical insights and experimental realizations of $\mathbb{Z}_2$ point-gap topology, while illustrating how non-Hermitian perspectives can enhance our grasp of topological phenomena in both Hermitian and non-Hermitian contexts.

Chapter 5

Dual Symmetry Classification for Non-Hermitian Systems

5.1 Introduction

Non-Hermitian systems exhibit richer topological properties compared to their Hermitian counterparts, as demonstrated in Chapter 4. It is well known that non-Hermitian systems have been classified based on either the symmetry relations for non-Hermitian Hamiltonians or the symmetry relations for nonunitary time-evolution operators in the context of Floquet topological phases [151, 152]. In this chapter, we propose that non-Hermitian systems can always be classified in two ways; a non-Hermitian system can be classified using the symmetry relations for non-Hermitian Hamiltonians or time-evolution operator regardless of the Floquet topological phases or not. We refer to this as *dual symmetry classification*. Section 5.2 provides a review of Floquet topological phases, and in Sec. 5.3, we introduce dual symmetry classification to expand the symmetry classification of non-Hermitian systems.

5.2 Classification for Floquet systems

In the study of topological phases, it is found that the nontrivial topological phase can be induced by periodically driving a system, which is known as the Floqeut topological phase [153–157]. For the Floquet topological phase, symmetry should be defined through the time-evolution operator, not the instantaneous Hamiltonian since the time dependence of the Hamiltonian is crucial to retain the symmetry. Therefore, taking into account the relation between the Floquet

effective Hamiltonian $H_{\text{eff}}(k)$ and the time-evolution operator $U(k)$,

$$U(k) = e^{-iH_{\text{eff}}(k)}, \tag{5.1}$$

the aforementioned relationships of symmetry in Eq. (4.30) can be reformulated as

$$\mathcal{T}_+ U^*(k)\mathcal{T}_+^{-1} = U^{-1}(-k) \qquad \text{(TRS)}, \tag{5.2a}$$

$$\mathcal{T}_- U^T(k)\mathcal{T}_-^{-1} = U(-k), \qquad \text{(TRS}^\dagger\text{)} \tag{5.2b}$$

$$\Xi_+ U^T(k)\Xi_+^{-1} = U^{-1}(-k) \qquad \text{(PHS)}, \tag{5.2c}$$

$$\Xi_- U^*(k)\Xi_-^{-1} = U(-k) \qquad \text{(PHS}^\dagger\text{)}, \tag{5.2d}$$

$$\Gamma U^\dagger(k)\Gamma^{-1} = U(k) \qquad \text{(CS)}, \tag{5.2e}$$

$$S\,U(k)S^{-1} = U^{-1}(k) \qquad \text{(SLS)}. \tag{5.2f}$$

where $U(k)$ stands for a nonunitary time-evolution operator in the momentum space. The quasi-energy is defined by the eigenvalue equation of $U(k)$

$$U|\phi\rangle = \lambda|\phi\rangle = e^{-i\varepsilon}|\phi\rangle. \tag{5.3}$$

For a nonunitary time-evolution operator, in general, $|\lambda| \neq 1$ and ε is complex.

5.3 Dual symmetry classification

While it is well known that the classifications based on the above symmetry relations in Eqs. (4.30) and (5.2) correctly predicts nontrivial topological phases in non-Hermitian systems, here, we propose alternative way to classify the non-Hermitian systems based on the fact that there is no strict difference in mathematical definition between non-Hermitian Hamiltonians and nonunitary time-evolution operators. By regarding a given non-Hermitian Hamiltonian $H(k)$ as a nonunitary time-evolution operator $U(k)$, the non-Hermitian Hamiltonian can be classified by symmetries defined in Eq. (5.2). In the same way, regarding a nonunitary time-evolution operator $U(k)$ as an non-Hermitian Hamiltonian $H(k)$, the nonunitary time-evolution operator can be classified by Eq. (4.30). This means that there are always two ways to classify a given Hamiltonian or a time-evolution operator in non-Hermitian systems, which we call dual symmetry classification.

Table 5.1: A list of the symmetry relations. For the dual symmetry classification we represent either a non-Hermitian Hamiltonian or a nonunitary time-evolution operator for the non-Hermitian system as $X(k)$.

Symmetry class	Hamiltonian Ref. [43]	Time-evolution operator Ref. [151]
TRS	$\mathcal{T}_+ H^*(k)\mathcal{T}_+^{-1} = H(-k)$	$\mathcal{T}_+ U^*(k)\mathcal{T}_+^{-1} = U^{-1}(-k)$
TRS†	$\mathcal{T}_- H^T(k)\mathcal{T}_-^{-1} = H(-k)$	$\mathcal{T}_- U^T(k)\mathcal{T}_-^{-1} = U(-k)$
PHS	$\Xi_+ H^T(k)\Xi_+^{-1} = -H(-k)$	$\Xi_+ U^T(k)\Xi_+^{-1} = U^{-1}(-k)$
PHS†	$\Xi_- H^*(k)\Xi_-^{-1} = -H(-k)$	$\Xi_- U^*(k)\Xi_-^{-1} = U(-k)$
CS	$\Gamma H^\dagger(k)\Gamma^{-1} = -H(k)$	$\Gamma U^\dagger(k)\Gamma^{-1} = U(k)$
SLS	$S H(k)S^{-1} = -H(k)$	$S U(k)S^{-1} = U^{-1}(k)$
Symmetry class	Dual symmetry classification H-type, Ref. [62]	Dual symmetry classification U-type, Ref. [62]
TRS	$\mathcal{T}_+ X^*(k)\mathcal{T}_+^{-1} = X(-k)$	$\mathcal{T}_+ X^*(k)\mathcal{T}_+^{-1} = X^{-1}(-k)$
TRS†	$\mathcal{T}_- X^T(k)\mathcal{T}_-^{-1} = X(-k)$	$\mathcal{T}_- X^T(k)\mathcal{T}_-^{-1} = X(-k)$
PHS	$\Xi_+ X^T(k)\Xi_+^{-1} = -X(-k)$	$\Xi_+ X^T(k)\Xi_+^{-1} = X^{-1}(-k)$
PHS†	$\Xi_- X^*(k)\Xi_-^{-1} = -X(-k)$	$\Xi_- X^*(k)\Xi_-^{-1} = X(-k)$
CS	$\Gamma X^\dagger(k)\Gamma^{-1} = -X(k)$	$\Gamma X^\dagger(k)\Gamma^{-1} = X(k)$
SLS	$S X(k)S^{-1} = -X(k)$	$S X(k)S^{-1} = X^{-1}(k)$

For example, the symmetry class of a give time-evolution operator is determined by the relations in Eqs. (4.30a)-(4.30f) or the relations in Eqs. (5.2a) - (5.2f). To avoid confusion, we call the former (latter) scheme for the classification as the H-type (U-type) classification. For the sake of completeness, we summarize all the symmetry relations in Table 5.1.

Note that Eq. (4.30b) and Eq. (5.2a) for TRS† are the same. In addition, Eq. (4.30a) for TRS and Eq. (5.2d) for PHS† are the same. We also note the inverse of the operator on the right-hand side in Eqs. (5.2a), (5.2c), and (5.2f) for U-type symmetry requires the strong constraints on the Hamiltonian. However, the minus sign on the right-hand side in Eqs. (4.30c)-(4.30f) for H-type symmetry requires the time-evolution operator only shifting the quasi-energy by π.

Here, we consider an example described by a non-Hermitian Hamiltonian:

$$H(k) = \begin{pmatrix} e^{\gamma}e^{ik} & \sqrt{e^{2\gamma}-1} \\ \sqrt{e^{2\gamma}-1} & e^{\gamma}e^{-ik} \end{pmatrix}, \tag{5.4}$$

whose inverse is given by

$$H^{-1}(k) = \begin{pmatrix} e^{\gamma}e^{-ik} & -\sqrt{e^{2\gamma}-1} \\ -\sqrt{e^{2\gamma}-1} & e^{\gamma}e^{ik} \end{pmatrix}, \tag{5.5}$$

where γ is a real number.

According to our dual symmetry classification, there are always two approaches to classifying such a Hamiltonian. From the relationships in Eqs. (4.30a)-(4.30f), we find that $H(k)$ satisfies only the spinless TRS with $\mathcal{T}_+ = \sigma_0$. In this case, it falls into class AI, featuring a $\mathbb{Z}$ point-gap topology and a $\mathbb{Z}_2$ imaginary line-gap topology. Alternatively, by interpreting $H(k)$ as a nonunitary time-evolution operator, and using the relationships in Eqs. (5.2a) - (5.2f), we see that it satisfies spinful TRS with $\mathcal{T}_+ = \sigma_y$, spinless PHS with $\Xi_+ = \sigma_z$ and CS with $\Gamma = \sigma_x$. From this perspective, it belongs to class DIII, which is characterized by a $\mathbb{Z}_2$ real line-gap topology. This demonstrates that our dual symmetry classification approach refines the topological classification of non-Hermitian systems and enriches their topological phases.

In Chapter 6, we demonstrate the validity of the dual symmetry classification by considering a nonunitary time-evolution operator defined for a quantum walk.

Chapter 6

Non-unitary Quantum Walks with $\mathbb{Z}_2$ Point-gap Topology

6.1 Introduction

One promising area of exploration within topology of non-Hermitian physics is the study of nonunitary quantum walks [151, 158–162]. The discrete-time quantum walk consists of a walker moving on a lattice, obeying a unitary time-evolution operator with each time step [163–169]. However, the nonunitary quantum walks incorporate gain and loss, resulting in non-Hermitian Hamiltonian dynamics. It is known that the nonunitary time-evolution operator can be classified by translating the symmetry relations of Hamiltonians to time-evolution operators. Some models of nonunitary quantum walks have been realized theoretically [151, 158, 160, 162] and experimentally [159, 161] by temporally alternating photon losses. However, there is no research focused on the topological properties of time-reversal symmetric no-Hermitian system with nontrivial $\mathbb{Z}_2$ point-gap topology.

In this chapter, we introduce a nonunitary quantum walk with spinful time-reversal symmetry and $\mathbb{Z}_2$ point gap topology by proposing the alternative symmetry classification way which we call as dual symmetry classification, which is introduced in Chapter 5. By using this new classification scheme, we introduce a nonunitary quantum walk with spinful time-reversal symmetry. We find that the nonunitary quantum walk has $\mathbb{Z}_2$ point gap with nontrivial $\mathbb{Z}_2$ topological invariant. We confirm that the nonunitary quantum walk satisfies BBC and the eigenstates are localized at both boundaries, indicating the $\mathbb{Z}_2$ NHSE.

This chapter is organized as follows. In Sec.6.2, we introduce quantum walks, the quantum counterpart of random walks, and construct a nonunitary quantum walk by incorporating a gain-loss operator to simulate an open system. In Sec.6.3, we define a nonunitary quantum walk with spinful time-reversal symmetry† and discuss the symmetry class of the system. Moreover, we propose methods of experimental realization of our quantum walk. In Sec.6.4.1 we calculate the $\mathbb{Z}_2$ point gap topological invariant of the nonunitary quantum walk and validate that when the quantum walk possesses a nontrivial $\mathbb{Z}_2$ topology, the eigenvalue spectrum of the time evolution operator under reflecting boundary conditions resides within the spectrum under periodic boundary conditions. Simultaneously, the eigenstates are localized near the boundaries of the system, indicating the emergence of the $\mathbb{Z}_2$ NHSE. In Sec.6.4.2, we study a junction system comprised of two topologically nontrivial quantum walks with inhomogeneous parameters in real space. Intriguingly, we find that both subsystems exhibit skin effects even under periodic boundary conditions.

6.2 Non-unitary quantum walks

Random walks are statistical models describing a series of random steps taken by a particle from its origin. They are widely used in computational algorithms to address complex problems in computer science, finance, and physics. Random walks can be classified based on time progression: continuous-time random walks, such as Brownian motion and the drunkard's walk, and discrete-time random walks, such as a Galton board, shown in Fig. 6.1(a). In a Galton board, a ball released from the top falls through layers of pegs, with a 50% chance of bouncing left or right at each peg. By the time it reaches the bottom, the ball's position follows a Gaussian distribution, peaking at the center.

Quantum walks are the quantum analogs of classical random walks. Fig. 6.1(b) illustrates a quantum extension of the Galton board. Unlike the classical case, where the ball follows distinct paths, the quantum system allows the ball to exist in a superposition of moving left and right at each step. This superposition results in interference during the descent, producing a probability distribution that differs fundamentally from the classical Gaussian distribution after enough steps. This quantum distribution is often referred to as the Konno distribution.

Now, we consider a particle that is treated as a "walker" in a quantum walk. The state of the

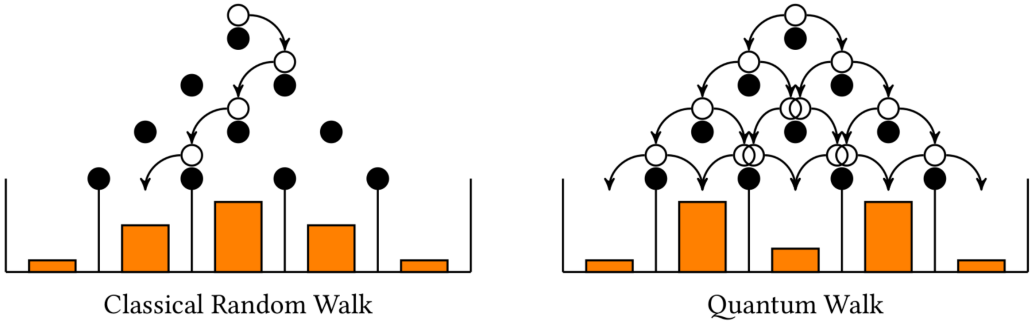

Figure 6.1: Schematic of a Galton board for (a) a classical random walk and (b) a quantum walk. This figure is reproduced from Ref. [170].

walker, denoted as $|\psi\rangle$ is represented as the tensor product of its position state $|x \in \mathbb{Z}\rangle$ and the coin state $|s\rangle$, expressed as

$$|\psi\rangle = \sum_{x,s} |x\rangle \otimes |s\rangle, \tag{6.1}$$

where the coin state $|s\rangle$ is an internal state written as a superposition of the basis states $|L\rangle = (1,0)^T$ and $|R\rangle = (0,1)^T$.

A simple quantum walk process involves two fundamental operators: the coin operator C and the shift operator S. The coin operator acts only on the coin state and performs a rotation to simulate the process of tossing a coin. It is defined as

$$C[\theta(x)] = \sum_{x} |x\rangle\langle x| \otimes e^{-i\theta(x)\sigma_y} = \sum_{x} |x\rangle\langle x| \otimes \begin{pmatrix} \cos\theta(x) & \sin\theta(x) \\ -\sin\theta(x) & cos\theta(x) \end{pmatrix}, \tag{6.2}$$

where σ_y is the Pauli matrix, indicating that the coin state is rotated by an angle $\theta(x)$ about the y axis.

Following the coin operation, the walker moves based on its internal state. If the coin state is $|L\rangle$, the walker moves one step to the left, whereas if the coin state is $|R\rangle$, the walker moves one step to the right. This movement is implemented by the shift operator S, which is expressed as

$$S = \sum_{x,s} |x-1\rangle\langle x| \otimes |L\rangle\langle L| + |x+1\rangle\langle x| \otimes |R\rangle\langle R|. \tag{6.3}$$

In some cases, the shift operator can also be written in terms of split-step shift operators. These

are defined as

$$S_- = \sum_{x,s} |x-1\rangle\langle x| \otimes |L\rangle\langle L| + |x\rangle\langle x| \otimes |R\rangle\langle R|, \tag{6.4}$$

$$S_+ = \sum_{x,s} |x\rangle\langle x| \otimes |L\rangle\langle L| + |x+1\rangle\langle x| \otimes |R\rangle\langle R|, \tag{6.5}$$

with the relationship $S = S_- S_+$. By combining the coin operator and the shift operator, the time-evolution operator for the quantum walk is defined as

$$U = S\,C[\theta(x)]. \tag{6.6}$$

We assume that the initial state of the walker is $|\psi(0)\rangle$. After one step of the quantum walk, the state of the walker is given by $|\psi(1)\rangle = U|\psi(0)\rangle$. After t steps, the state of the walker is expressed as

$$|\psi(t)\rangle = U^t|\psi(0)\rangle. \tag{6.7}$$

Similar to the tight-binding model, the quantum walk model often employs operators in the momentum representation to analyze systems under PBCs when $\theta(x)$ is homogeneous in real space. By applying the Fourier transform $|x\rangle = \frac{1}{\sqrt{N}} \sum_k e^{ikx}|k\rangle$, the time-evolution operator can be easily diagonalized in momentum space, resulting in:

$$C(\theta) = \sum_k |k\rangle\langle k| \otimes \widetilde{C}(\theta), \quad \widetilde{C}(\theta) = e^{-i\theta\sigma_y}, \tag{6.8}$$

$$S = \sum_k |k\rangle\langle k| \otimes \widetilde{S}, \quad \widetilde{S} = \begin{pmatrix} e^{ik} & \\ & e^{-ik} \end{pmatrix}, \tag{6.9}$$

$$U = \sum_k |k\rangle\langle k| \otimes \widetilde{U}, \quad \widetilde{U} = \widetilde{S}\widetilde{C}(\theta) = \begin{pmatrix} e^{ik}\cos\theta & e^{ik}\sin\theta \\ -e^{-ik}\sin\theta & e^{-ik}\cos\theta \end{pmatrix}. \tag{6.10}$$

To simulate asymmetric hopping in non-Hermitian tight-binding models (e.g., the Hatano-Nelson model), we can introduce gain and loss acting on different internal states in the quantum walk. This operator, referred to as the gain-loss operator, is represented as

$$G = \sum_x |x\rangle\langle x| \otimes \begin{pmatrix} e^{\gamma} & \\ & e^{\gamma} \end{pmatrix}. \tag{6.11}$$

Here γ characterizes the degree of nonunitarity, and the gain-loss operator satisfies $G^\dagger \neq G^{-1}$. For

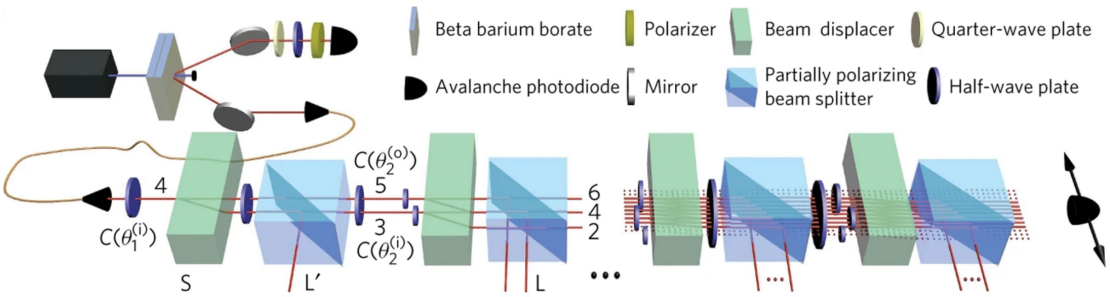

Figure 6.2: Experimental setup for realizing a nonunitary quantum walk, as demonstrated in Ref. [159].

$\gamma > 0$, $G|x, L\rangle = e^{\gamma}|x, L\rangle$ corresponds to gain in the system, while $G|x, L\rangle = e^{-\gamma}|x, R\rangle$ represents loss.

By introducing the gain-loss operator, we can define a nonunitary quantum walk, where the time-evolution operator is given by

$$U = GSC[\theta(x)]. \tag{6.12}$$

The nonunitary quantum walk has been experimentally realized on an optical platform, as demonstrated in Ref. [159]. In their implementation, the walker is represented by entangled photon pairs, while the coin operator and shift operator are realized using half-wave plates and beam displacers, respectively, as shown in Fig. 6.2.

In realistic systems, implementing gain is highly challenging. Therefore, the experiment focuses solely on the loss process, which is realized using a partially polarizing beam splitter. The corresponding loss operator is defined as

$$L = \sum_x |x\rangle\langle x| \otimes \begin{pmatrix} 1 & \\ & \sqrt{P} \end{pmatrix}, \tag{6.13}$$

where P represents the probability that the walker in the $|R\rangle$ internal state is not reflected by the partially polarizing beam splitter, while walker in the $|L\rangle$ internal state passes straight through the prism without being reflected.

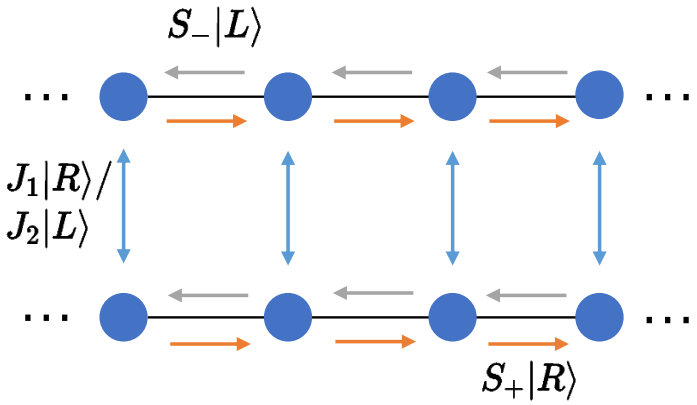

Figure 6.3: The schematic view of the movement of the walker in the nonunitary quantum walk in Eq. (6.31). The walker is moving on a pair of parallel chains. The horizontal movement of the walker along the chain is controlled by S operator, while the jump to the other chain is controlled by J operator.

6.3 A model of nonunitary quantum walk with time-reversal symmetry

In this section, we introduce a nonunitary discrete-time quantum walk to demonstrate the dual symmetry classification for the time-evolution operator. Due to the reason explained in Sec. 6.4, we call this quantum walk the nonunitary quantum walk with $\mathbb{Z}_2$ point-gap topology.

6.3.1 Real space representation

We consider a particle with two internal degrees of freedom, which a walker of the quantum walk, moving on a pair of parallel chains, a and b, which is important to realize TRS† with $\mathcal{T}_-\mathcal{T}_-^* = -1$, as we demonstrate later. The state of the walker can be defined as

$$|\psi(t)\rangle = \sum_{x,n,s} \psi_{x,n,s}(t)\,|x\rangle \otimes |n\rangle \otimes |s\rangle\,. \tag{6.14}$$

Here, $|x\rangle$ where $x \in \mathbb{Z}$ represents the position space, $|n = a, b\rangle$ represents the chain space, and $|s = L, R\rangle$ represents the internal state space where two basic vectors of the internal state of the walker is $|L\rangle = (1, 0)^T$ and $|R\rangle = (0, 1)^T$. The dynamics of a quantum walk are described by a time-evolution operator U periodically operating on the wave function of the walker. After t steps, the state of walker can be written as $|\psi(t)\rangle = U^t|\psi(0)\rangle$.

A standard quantum walk within one period involves at least two operators: the coin operator and the shift operator. These operators serve to simulate the processes of coin flipping and the movement of the walker, respectively. We define the coin operator C as a rotation operation in the opposite direction of the internal state on different chains, which can be expressed as

$$C_{\alpha=x,y}[\theta(x)] = \sum_x |x\rangle\langle x| \otimes e^{-i\theta(x)\tau_z \otimes \sigma_\alpha} \tag{6.15}$$

$$= \sum_x |x\rangle\langle x| \otimes \begin{pmatrix} e^{-i\theta(x)\sigma_\alpha} & 0 \\ 0 & e^{i\theta(x)\sigma_\alpha} \end{pmatrix}, \tag{6.16}$$

where the Pauli matrix $\sigma_{x,y,z}$ ($\tau_{x,y,z}$) acts on the internal states space $|s\rangle$ (the chain space $|n\rangle$). The subscript $\alpha = x, y$ indicates the rotation around the x or y axis with the rotation angle $\theta(x)$ which may depend on the position x.

The movement of the walker along the same chain is determined by the shift operators. The shift operators change the position $|x\rangle$ depending on the initinal states, are given by

$$S_- = \sum_x \left(|x-1\rangle\langle x| \otimes \tau_0 \otimes |L\rangle\langle L| + |x\rangle\langle x| \otimes \tau_0 \otimes |R\rangle\langle R|\right), \tag{6.17}$$

$$S_+ = \sum_x \left(|x\rangle\langle x| \otimes \tau_0 \otimes |L\rangle\langle L| + |x+1\rangle\langle x| \otimes \tau_0 \otimes |R\rangle\langle R|\right), \tag{6.18}$$

where τ_0 represent the 2×2 indentity matrix acting on the chain space. Here, we take periodic boundary condition to ensure that the shift operator is unitary.

We introduce another operator representing the hopping between the two chains that we refer to as the jump operator $J_{1,2}$. This operator determines whether the walker jumps to another chain depending on the internal state. The jump operators $J_{1,2}$ can be expressed as follows:

$$J_1 = \sum_x |x\rangle\langle x| \otimes \left[\tau_0 \otimes |L\rangle\langle L| + (|b\rangle\langle a| + |a\rangle\langle b|) \otimes |R\rangle\langle R|\right], \tag{6.19}$$

$$J_2 = \sum_x |x\rangle\langle x| \otimes \left[(|b\rangle\langle a| + |a\rangle\langle b|) \otimes |L\rangle\langle L| + \tau_0 \otimes |R\rangle\langle R|\right]. \tag{6.20}$$

The movement of the walker by the shift operator $S_\pm$ and the jump operator $J_{1,2}$ are schematically shown in Fig.6.3.

To incorporate nonunitary dynamics into the quantum walk, we introduce a nonunitary gain-

loss operator

$$G = \sum_x |x\rangle\langle x| \otimes e^{\gamma\tau_z \otimes \sigma_z} \tag{6.21}$$

$$= \sum_x |x\rangle\langle x| \otimes \begin{pmatrix} e^{\gamma\sigma_z} & 0 \\ 0 & e^{-\gamma\sigma_z} \end{pmatrix}, \tag{6.22}$$

which accounts for the phenomenological gain and loss of amplitudes, while γ represents the strength of non-unitarity of the quantum walk.

Using the above operators, we define the time evolution operator of our quantum walk in a time-symmetric frame as

$$U = C_y\left[\theta_3(x)/2\right] S_+ C_y[\theta_1(x)] J_2 C_x[\theta_2(x)] G C_x[\theta_2(x)] J_1 C_y[\theta_1(x)] S_- C_y\left[\theta_3(x)/2\right]. \tag{6.23}$$

When we set the value of θ_3 at the boundary to be $\pi/2$, the walker cannot move from one side boundary to the other. In this case, the boundary conditions are referred to as reflecting boundary conditions (RBC), which can also be viewed as OBC in a tight-binding model.

6.3.2 Momentum space representation

If the parameter $\theta(x)$ in Eq. (6.16) and γ in Eq. (6.22) are constant over the position x, the time-evolution operator U possesses translation symmetry and can be diagonal in the momentum space $|k\rangle$ by the Fourier transformation of the basic operators over the real space $|x\rangle$, yielding:

$$C_\alpha[\theta] = \sum_k |k\rangle\langle k| \otimes \widetilde{C}_\alpha(\theta),\ \widetilde{C}_\alpha(\theta) = \begin{pmatrix} e^{-i\theta\sigma_\alpha} & 0 \\ 0 & e^{i\theta\sigma_\alpha} \end{pmatrix}, \tag{6.24}$$

$$S_- = \sum_k |k\rangle\langle k| \otimes \widetilde{S}_-(k),\ \widetilde{S}_-(k) = \begin{pmatrix} e^{ik} & & & \\ & 1 & & \\ & & e^{ik} & \\ & & & 1 \end{pmatrix}, \tag{6.25}$$

$$S_+ = \sum_k |k\rangle\langle k| \otimes \widetilde{S}_+(k),\ \widetilde{S}_+(k) = \begin{pmatrix} 1 & & & \\ & e^{-ik} & & \\ & & 1 & \\ & & & e^{-ik} \end{pmatrix}, \tag{6.26}$$

$$J_1 = \sum_k |k\rangle\langle k| \otimes \widetilde{J}_1,\ \widetilde{J}_1 = \begin{pmatrix} 0 & 0 & 1 & 0 \\ 0 & 1 & 0 & 0 \\ 1 & 0 & 0 & 0 \\ 0 & 0 & 0 & 1 \end{pmatrix}, \tag{6.27}$$

$$J_2 = \sum_k |k\rangle\langle k| \otimes \widetilde{J}_2,\ \widetilde{J}_2 = \begin{pmatrix} 1 & 0 & 0 & 0 \\ 0 & 0 & 0 & 1 \\ 0 & 0 & 1 & 0 \\ 0 & 1 & 0 & 0 \end{pmatrix}, \tag{6.28}$$

$$G = \sum_k |k\rangle\langle k| \otimes \widetilde{G},\ \widetilde{G} = \begin{pmatrix} e^{\gamma\sigma_z} & 0 \\ 0 & e^{-\gamma\sigma_z} \end{pmatrix}, \tag{6.29}$$

with time evolution operator

$$U = \sum_k |k\rangle\langle k| \otimes \widetilde{U}(k), \tag{6.30}$$

$$\widetilde{U}(k) = \widetilde{C}_y\left(\theta_3/2\right)\widetilde{S}_+\widetilde{C}_y(\theta_1)\widetilde{J}_2\widetilde{C}_x(\theta_2)\widetilde{G}\widetilde{C}_x(\theta_2)\widetilde{J}_1\widetilde{C}_y(\theta_1)\widetilde{S}_-\widetilde{C}_y\left(\theta_y/2\right). \tag{6.31}$$

6.3.3 Symmetry

Here, we examine the symmetry of the nonunitary time-evolution operator $\tilde{U}(k)$ in Eq. (6.31) according to our proposal in Sec. 5.3. First, we observe that the operator $\widetilde{U}(k)$ fulfills spinful TRS† in H type in Eq. (4.30b) with $\mathcal{T}_- = \tau_x \otimes \sigma_y$ where $\mathcal{T}_-\mathcal{T}_-^* = -1$. Thus, the operator $\tilde{U}(k)$ also satisfies the TRS† in U type in Eq. (5.2b) since both relations are identical. Due to spinful TRS†, the eigenvalue of $\tilde{U}(k)$ is always double degenerated.

Furthermore, the operator $\tilde{U}(k)$ satisfies PHS† in H type, namely Eq.(4.30d) with $\Xi_- = \tau_z \otimes \sigma_0$. Thereby, CS in H type in Eq.(4.30e) with $\Gamma = \tau_y \otimes \sigma_y$ is also satisfied. Accordingly, the operator $\tilde{U}(k)$ is classified in class DIII† in H type, though it is classified in class AII† in U type.

We remark that the symmetry realizations in Eq. (4.30d) assumes that the eigenenergy E appears a pair $\pm E$, thus the particle-hole symmetric point $E_0 = 0$. If the symmetric point E_0 is not zero, Eq. (4.30d) is modified as

$$\Xi_- \left[H(k) - E_0\right]^* \Xi_-^{-1} = -\left[H(-k) - E_0\right]. \tag{6.32}$$

This means that when the operator satisfies Eq. (4.30d), the operator also satisfies Eq. (6.32) only for $\mathrm{Re}\,[E_0] = 0$. In other words, $\mathrm{PHS}^\dagger$ is broken for $\mathrm{Im}\,[E_0] \neq 0$. Accordingly, our quantum walk $\tilde{U}(k)$ belongs in class $\mathrm{AII}^\dagger$ even in H type if the symmetric point is not a pure imaginary number. While this fact may imply that the dual symmetry classification is not important, this is not the case as we explained in Sec. 6.4.

We also note that while we consider symmetry of our quantum walk only in the momentum representation for simplicity, symmetries mentioned above hold even in the time-evolution operator in the real space. Therefore, even if the parameter $\theta(x)$ in Eq. (6.16) and γ in Eq. (6.22) depend on the position, the symmetry class is unchanged.

6.3.4 Experimental implementation

At the end of Sec. 6.3, we simply mention the experimental realization of our quantum walk. In the experiment of photonic quantum walks in nonunitary dynamics, the coin operator, shift operator, and gain-loss operator can be realized by using a half-wave plate, beam displacer, and partially polarizing beam splitter, respectively. To experimentally implement the jump operator in our model, we propose two methods utilizing distinct optical setups, as illustrated in Fig. 6.4. In Fig. 6.4(a), we employ polarizing beam splitters and mirrors to facilitate the jump of photons possessing a specific polarization to the other chain. Here, photons with the $|R\rangle$ internal state traverse the polarizing beam splitter directly, maintaining their original direction. Conversely, photons with the $|L\rangle$ internal state undergo a $\pi/2$ reflection. After two subsequent reflections in the mirrors, they traverse the beam splitter of the alternate chain in a direction parallel to the incident path. In Fig. 6.4(b), a notched rectangle beam displacer is employed. This architecture is expected to be more compact and stable than that in Fig. 6.4(a). Photons with the $|R\rangle$ internal state remain on their original chain, while photons with the $|L\rangle$ internal state undergo displacement. After two refractions, they move to the alternate chain in a direction parallel to the original chain.

6.4 $\mathbb{Z}_2$ point-gap topology of the nonunitary quantum walk

In this section, we study the point-gap topology of our nonunitary quantum walk $\tilde{U}(k)$ in Eq. 6.31. We recall that the operator $\tilde{U}(k)$ belongs to class $\mathrm{DIII}^\dagger$ in H type for the symmetric point

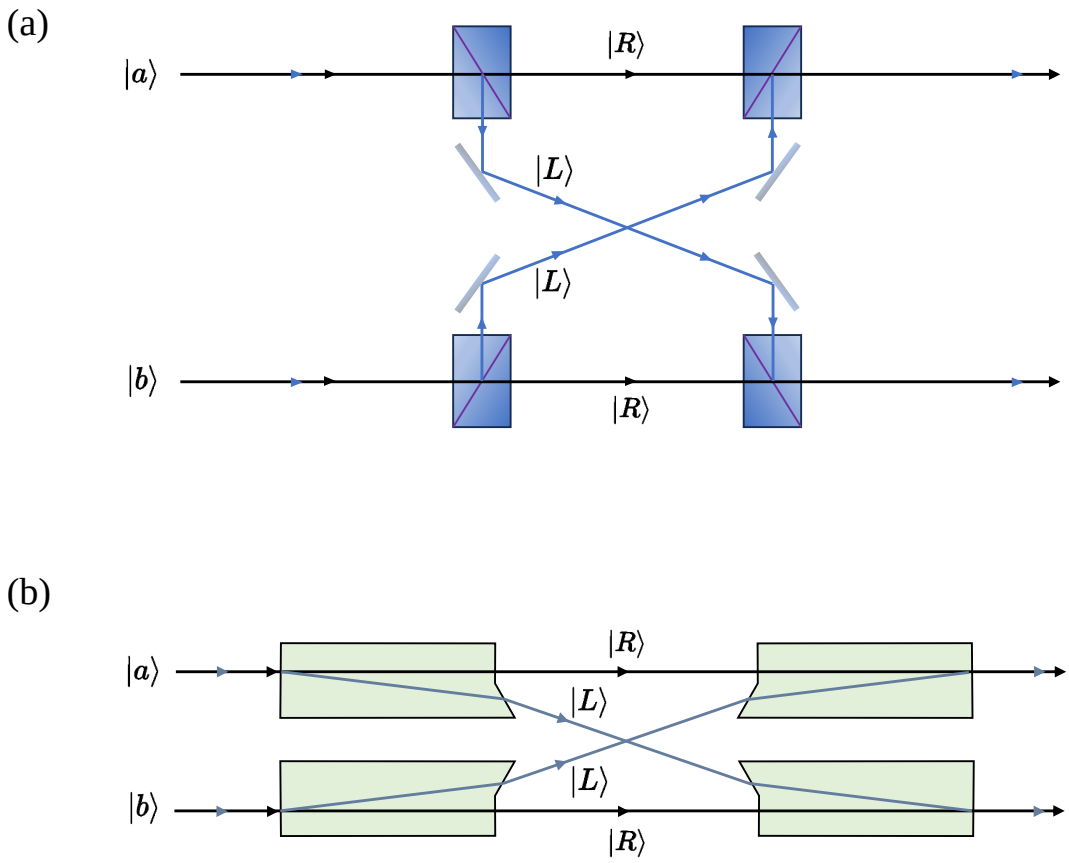

Figure 6.4: The schematic view of the two experimental implementation for the jump operator J_2 using (a) beam splitters and (b) beam displacers. The walker with an internal state of $|L\rangle$ undergoes a jump to the other chain, while the walker with an internal state of $|R\rangle$ remains on the same chain. J_1 can be implemented by rotating the polarization of the photons entering each optical path of the J_2 setup by 90 degrees using a half-wave plate and the polarization of the photons output from the J_2 setup by 90 degrees using a half-wave plate.

$\mathrm{Re}[E_0] = 0$, otherwise it belongs to class $\mathrm{AII}^\dagger$ in H type. On the other hand, the operator $\tilde{U}(k)$ belongs to class $\mathrm{AII}^\dagger$ in U type for any symmetric point.

6.4.1 $\mathbb{Z}_2$ point-gap topology under PBC and RBC

The eigenvalues λ of $\widetilde{U}(k)$ are shown by red curves in Fig. 6.5 for two specific values of parameters. Figure 6.5(a) clearly shows that the point gaps open in finite regions of the symmetric point E_0, while the point gaps close by slightly changing the value of θ_2 from $\pi/5$ to $\pi/6$ as shown in Figure 6.5(b). However, due to the double degeneracy of the eigenvalue, the energy-winding number for class $\mathrm{DIII}^\dagger$ is always trivial. However, an additional topological invariant, known as

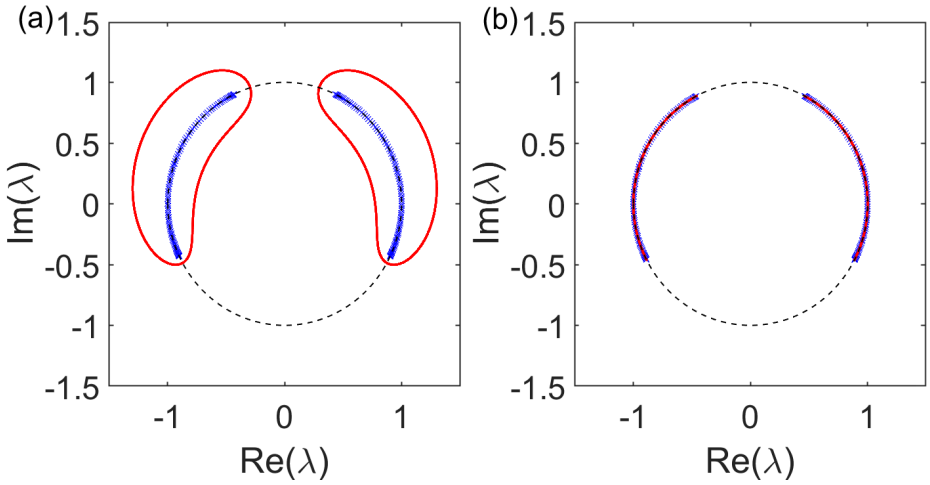

Figure 6.5: Eigenvalue spectra of the time evolution operator U under PBC (red curves) and RBC (blue dots) in the case of $\gamma = 0.5$, $\theta_1 = 3\pi/10$ and $\theta_3 = \pi/4$. (a) $\theta_2 = \pi/5$, (b) $\theta_2 = \pi/6$. The black dashed line represents the unit circle.

$\mathbb{Z}_2$ topological invariant, defined in Ref. [43] by

$$(-1)^{\nu(\lambda)} = \mathrm{sgn}\left\{\frac{\mathrm{Pf}\left[\left(\widetilde{U}(\pi) - E_0\right)\mathcal{T}\right]}{\mathrm{Pf}\left[\left(\widetilde{U}(0) - E_0\right)\mathcal{T}\right]}\right\}, \tag{6.33}$$

can be topologically nontrivial for $\mathrm{Re}\,[E_0] = 0$ in class DIII† in H type. Here, $\nu \in \{0, 1\}$ represents $\mathbb{Z}_2$ topological invariant, with $\nu = 0$ indicating a topologically trivial phase. We confirmed that $\nu = 1$ when E_0 locates in the closed curves in Fig. 6.5(a). Here, we emphasize that we use the nonunitary time-evolution operator $\tilde{U}(k)$ instead of the effective Hamiltonian in Eq. (6.33) to calculate the $\mathbb{Z}_2$ topological invariant while Eq. (6.33) is defined for non-Hermitian Hamiltonians. Therefore, the fact that the regarding the time-evolution operator as the non-Hermitian Hamiltonian, which is crucial for the dual symmetry classification, is essential to study the topological phase.

However, as we mentioned, our quantum walk belongs to class AII† in H type for general value of E_0. In this case, $\mathbb{Z}_2$ topological invariant at a symmetric point E_0 is defined by

$$(-1)^{\nu(\lambda)} = \mathrm{sgn}\left\{\frac{\mathrm{Pf}\left[\left(\widetilde{U}(\pi) - E_0\right)\mathcal{T}\right]}{\mathrm{Pf}\left[\left(\widetilde{U}(0) - E_0\right)\mathcal{T}\right]} \times \exp\left[-\frac{1}{2}\int_{k=0}^{k=\pi} dk\partial_k \log\det\left[\left(\widetilde{U}(k) - E_0\right)\mathcal{T}\right]\right]\right\}, \tag{6.34}$$

in Ref. [43] Again we remark that we use $\tilde{U}(k)$, not the Hamiltonian, to calculate the $\mathbb{Z}_2$ topological invariant. Since Eq. (6.34) is defined for the operator in H type, if $\mathbb{Z}_2$ invariant can be

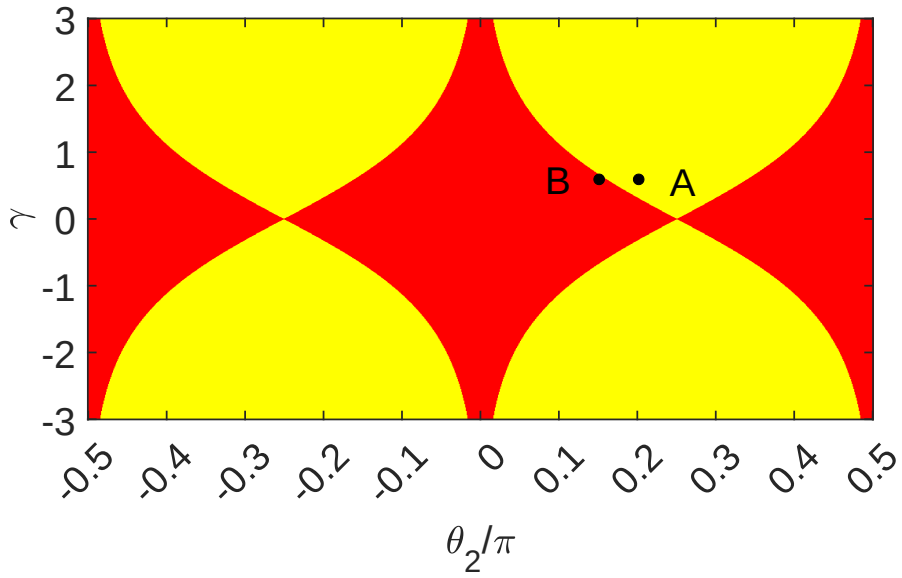

Figure 6.6: The phase diagram of $\mathbb{Z}_2$ topological invariant in the parameter space (θ_2, γ), with $\theta_1 = \frac{3}{10}\pi$ and $\theta_3 = \frac{\pi}{4}$. In the region depicted by filled yellow, $\nu(\lambda) = 1$ for some values of λ, while in the region shown by filled red, $\nu(\lambda) \equiv 0$ for any value of λ.

correctly calculated in Eq. (6.34), this clarifies the correctness of our proposal on the dual symmetry classification.

Figure 6.6 illustrates the $\mathbb{Z}_2$ topological invariant of $\widetilde{U}(k)$ as a function of the parameters θ_2 and γ and the symmetric point E_0 by numerically solving Eq.(6.34). The yellow region represents the presence of at least one point $E_0 \in \mathbb{C}$ where $\nu(\lambda) = 1$, while the blue region indicates that any points on the complex plane is topologically trivial. The A and B in Fig. 6.6 indicates the parameters used in Fig. 6.5 (a) and (b), respectively.

Here, we check the bulk-edge correspondence for $\mathbb{Z}_2$ point-gap topology of our quantum walk. As explained, in case of Fig. 6.5 (a), the point gap opens in which $\mathbb{Z}_2$ topological invariant is nontrivial, while there are no point gap in Fig. 6.5 (b). To calculate the spectra and eigenstates of the operator U with RBC in the real space representation, we apply for the the generalized Brillouin zone (GBZ) [52, 148–150] as shown in Fig. 7.4 (a) and (b). Figure 6.5 (a) shows that the spectrum for the system with RBC (RBC spectrum, in short) depicted by blue dots appears as arcs in the point gap. Furthermore, the eigenstates are localized at right and left boundaries, confirming $\mathbb{Z}_2$ NHSE. More specifically, as shown in Fig. 7.4 (a) and (b), GBZ inside of Brillouin zone (BZ) correspond to eigenmodes localized at the left boundary, while those outside of BZ represent right-boundary-localized eigenmodes [55]. On the other hand, in case of Fig. 6.5(b)

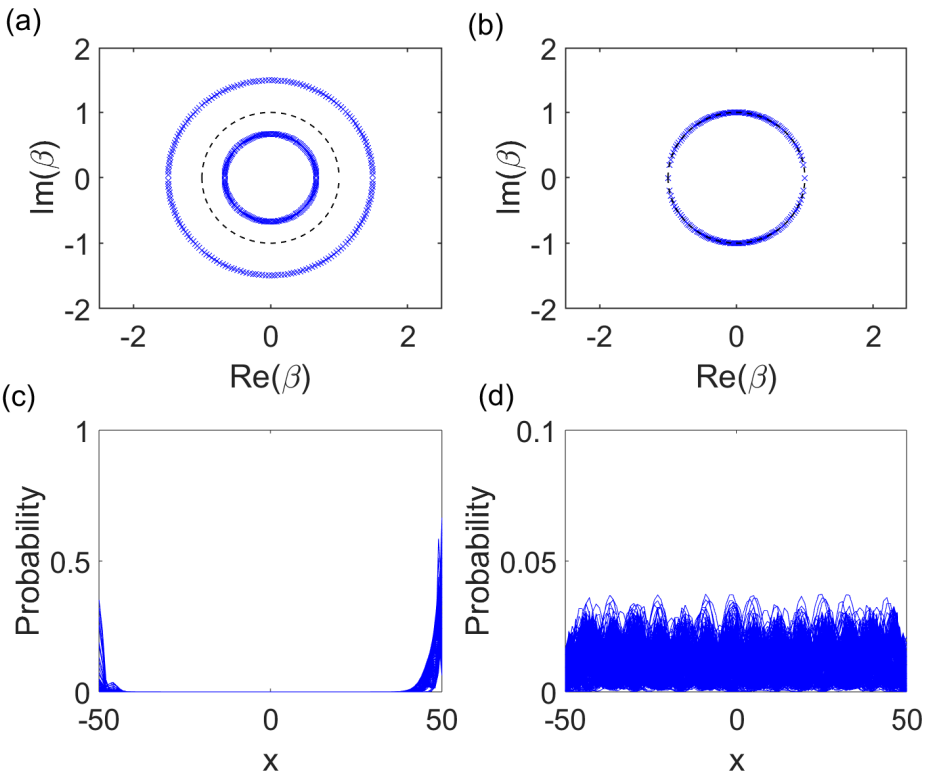

Figure 6.7: GBZ and BZ of the time evolution operator U under RBC in the case of $\gamma = 0.5$, $\theta_1 = 3\pi/10$ and $\theta_3 = \pi/4$ for (a) $\theta_2 = \pi/5$, (b) $\theta_2 = \pi/6$. GBZ is depicted by blue crosses while BZ forming a unit circle on the complex plane is represented by dashed line. (c,d) The probability distributions of the corresponding eigenvectors of U for (c) $\theta_2 = \pi/2$ and (b) $\theta_2 = \pi/6$.

with trivial topology, the RBC spectrum almost overlaps with the PBC spectrum. Moreover, the GBZ coincides with the BZ as shown in Fig. 7.4(b), resulting in the disappearance of NHSE, and the eigenmodes are not localized near the boundaries as shown in Fig. 7.4 (d). These numerical results verify that the quantum walk in Eq. (6.31) exhibits $\mathbb{Z}_2$ point-gap topology in H type and satisfies the bulk-edge correspondence for $\mathbb{Z}_2$ point-gap topology.

Finally, we analyze the dynamical evolution of this quantum walk. We consider a walker initially positioned at the origin and investigate its descrete evolution under the presence and absence of the skin effect, respectively. In Fig. 6.8, we present the probability distribution of the walker in real space after each step. It can be observed that in systems where the time evolution operator exhibits a point gap, the walker becomes localized near the left and right boundaries after a certain number of steps. In contrast, in systems where the time evolution operator is topologically trivial, the walker is not confined to the boundaries, indicating the absence of the

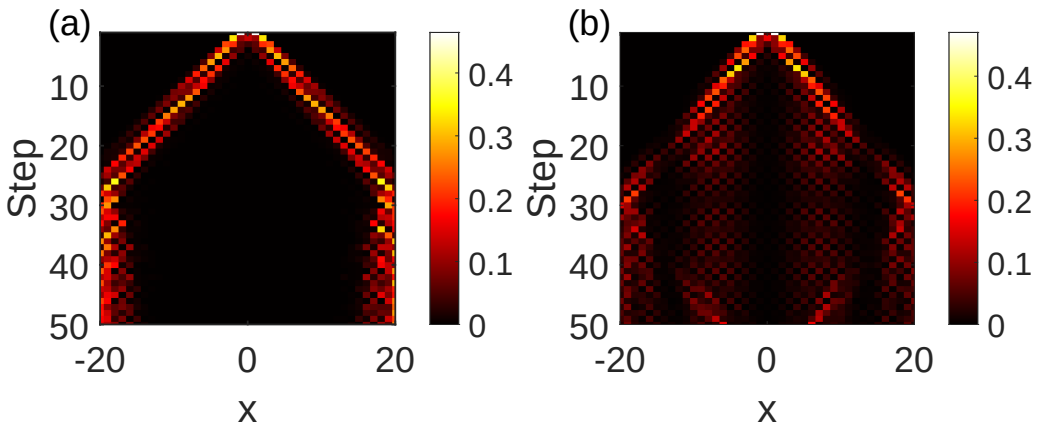

Figure 6.8: Time evolution of the probability distribution of the quantum walk in the case of $\gamma = 0.5$, $\theta_1 = 3\pi/10$ and $\theta_3 = \pi/4$. (a) $\theta_2 = \pi/5$, (b) $\theta_2 = \pi/6$. The initial state of the walker is given by $|\psi_0\rangle = |0\rangle \otimes [|a\rangle \otimes (|L\rangle + i|R\rangle) + |b\rangle \otimes (|L\rangle - i|R\rangle)]/2$.

skin effect.

6.4.2 $\mathbb{Z}_2$ point-gap topology in junction systems

Recently, the bulk-edge correspondence for $\mathbb{Z}$ point-gap topology has been generalized to junction systems where the topological number varies at interfaces[61]. It states that the spectrum for the junction systems in a ring geometry appears in a region where the difference in the point-gap topological numbers for two subsystems is nonzero and the corresponding eigenstates are localized at the interfaces.

In this subsection, we study the bulk-edge correspondence for $\mathbb{Z}_2$ point gap topology in junction systems by using the nonunitary quantum walk with $\mathbb{Z}_2$ point-gap topology. We explore a system with a ring geometry comprising two subsystems connected; subsystem A in the region $1 \leq x \leq l$ and subsystem B in the region $l + 1 \leq x \leq 2l$, where both subsystems possess distinct parameters of the nonunitary quantum walk with $\mathbb{Z}_2$ point-gap topology. Therefore, there are two interfaces near $x = 1$ and l.

Figure. 6.9 (a) shows PBC spectra for the individual subsystems, σ^A_{PBC} and σ^B_{PBC}, under different parameter pairs (θ^A_1, θ^B_1), as well as the eigenvalue spectrum of the junction system, $\sigma^{\mathrm{junc}}_{\mathrm{PBC}}$. Note that the $\mathbb{Z}_2$ topological number for each subsystem ν is one in the closed curves of σ^A_{PBC} or σ^B_{PBC}. Thereby, the difference in $\mathbb{Z}_2$ topological topological number is zero in a region with no point gap and a region where σ^A_{PBC} and σ^B_{PBC} are overlapped. We observed that $\sigma^{\mathrm{junc}}_{\mathrm{PBC}}$ appears as

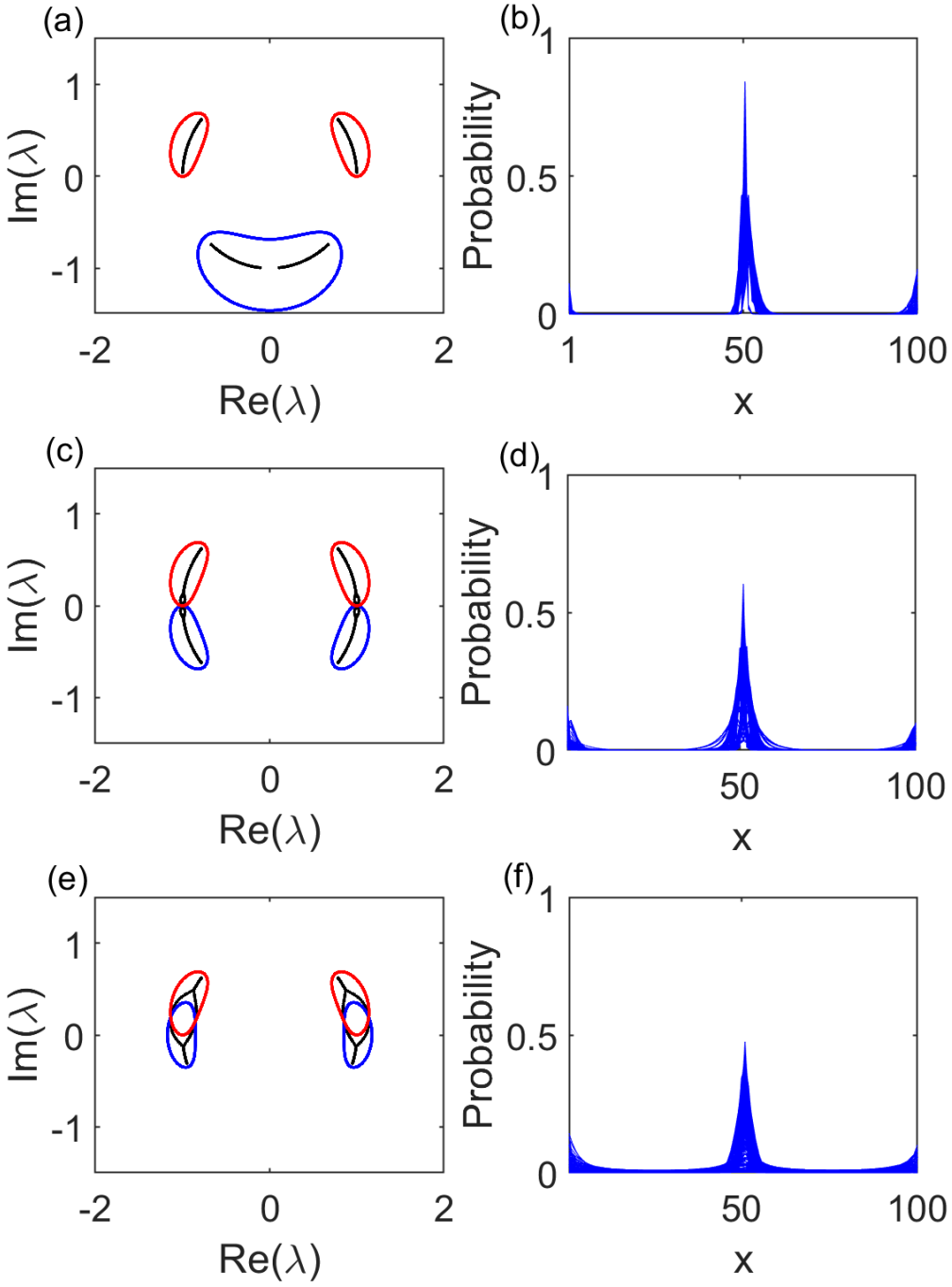

Figure 6.9: (a,c,e) Eigenvalue spectra and (b,d,f) probability distributions of all eigenvectors of the time-evolution operator in the junction system composed of two nontrivial subsystems A and B with the parameters $l = 50$, $\gamma_A = \gamma_B = 0.5$, $\theta_{1,B} = 3\pi/10$, $\theta_{2A} = \theta_{2B} = \pi/4$ and $\theta_{3A} = \theta_{3B} = 2\pi/5$, (a,b) $\theta_{1A} = \pi/10$, (c,d) $\theta_{1A} = \pi/5$, (e,f) $\theta_{1A} = \pi/4$. The left figures (a,c,e) show the eigenvalue spectrum of subsystem A (blue curve), subsystem B (red curve) and junction system with PBC (black curve), while the right figures (b,d,f) show the corresponding distribution of all eigenstates.

arcs in the region where the difference in $\mathbb{Z}_2$ topological topological number is nonzero as shown by black curves in Fig. 6.9 (a). Furthermore, the eigenstates localized near the interfaces of the two subsystems, called the non-Hermitian proximity effects[61], as shown in Fig. 6.9(b). We note that although there is always a tendency for the eigenstates of the time evolution operator to be localized near the boundaries of the two subsystems, this localization strength gradually weakens as σ^A_{PBC} and σ^B_{PBC} get closer. When σ^A_{PBC} and σ^B_{PBC} are sufficiently far apart, the eigenstates are tightly confined near the interface [see Fig.6.9(a) and (b)]. However, as the distance between the two spectra decreases and even when they intersect, the eigenstates may have a non-negligible probability of appearing even at the center of the subsystems, although they still exhibit a tendency to move towards the interface [see Fig.6.9(e) and (f)]. These observations establishes the bulk-edge correspondence for $\mathbb{Z}_2$ point-gap topology in junction systems in the same fashion with $\mathbb{Z}$ point-gap topology as clarified in Ref. [61].

Figure 6.10 illustrates the time evolution of the walker in the junction system. In Figs. 6.10(a), (c),(e), and (g), the walker is initially located on subsystem A, while in Figs. 6.10(b), (d),(f), and (h), the walker's initial state is on subsystem B. We observe that when σ^A_{PBC} and σ^B_{PBC} are sufficiently far apart, the walker is strongly stucked near the interface. However, in cases where σ^A_{PBC} and σ^B_{PBC} overlap each other, the confinement near the interface of the subsystems is not as strong as in the previous cases, as indicated by Figs. 6.10(g,h).

6.4.3 $\mathbb{Z}_2$ point-gap topology in stacked systems

A hallmark of $\mathbb{Z}_2$ topology manifests in the gap-closing phenomenon emerging when stacking two identical topologically nontrivial systems. To explore this characteristic in non-Hermitian Floquet systems, we construct a bilayer system consisting of two identical quantum walk subsystems. Since our quantum walk exhibits nontrivial $\mathbb{Z}_2$ point-gap topology under the U-type symmetry classification, we mathematically construct the stacked system through direct sum of time-evolution operators of the subsystems in the stacking space. By introducing a constant interlayer coupling strength Δ that preserves original symmetries of the system, the time-evolution

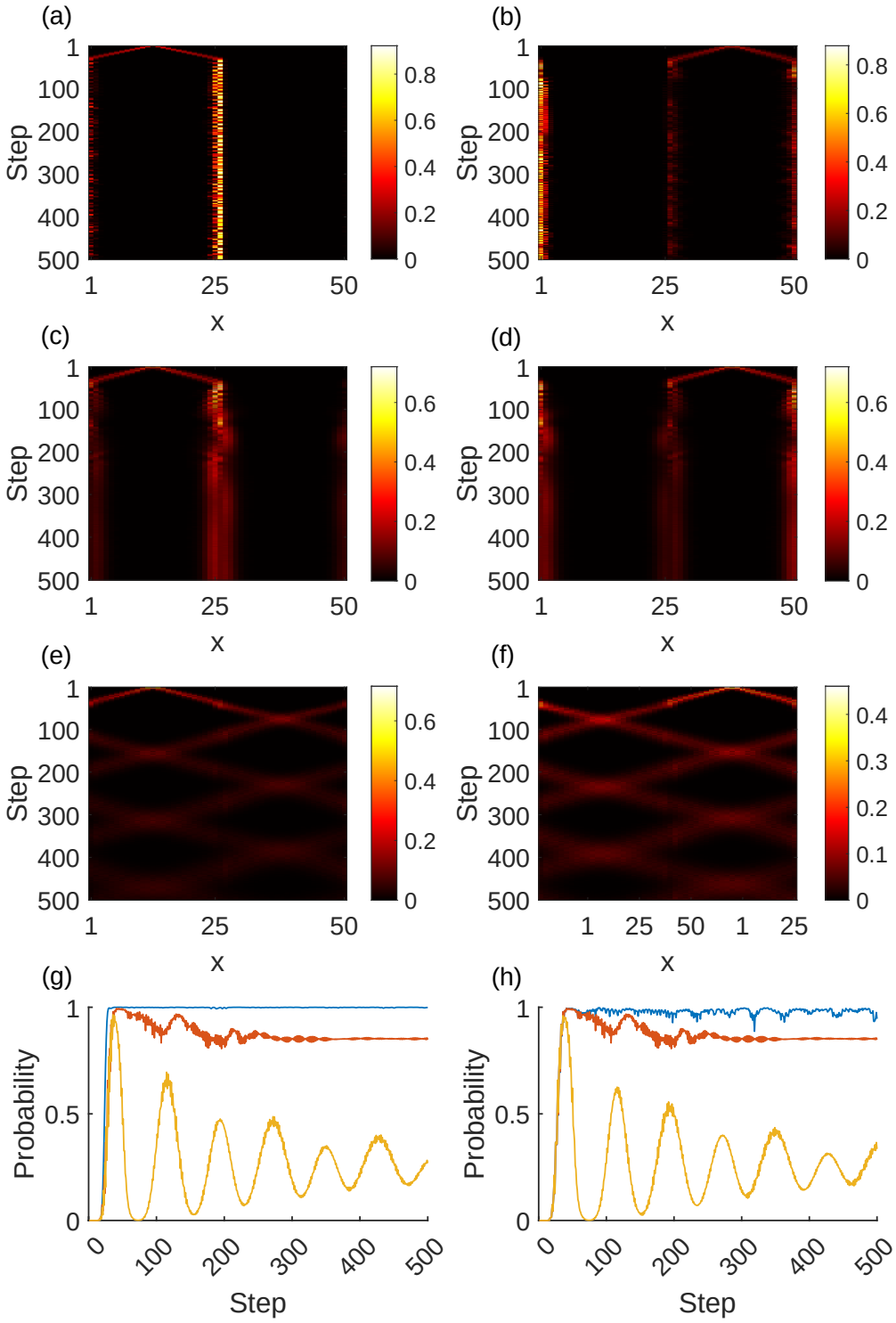

Figure 6.10: (a-f) Time evolution of the probability distribution in a junction system with PBC with the parameters $l = 25$, $\gamma_A = \gamma_B = 0.5$, $\theta_{1,B} = 3\pi/10$, $\theta_{2A} = \theta_{2B} = \pi/4$ and $\theta_{3A} = \theta_{3B} = 2\pi/5$, (a,b) $\theta_{1A} = \pi/10$, (c,d) $\theta_{1A} = \pi/5$, (e,f) $\theta_{1A} = \pi/4$. (g,h) The time dependence of the probability of the walker near the boundaries of two subsystems. The initinal state of the walker is given by (a,c,e,g) $|\psi_0\rangle = |x_{0,A}\rangle \otimes [|a\rangle \otimes (|L\rangle + i|R\rangle) + |b\rangle \otimes (|L\rangle - i|R\rangle)]/2$ and (b,d,f,h) $|\psi_0\rangle = |x_{0,B}\rangle \otimes [|a\rangle \otimes (|L\rangle + i|R\rangle) + |b\rangle \otimes (|L\rangle - i|R\rangle)]/2$, with $x_{0,A} = (l+1)/2$ and $x_{0,B} = l+(l+1)/2$.

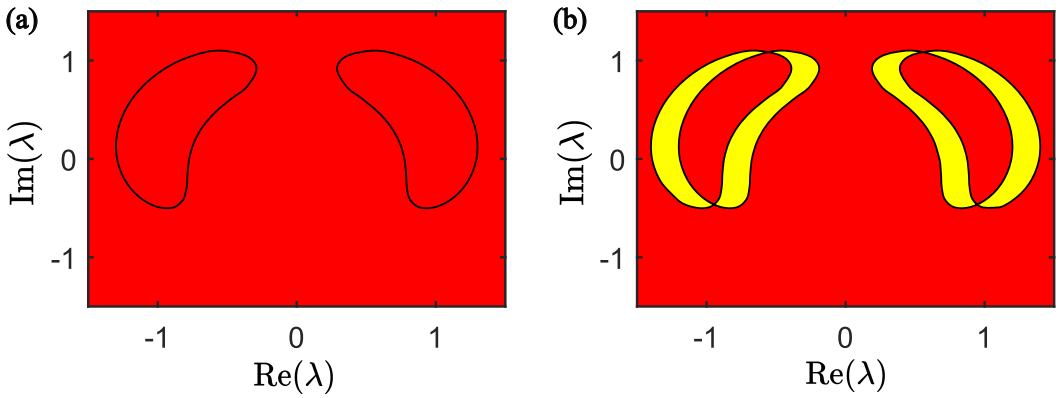

Figure 6.11: Distribution of the $\mathbb{Z}_2$ topological index in the stacked quantum walk system with parameters $\theta_1 = 3\pi/10$, $\theta_2 = \pi/5$, and $\theta_3 = \pi/4$. (a) Decoupled subsystem configuration ($\Delta = 0$). (b) Strong stacking strength with $\Delta = 0.1$. Regions shaded in yellow and red correspond to $\nu(\lambda) = 1$ and $\nu(\lambda) = 0$, respectively. Black curves represent the eigenvalue spectrum of U_s where the $\mathbb{Z}_2$ index becomes undefined.

operator of the stacked system assumes the block matrix form:

$$U_s(k) = \begin{pmatrix} U(k) & \Delta \\ \Delta & U(k) \end{pmatrix}. \tag{6.35}$$

The eigenvalue spectrum of $U_s(k)$ and the distribution of the $\mathbb{Z}_2$ topological index are shown in Fig. 6.11. In the case of $\Delta = 0$, where the two subsystems are decoupled, the $\mathbb{Z}_2$ point-gap topology is trivial for any reference point in the complex plane [see Fig. 6.11(a)]. This is expected due to the intrinsic $\mathbb{Z}_2$ nature. However, under strong stacking interactions, the spectrum begins to split, and nontrivial $\mathbb{Z}_2$ regions emerge [see Fig. 6.11(b)]. According to the definition in Eq. (6.34), the yellow regions, which are enclosed by the spectrum only once, exhibit nontrivial $\mathbb{Z}_2$ topology, whereas the red regions, surrounded by the spectrum twice, display trivial $\mathbb{Z}_2$ topology.

The above conclusion is particularly intriguing as it deviates from the conventional understanding of $\mathbb{Z}_2$ topology, which is generally considered highly fragile against stacking. In fact, the emergence of the nontrivial topological phases in such system arises from the splitting of a fourfold degeneracy into a twofold degeneracy, driven by non-Hermitian level repulsion between Kramers pairs. In Chapter 7, we will explore the robustness of the $\mathbb{Z}_2$ topological phase in stacked systems in detail and map this problem, through Hermitization, to the stability of Majorana zero modes in Hermitian systems.

6.5 Summary and discussion

In summary, in this chapter, by using H-type dual symmetry classification in Chapter 5 and regarding the time-evolution operator as the non-Hermitian Hamiltonian, we have successfully constructed a nonunitary quantum walk with spinful $\mathrm{TRS}^{\dagger}$. Furthermore, we have shown that this nonunitary quantum walk can obtain nontrivial $\mathbb{Z}_2$ point-gap topology again regarding the time-evolution operator as the non-Hermitian Hamiltonian. The eigenvalue spectrum of the system strongly depends on the system's boundary conditions when the time evolution operator is $\mathbb{Z}_2$ topologically nontrivial. Under RBC, the eigenstates of the time evolution operator exhibit localization near the boundaries, indicating the presence of the skin effect. In contrast to the traditional Hatano-Nelson model, in such a quantum walk, we can control the opening and closing of the point gap by adjusting the parameters of the coin operators or the gain-loss operator.

Moreover, we studied quantum walks in junction system composed of two $\mathbb{Z}_2$ nontrivial quantum walks. When the distance between the PBC spectra of the two topologically nontrivial subsystems in the junction system is sufficiently large, the PBC spectrum of the junction system can be effectively treated as an RBC spectrum, which is also a novel approach to achieve RBC in arbitrary quantum walks. In this scenario, all eigenstates become localized near the boundaries of the two subsystems, resulting in the non-Hermitian proximity effects. However, as the distance between the two PBC spectra decreases, the confinement ability of the boundaries on the eigenstates weakens. The same phenomenon also occurs with the confinement ability on the walker.

In this chapter, we have defined the skin effect in nonunitary quantum walk systems as the localization of eigenstates of the time evolution operator near the boundaries of the system. We have noticed that in quantum walk systems with skin effect, the walker becomes localized near the boundaries of the system after a sufficiently long time. However, especially for the junction system, the state of the walker's evolution over time is not well-defined. In particular, when the eigenvalue spectrum of the PBC junction system has a non-zero area, the choice of initial state can affect the boundaries to which the walker becomes confined. Studying the time evolution of nonunitary quantum walks is an interesting work and holds significant importance for investigating the time-dependent topological properties of non-Hermitian systems.

Finally, we discuss a possible application of the dual symmetry classification proposed in the

current work to unitary time-evolution operators. In principle, the dual symmetry classification can also be applied to unitary time-evolution systems. Applying the H-type classification, we can identify line and point gaps for various unitary time-evolution operators, where nontrivial topological phases may arise. However, these unitary time-evolution operators do not show phenomena peculiar to non-Hermitian physics, such as point-gap topology and skin effects, as long as they keep unitarity, for the following reasons. A unitary time-evolution operator U, related to the effective Hermitian H_{eff} by Eq. (5.1), can commute with H_{eff}, leading to U and H_{eff} having simultaneous eigenstates. Therefore, since all the eigenstates are those of the Hermitian Hamiltonian, phenomena unique to non-Hermitian systems are not anticipated. However, applying the dual symmetry classification for unitary time-evolution operators may give an opportunity to better understand of the topological properties in Hermitian systems. We leave it as an open problem.

Chapter 7

Robust $\mathbb{Z}_2$ Topological Phases in Stacked Systems

7.1 Introduction

Quantum spin Hall (QSH) insulators have attracted significant interest and spurred extensive research into the field of topological insulators over the past two decades [8, 9, 13, 14, 67–71, 171–175]. The concept of a QSH insulator was first proposed by Kane and Mele in 2005 [8, 9]. They showed that a nontrivial topological phase appears in a system with Kramers pairs due to time-reversal symmetry (TRS) by considering the coupling of two Haldane models [6] with opposite effective magnetic fields. They showed that the topological phase of such a two-dimensional (2D) system hosts helical edge states of Kramers pairs, where electrons with opposite spins propagate in opposite directions without back scattering. They also proposed that the topology of such a system can be defined by a $\mathbb{Z}_2$ topological invariant. Because of the Kramers pairs, TRS in the QSH system is called spinful TRS. Soon after that, following a more realistic proposal [171], the QSH effect was first experimentally observed in HgTe/CdTe quantum wells [13]. The $\mathbb{Z}_2$ topological phase has also been extended to the three-dimensional systems with Kramers pair due to TRS and experimentally observed[14–17]. These theoretical and experimental progress have highly stimulated the study of the topological phase of matter. Beyond the well-known 2D and 3D topological insulators, other topological phases exhibiting $\mathbb{Z}_2$ topology exist, which are classified by different symmetry classes. In one-dimensional (1D) systems, $\mathbb{Z}_2$ topology can also be observed in classes DIII [176–178] and D [179–181]. Class DIII exhibits

spinful TRS, examples of which include 1D superconductors with Majorana edge states. Class D systems possess particle-hole symmetry (PHS) but lack TRS, such as 1D superconductors in the presence of a magnetic field.

In recent years, research on non-Hermitian systems has gained significant attention due to its potential for novel physical phenomena. $\mathbb{Z}_2$ topology can also be defined in non-Hermitian systems with point gaps, as discussed in the preceding chapters. For 1D systems, $\mathbb{Z}_2$ point-gap topology appears in systems with spinful TRS† (AII†, DIII†, etc) due to the emergence of the Kramers degeneracy [43, 62, 182–184]. A simple example is the coupled Hatano-Nelson model with spinful TRS†, introduced in Sec. 4.4, where all eigenstates are localized at both boundaries of the system, referred to as the $\mathbb{Z}_2$ NHSE [54].

By stacking multiple 1D strips or layering 2D sheets of topological materials, a hetero structure with unique and potentially advantageous properties can be realized, known as a stacked system. These systems are of significant interest for both fundamental research and practical applications, such as quantum computing [72, 185], due to the novel electronic, magnetic, and optical behaviors that can arise from interactions between the layers [186–189]. It is generally believed that when an even number of layers where each layer has a nontrivial $\mathbb{Z}_2$ topological phase, such as quantum spin Hall insulators, are stacked, the $\mathbb{Z}_2$ topological phase becomes unstable due to the $\mathbb{Z}_2$ nature. However, several researchers have shown that $\mathbb{Z}_2$ topology exhibits robustness against stacking in Hermitian systems in certain parameter regions[180, 190, 191]. Despite these findings, the reason has not yet been seriously discussed and there has been no systematic research identifying the underlying causes of this robustness.

In this Chapter, we provide a systematic understanding of the robust $\mathbb{Z}_2$ topological phase in a Hermitian system with chiral symmetry against stacking. We clarify that the robustness generally originates from level repulsion in the corresponding non-Hermitian system derived from Hermitization[192]. We demonstrate this by treating a class DIII superconductor in 1D with $\mathbb{Z}_2$ topology and the corresponding non-Hermitian 1D system in class AII† with $\mathbb{Z}_2$ point-gap topology as an example. For the latter system, in the case of stacking two 1D chains, the four-fold degeneracy of the spectrum breaks down to two-fold degeneracy due to the level repulsion between two Kramers pairs as expected. Remarkably, $\mathbb{Z}_2$ point-gap topology at the energy E in point gaps emerged as the level repulsion remains nontrivial. Moreover, through Hermitiza-

tion, the energy E of the non-Hermitian system takes the role of the chemical potential μ of the Hamiltonian for the DIII superconductors. Due to this correspondence, the energy region for the nontrivial $\mathbb{Z}_2$ point-gap topology coincides with the range of μ where the $\mathbb{Z}_2$ topological phase of the DIII stacked superconductor is nontrivial and zero-energy states appear. Our result provides a systematic understanding of robust $\mathbb{Z}_2$ topology in Hermitian systems with chiral symmetry, as the level repulsion in the corresponding non-Hermitian systems. We note that the stacking 2D $\mathbb{Z}_2$ topological insulators were studied from the view point of the robustness of 2D surface states on a 3D weak topological insulator[172, 193–195]. However, the weak $\mathbb{Z}_2$ topological invariant for the 3D system was studied in these works and not the (strong) $\mathbb{Z}_2$ topological invariant for the 2D system.

This Chapter is organized as follows. In Sec. 7.2, we provide our main idea that non-Hermitian level repulsion can be considered the origin of robust $\mathbb{Z}_2$ topological phases in stacked Hermitian systems via a Hermitization process. In Sec. 7.3.1, we define a 1D DIII superconductor and show that it can be transformed into a Hermitized version of a coupled Hatano-Nelson model in class AII†. We demonstrate that the emergence of zero-energy states in the Hermitian system can be predicted by relating the energy point E in the non-Hermitian system to the chemical potential μ in the Hermitian system. In Sec. 7.3.2, we investigate the robustness of the $\mathbb{Z}_2$ point-gap topology against the stacking of coupled Hatano-Nelson models. We find that this robustness results from non-Hermitian level repulsion. Additionally, we use three-chain and four-chain stacked system as examples to demonstrate that the regions of $\mathbb{Z}_2$ trivial and nontrivial point-gap topology on the complex plane alternate along the real axis in multi-chain stacked systems. In Sec. 7.3.3, we examine the stacked DIII superconductor and confirm its robustness using the perspective introduced in Sec. 7.3.1.

7.2 Origin of robust $\mathbb{Z}_2$ topology in stacked systems

First, we explain our main idea of why the robustness of $\mathbb{Z}_2$ topological phases in Hermitian systems can be related to non-Hermitian systems. To establish connections between Hermitian and non-Hermitian systems, the Hermitization procedure of a non-Hermitian Hamiltonian is crucial. For any non-Hermitian $\mathcal{H}$, it can be transformed into a Hermitian Hamiltonian H in the

doubled Hilbert space through Hermitization[192] as follows:

$$H = \begin{pmatrix} 0 & \mathcal{H} - E_p \\ \mathcal{H}^\dagger - E_p^* & 0 \end{pmatrix}, \tag{7.1}$$

where E_p represents a reference point on the complex energy plane of $\mathcal{H}$, while it becomes a system parameter for H. This relation inevitably introduces chiral symmetry for the Hermitian Hamiltonian H, characterized by $\Gamma H \Gamma^{-1} = -H$ with $\Gamma = \tau_z$, where the Pauli matrices $\tau_{x,y,z}$ act on the doubled space. Under periodic boundary conditions (PBC), the presence of a $\mathbb{Z}$ (or $\mathbb{Z}_2$) point gap in the non-Hermitian Hamiltonian $\mathcal{H}$ implies that a corresponding real energy gap will open in the Hermitian Hamiltonian H, which induces edge states, and vice versa [43, 54**?**].

We begin with a non-Hermitian Hamiltonian $\mathcal{H}(k)$ in class AII† that exhibits nontrivial $\mathbb{Z}_2$ point-gap topology. The Hamiltonian $\mathcal{H}$ exhibits spinful TRS†, given by

$$\mathcal{T}\mathcal{H}(k)^T\mathcal{T}^{-1} = \mathcal{H}(-k), \quad \mathcal{T} = \sigma_y, \tag{7.2}$$

where the Pauli matrices $\sigma_{x,y,z}$ and a 2×2 matrix $\sigma_0 = \mathrm{diag}\{1, 1\}$ act on the spin space. The condition $\mathcal{T}\mathcal{T}^* = -1$ leads to the important observation that for any eigenenergy E, there must be at least double degeneracy, with the eigenstates $|\psi\rangle$ and $\mathcal{T}^T|\psi\rangle^*$, referred to as Kramers pairs. If a non-Hermitian Hamiltonian only satisfies Eq. (7.2), the system belongs to class AII†. The topological invariant of such a system can be defined by a $\mathbb{Z}_2$ invariant $\nu \in \{0, 1\}$, while $\mathcal{H}(k)$ exhibits nontrivial $\mathbb{Z}_2$ point-gap topology at the reference point E_p when $\nu(E_p) = 1$.

The stacked system of $\mathcal{H}(k)$ is written as

$$\mathcal{H}_\mathrm{s}(k) = \begin{pmatrix} \mathcal{H}(k) & \delta_0\sigma_0 + i\boldsymbol{\delta}\cdot\boldsymbol{\sigma} \\ \delta_0\sigma_0 - i\boldsymbol{\delta}\cdot\boldsymbol{\sigma} & \mathcal{H}(k) \end{pmatrix}, \tag{7.3}$$

where δ_0 and $\boldsymbol{\delta} = (\delta_x, \delta_y, \delta_z)$ denotes the k-independent stacking strengths. The stacked Hamiltonian preserves spinful TRS† with the symmetry operator $\mathcal{T} = \eta_0 \otimes \sigma_y$, where the 2×2 matrix $\eta_0 = \mathrm{diag}\{1, 1\}$ acts on the stacked space. One might naturally assume that $\mathcal{H}_\mathrm{s}$ should be $\mathbb{Z}_2$ trivial even if each $\mathcal{H}(k)$ is $\mathbb{Z}_2$ nontrivial because of the $\mathbb{Z}_2$ nature. However, the stacking term introduces the level repulsion which makes the four-fold degeneracy of the spectrum the double degeneracy, as illustrated in Fig. 7.1. In tthe case of Fig. 7.1 (a) without couplings, since the system consists of two independent layers with nontrivial $\mathbb{Z}_2$ invariant, the $\mathbb{Z}_2$ invariant remains

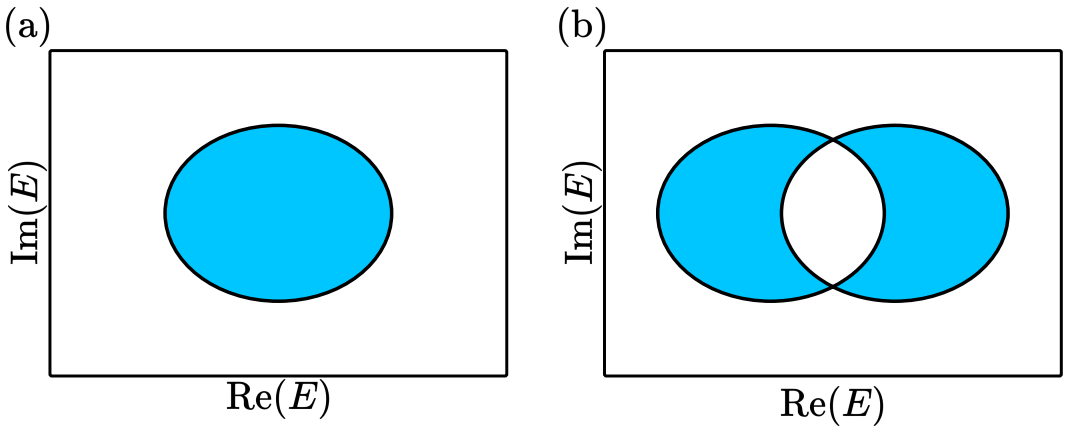

Figure 7.1: Schematic views of the energy spectra of a stacked non-Hermitian Hamiltonian $\mathcal{H}_s(k)$ (a) without and (b) with coupling terms. The black solid curve represents the four-fold and two fold degenerated energy spectrum in (a) and (b) respectively. The blue regions indicate emergence of nontrivial $\mathbb{Z}_2$ point-gap topology.

nontrivial. In the case of Fig. 7.1 (b) with finite couplings, the four-fold degeneracy is down to two-fold degeneracy due to level repulsion. Since the energy spectrum winds around a point in the middle white region twice, the $\mathbb{Z}_2$ invariant is trivial. On the other hand, since the energy spectrum winds around a point in the blue regions once, the $\mathbb{Z}_2$ invariant is nontrivial. Moreover, the separation distance of the energy spectrum can increase or decrease depending on the stacking strength, leading to the expansion or contraction of the $\mathbb{Z}_2$ nontrivial region.

By employing the Hermitization transform, we can extend conclusions from non-Hermitian systems to Hermitian systems. Since the $\mathbb{Z}_2$ point-gap topology in a non-Hermitian system is robust against stacking due to level repulsion, the corresponding Hermitian Hamiltonian, with parameter E_p (the complex energy in the $\mathbb{Z}_2$ nontrivial region of the non-Hermitian system), also exhibits such robustness. In the Hermitian case, since E_p is a parameter, we cannot understand the robustness through level repulsion as we do in the non-Hermitian case. This approach offers a clear and visual way to understand the robustness of $\mathbb{Z}_2$ topology from a non-Hermitian perspective.

7.3 Demonstration: 1D DIII Hermitian Hamiltonian and 1D AII† non-Hermitian Hamiltonian

In this section, we demonstrate our idea that the robustness of $\mathbb{Z}_2$ topological phases in Hermitian systems originates from the level repulsion of non-Hermitian systems. To this end, we focus on a 1D topological superconductor in class DIII which possesses chiral symmetry resulting in $\mathbb{Z}_2$ topological phases and Majorana Kramers pairs. We demonstrate that the Majorana zero-energy modes are robust in such a system due to the non-Hermitian level repulsion, as discussed in Sec. 7.2.

7.3.1 Models

To begin with, we consider a 1D topological superconductor in class DIII which possesses $\mathbb{Z}_2$ topological phases. Then, we derive the non-Hermitian Hamiltonian through the Hermitization in Eq. (7.1).

The Hamiltonian in class DIII is formulated using fermionic annihilation and creation operators $c_{i,\sigma}$ and $c^\dagger_{i,\sigma}$, respectively, at a site i with spin $\sigma =\uparrow,\downarrow$ and can be expressed as follows:

$$\begin{aligned} H = \sum_{i\in\mathbb{Z}} \Bigg\{ & \sum_{\sigma=\uparrow,\downarrow} t\left(c^\dagger_{i+1,\sigma}c_{i,\sigma} + \text{H.c.}\right) - \mu c^\dagger_{i,\sigma}c_{i,\sigma} \\ & + \frac{1}{2}\Big[\alpha_R\left(c^\dagger_{i+1,\downarrow}c_{i,\uparrow} - c^\dagger_{i,\downarrow}c_{i+1,\uparrow}\right) \\ & - d_x \sum_{\sigma=\uparrow,\downarrow}\left(c^\dagger_{i,\sigma}c^\dagger_{i+1,\sigma} - c^\dagger_{i+1,\sigma}c^\dagger_{i,\sigma}\right) \\ & + d_z\left(c^\dagger_{i,\uparrow}c^\dagger_{i+1,\downarrow} - c^\dagger_{i+1,\uparrow}c^\dagger_{i,\downarrow}\right) + \text{H.c.}\Big]\Bigg\}. \end{aligned} \tag{7.4}$$

The parameter t and μ represent the hopping amplitude and the chemical potential, respectively. Additionally, α_R and $d_{x/z}$ represent the strengths of the spin-orbit coupling and superconductor pairing, respectively. All these parameters are real.

To study the topological properties, we diagonalize the Hamiltonian to momentum space by

Fourier transform $c_{i,\sigma} = \sum_k \frac{1}{\sqrt{N}} e^{ikx_i} c_{k,\sigma}$, and then we obtain a BdG Hamiltonian written as

$$\begin{aligned} H_{\mathrm{BdG}}(k) &= \Psi^\dagger H(k) \Psi \\ &= \Psi^\dagger \begin{pmatrix} h(k) - \mu\sigma_0 & i\boldsymbol{d}(k)\cdot\boldsymbol{\sigma}\sigma_y \\ -i\boldsymbol{d}^*(k)\cdot\boldsymbol{\sigma}\sigma_y & -h^T(-k) + \mu\sigma_0 \end{pmatrix} \Psi, \end{aligned} \tag{7.5}$$

where

$$\Psi = \left(c_{k,\uparrow}, c_{k,\downarrow}, c^\dagger_{-k,\uparrow}, c^\dagger_{-k,\downarrow}\right)^T, \tag{7.6}$$

$$h(k) = 2t\cos(k)\sigma_0 + \alpha_R \sin(k)\sigma_y, \tag{7.7}$$

$$\boldsymbol{d}(k) = i\,(d_x, 0, d_z)\sin k. \tag{7.8}$$

Here, $\boldsymbol{\sigma} = (\sigma_x, \sigma_y, \sigma_z)$ and σ_0 act on the spin space. The effective Hamiltonian $H(k)$ can be rewritten as

$$H(k) = (2t\cos k - \mu)\,\tau_z \otimes \sigma_0 + \alpha_R \sin(k)\tau_z \otimes \sigma_y + d_x \sin(k)\tau_y \otimes \sigma_z - d_z \sin(k)\tau_y \otimes \sigma_x, \tag{7.9}$$

where the Pauli matrices $\tau_{x,y,z}$ and τ_0 act on the particle-hole space. The Hamiltonian satisfies the following symmetry relations

$$\text{TRS}: \quad TH^*(k)T^{-1} = H(-k), \quad T = \tau_z \otimes \sigma_y, \tag{7.10}$$

$$\text{PHS}: \quad PH^*(k)P^{-1} = -H(-k), \quad P = \tau_y \otimes \sigma_y, \tag{7.11}$$

$$\text{CS}: \quad \Gamma H(k)\Gamma^{-1} = -H(k), \quad \Gamma = \tau_x \otimes \sigma_0, \tag{7.12}$$

which results in the system belonging to the DIII symmetry class.

Now we derive a non-Hermitian Hamiltonian from the above DIII Hermitian Hamiltonian through an *inverse-Hermitization procedure*. We consider a unitary transformation after which the chiral symmetry operator exhibits a diagonal form $\Gamma = \tau_z \otimes \sigma_0$. The transformed Hamiltonian

is given by

$$H'(k) = e^{-i\frac{\pi}{4}\tau_y\otimes\sigma_0} H(k) e^{i\frac{\pi}{4}\tau_y\otimes\sigma_0}$$
$$= \begin{pmatrix} & \mathcal{H}(k) - \mu \\ \mathcal{H}^\dagger(k) - \mu & \end{pmatrix}, \tag{7.13}$$

where the off-diagonal matrix

$$\mathcal{H}(k) = \begin{pmatrix} 2t\cos k - id_x \sin k & -i(\alpha_R - d_z)\sin k \\ i(\alpha_R + d_z)\sin k & 2t\cos k + id_x \sin k \end{pmatrix}, \tag{7.14}$$

can be regarded as a non-Hermitian Hamiltonian $\mathcal{H}(k)$ of the coupled Hatano-Nelson model [54]. The diagonal elements of $\mathcal{H}(k)$ represent the Hamiltonian of a Hatano-Nelson model without disorder and its time-reversal partner:

$$\mathcal{H}_{\mathrm{HN}}(k) = \left(t - \frac{d_x}{2}\right) e^{ik} + \left(t + \frac{d_x}{2}\right) e^{-ik}, \tag{7.15}$$

$$\mathcal{H}^T_{\mathrm{HN}}(-k) = \left(t - \frac{d_x}{2}\right) e^{-ik} + \left(t + \frac{d_x}{2}\right) e^{ik}, \tag{7.16}$$

where the prefactors $t \pm d_x/2$ represent the asymmetric hopping terms, and the off-diagonal elements denote the symmetry-protected couplings. We observe that $\mathcal{H}(k)$ exhibits spinful TRS†, following Eq. (7.2), with $\mathcal{T} = \sigma_y$. As a result, the energy spectrum is always double degenerate. Such a system belongs to the AII† symmetry class with $\mathbb{Z}_2$ point-gap topology according to the symmetry classification in non-Hermitian systems[43]. The $\mathbb{Z}_2$ topological invariant ν at reference point E_p on $\mathcal{H}(k)$ is defined by

$$(-1)^{\nu(E_p)} = \mathrm{sgn}\left\{ \frac{\mathrm{Pf}\left[\left(\mathcal{H}(\pi) - E_p\right)\mathcal{T}\right]}{\mathrm{Pf}\left[\left(\mathcal{H}(0) - E_p\right)\mathcal{T}\right]} \times \exp\left[-\frac{1}{2}\int_{k=0}^{k=\pi} dk \frac{\partial \log\det\left[\left(\mathcal{H}(k) - E_p\right)\mathcal{T}\right]}{\partial k} \right] \right\}. \tag{7.17}$$

When $\alpha_R^2 < d_z^2 + d_x^2$, as shown in Fig. 7.2 (a), the spectrum for the system with PBC (PBC spectrum, in short) forms a closed ellipse on the complex plane keeping the double degeneracy, leading to the $\mathbb{Z}_2$ point gaps being open at the point E_p enclosed by the spectrum. Under PBC, when a point-gap opens for non-Hermitian Hamiltonian $\mathcal{H}(k)$, a real energy gap opens for DIII Hermitian Hamiltonian $H(k)$ if the chemical potential $\mu(\in \mathbb{R})$ takes a value within the point gap, as shown by the red line segment in Fig. 7.2(a). In this case, $H'(k)$ [also $H(k)$] has nontrivial $\mathbb{Z}_2$ topology, leading to the emergence of Majorana zero-energy modes under open boundary

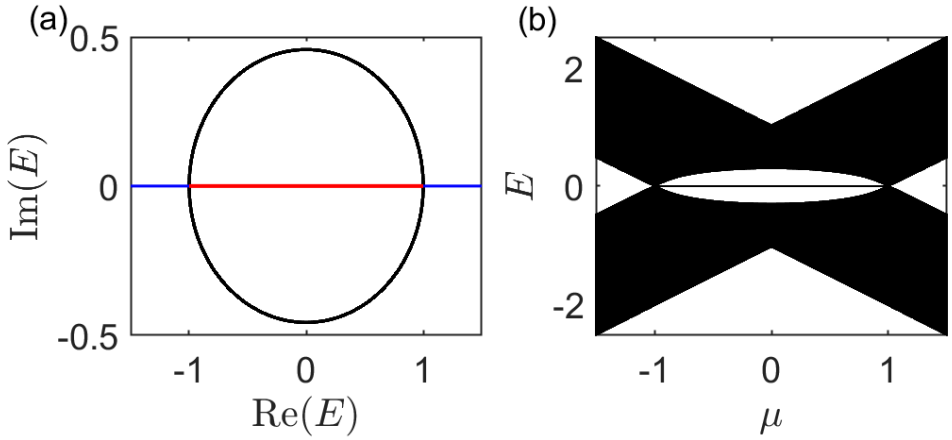

Figure 7.2: Energy spectrum of (a) non-Hermitian coupled HN model $\mathcal{H}(k)$ and (b) corresponding DIII superconductor $H(k)$, with $t = 0.5$, $\alpha_R = 0.2$, $d_x = 0.4$ and $d_z = 0.3$. (a) $\mathbb{Z}_2$ topological invariant $\nu = 1$ inside the closed curve of the complex spectrum. (b) In the region of μ encircled by the complex spectrum in (a), edge states appear in the DIII superconductor.

conditions (OBC) according to the BBC, as shown in Fig. 7.2(b).

7.3.2 Robust $\mathbb{Z}_2$ point-gap topology: Non-Hermitian system

Here, we study the robustness of $\mathbb{Z}_2$ point-gap topology of the non-Hermitian system against stacking of multiple 1D chains using the coupled Hatano-Nelson model defined by Eq. 7.14. According to Eq. (7.3), we define the stacked system $\mathcal{H}_s(k)$ as

$$\mathcal{H}_s(k) = \begin{pmatrix} \mathcal{H}(k) & \delta_0\sigma_0 + i\boldsymbol{\delta}\cdot\boldsymbol{\sigma} \\ \delta_0\sigma_0 - i\boldsymbol{\delta}\cdot\boldsymbol{\sigma} & \mathcal{H}(k) \end{pmatrix}, \tag{7.18}$$

where, δ_0 and $\boldsymbol{\delta} = (\delta_x, \delta_y, \delta_z)$ represent the strength of coupling of two 1D chains. The latter one involves the spin-dependent coupling.

For simplicity, we consider the case $\delta_x = \delta_y = 0$ hereafter. We note that, to keep the symmetry class with stacking effects, in general, the stacking term σ_0 and at least one component of $\boldsymbol{\sigma}$ should be finite. Otherwise, the Hamiltonian in Eq. (7.18) can be decomposed into two independent systems and spinful TRS† may break, as explained in Sec. 7.4. Under this simplification, the PBC spectrum can be solved as

$$E_{\eta\epsilon}(k) = 2t\cos k + i\eta r(k)e^{i\epsilon\phi(k)}, \tag{7.19}$$

where

$$r(k) = \left\{ \left[(\alpha_R^2 + d_x^2 - d_z^2) \sin^2 k - (\delta_0^2 + \delta_z^2) \right]^2 + 4 \sin^2 k \left[\delta_0^2 (\alpha_R^2 + d_x^2 - d_z^2) + \delta_z^2 d_x^2 \right] \right\}^{\frac{1}{4}}, \tag{7.20}$$

$$\phi(k) = \frac{1}{2} \arctan \frac{2 \sin k \sqrt{\delta_0^2 (\alpha_R^2 + d_x^2 - d_z^2) + \delta_z^2 d_x^2}}{(\alpha_R^2 + d_x^2 - d_z^2) \sin^2 k - (\delta_0^2 + \delta_z^2)} \in \left(-\frac{\pi}{2}, \frac{\pi}{2} \right). \tag{7.21}$$

Here, $\eta, \varepsilon = \pm$ represent the four energy bands $E_{\pm\pm}$ of $\mathcal{H}_s(k)$. Rewriting Eq. (7.19), we see that

$$E_{\eta\varepsilon}(k) = 2t \cos k - \eta\varepsilon r(k) \sin \phi(k) + i\eta r(k) \cos \phi(k). \tag{7.22}$$

Note that $\cos \phi(k) \geq 0$.

For the stacking term $\delta_0 = \delta_z = 0$, there is no coupling in the stacked system, resulting in fourfold degeneracy of the eigenvalues. In this case, the $\mathbb{Z}_2$ topological invariant ν in Eq. (7.17) becomes trivial due to the $\mathbb{Z}_2$ nature. On the other hand, when $\delta_0 \neq 0$ or $\delta_z \neq 0$, ϕ is finite in general, which results in lifting the fourfold degeneracy to double degeneracy because we see $E_{\eta+} = E_{\eta-}$ while $E_{+\varepsilon} \neq E_{-\varepsilon}$. This indicates that the level repulsion in $\mathcal{H}_s(k)$ is induced by the coupling of two chains. In Fig. 7.3, the black curves shows the PBC spectrum in Eq. (7.19) for various values of the stacking strength δ_z. As schematically explained in Fig. 7.1, we observe that the single closed ellipse with no stacking is split into two ellipses at the finite value of δ_z. Especially, the regions surrounded by split spectra expand as increasing δ_z. Remarkably, we confirmed that the $\mathbb{Z}_2$ topological invariant $\nu(E_p)$ in Eq. (7.17) becomes nontrivial when the reference point E_p locates in the expanded regions, that is, inside the ellipses except for the common region inside the two ellipses. In particular, when $\delta_z \geq \sqrt{(2t)^2 - \delta_0^2}$, all the regions enclosed by the spectrum exhibit nontrivial $\mathbb{Z}_2$ topology [Fig. 7.3 (c) and (d)].

Next, we verify the BBC of the $\mathbb{Z}_2$ point-gap topology in the stacked systems. As shown by the red curves in Fig. 7.3, which represent numerically calculated eigenvalues for the system with OBC (OBC spectra, in short), OBC spectra always emerge in the topologically nontrivial regions. Therefore, the BBC of the $\mathbb{Z}_2$ point-gap topology holds in the stacked systems.

As a technical note, when we calculate the OBC spectra, the strong finite-size effects make it impossible to obtain the OBC spectrum by directly diagonalizing $\mathcal{H}(k)$ in real space. Therefore, we apply the generalized Brillouin zone (GBZ) [148, 149] approach according to non-Bloch

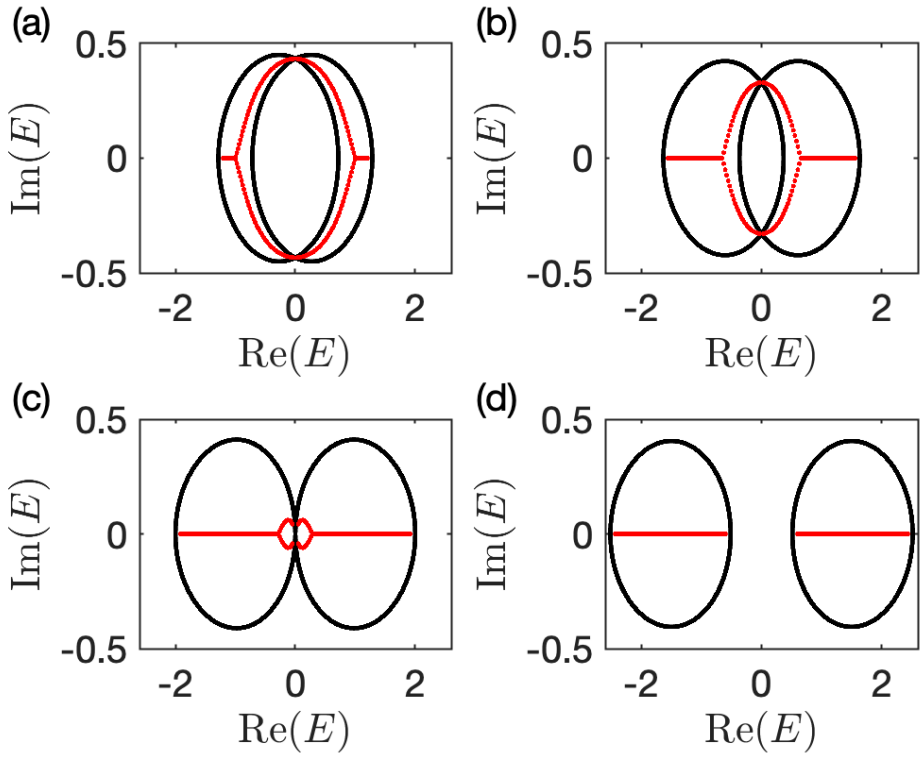

Figure 7.3: Complex energy spectrum of stacked coupled HN model $\mathcal{H}_s$ under PBC (black curves) and OBC (red curves), with parameters $t = 0.5$, $\alpha_R = 0.2$, $d_x = 0.4$, $d_z = 0.3$, $\delta_0 = 0.2$ and (a) $\delta_z = 0.2$ (b) $\delta_z = 0.6$ (c) $\delta_z = \sqrt{0.96}$ (d) $\delta_z = 1.5$.

band theory in the symplectic class [150]. The GBZ corresponding to Fig. 7.3 is shown in Fig. 7.4, by the black dots, while the unit circle (blue solid curve) represents the ordinary Brillouin zone (BZ). The points on the GBZ inside the BZ correspond to eigenmodes localized at the left boundary, while those outside the BZ represent right-boundary-localized eigenmodes. From Fig. 7.4(a), for a small value of δ_0 and δ_z, the GBZ begins to deviate from the BZ along the real axis, and the eigenmodes, especially those near the imaginary axis, are not strongly bound by the boundaries. However, for a strong stacking strength, all the eigenmodes become localized at both boundaries, as shown in Fig. 7.4, indicating the emergence of a strong $\mathbb{Z}_2$ NHSE. We note that the robustness of $\mathbb{Z}_2$ invariant is rather the general property of the stacked Hamiltonian belonging to class AII†. The same results are obtained even when using a different model, as demonstrated at the end of Sec. 7.3.2.

Furthermore, the robustness of the $\mathbb{Z}_2$ point-gap topological phase due to the level repulsion can be extended to multi-chain stacked systems. It is expected that, for an n-chain stacked system,

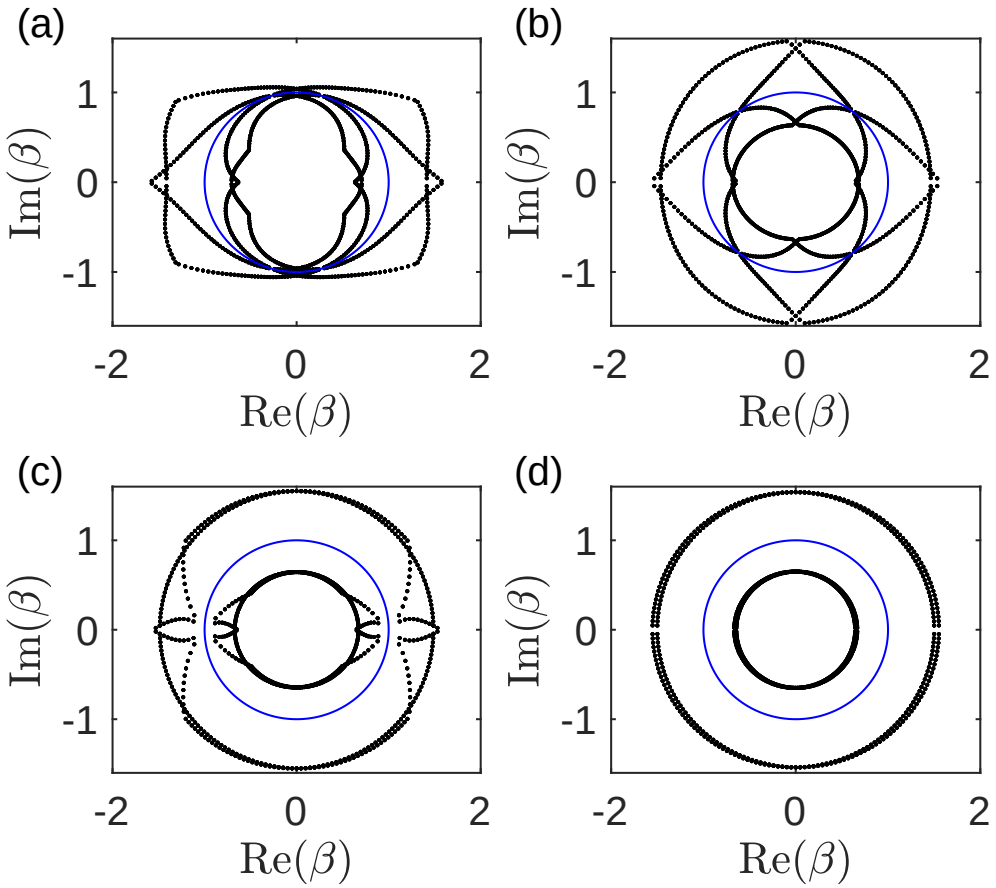

Figure 7.4: GBZ (black dots) and BZ (blue unit circle) of stacked coupled HN model $\mathcal{H}_s$, with parameters $t = 0.5$, $\alpha_R = 0.2$, $d_x = 0.4$, $d_z = 0.3$, $\delta_0 = 0.2$ and (a) $\delta_z = 0.2$ (b) $\delta_z = 0.6$ (c) $\delta_z = \sqrt{0.96}$ (d) $\delta_z = 1.5$.

the energy spectrum splits from a $2n$-degenerate curve into n double-degenerate curves and the $\mathbb{Z}_2$ topological phase would have the robustness by the same argument.

To confirm the above expectation, we consider the systems with PBC composed by three and four stacked chains, which are defined by

$$\mathcal{H}_{3s}(k) = \begin{pmatrix} \mathcal{H}(k) & \delta_0 + i\boldsymbol{\delta}\cdot\boldsymbol{\sigma} & \\ \delta_0 - i\boldsymbol{\delta}\cdot\boldsymbol{\sigma} & \mathcal{H}(k) & \delta_0 + i\boldsymbol{\delta}\cdot\boldsymbol{\sigma} \\ & \delta_0 - i\boldsymbol{\delta}\cdot\boldsymbol{\sigma} & \mathcal{H}(k) \end{pmatrix} \tag{7.23}$$

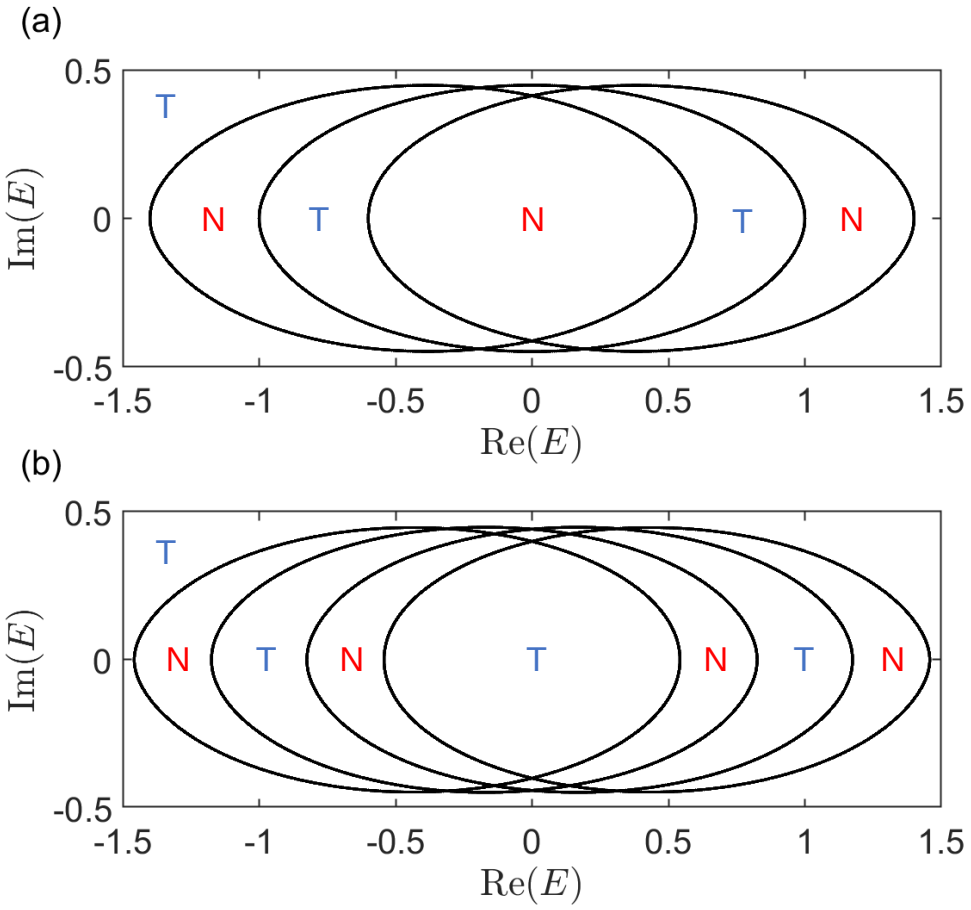

Figure 7.5: Complex energy spectrum and $\mathbb{Z}_2$ index of (a) $\mathcal{H}_{3s}(k)$ and (b) $\mathcal{H}_{4s}(k)$ with parameters $t = 0.5$, $\alpha_R = 0.2$, $d_x = 0.4$, $d_z = 0.3$, $\delta_0 = \delta_z = 0.2$ and $\sigma_x = \sigma_y = 0$. The capital T and N indicates that the $\mathbb{Z}_2$ topology is trivial or nontrivial, respectively, in the corresponding areas.

and

$$\mathcal{H}_{4s}(k) = \begin{pmatrix} \mathcal{H}(k) & \delta_0 + i\boldsymbol{\delta}\cdot\boldsymbol{\sigma} & & \\ \delta_0 - i\boldsymbol{\delta}\cdot\boldsymbol{\sigma} & \mathcal{H}(k) & \delta_0 + i\boldsymbol{\delta}\cdot\boldsymbol{\sigma} & \\ & \delta_0 - i\boldsymbol{\delta}\cdot\boldsymbol{\sigma} & \mathcal{H}(k) & \delta_0 + i\boldsymbol{\delta}\cdot\boldsymbol{\sigma} \\ & & \delta_0 - i\boldsymbol{\delta}\cdot\boldsymbol{\sigma} & \mathcal{H}(k) \end{pmatrix}, \tag{7.24}$$

respectively. Note that both $\mathcal{H}_{3s}(k)$ and $\mathcal{H}_{4s}(k)$ exhibit spinful TRS† symmetry with time-reversal operators $\mathcal{T}_{3s} = I_3 \otimes \sigma_y$ and $\mathcal{T}_{4s} = I_4 \otimes \sigma_y$, respectively. Here, I_n ($n \in \mathbb{Z}$) represents an n-dimensional identity matrix. The definition of the $\mathbb{Z}_2$ invariant is the same as before [Eq. (7.17)].

The complex energy spectra of $\mathcal{H}_{3s}(k)$ and $\mathcal{H}_{4s}(k)$ are shown in Fig. 7.5. We observe that PBC spectra of $\mathcal{H}_{3s}(k)$ and $\mathcal{H}_{4s}(k)$ split into 3 and 4 bands (ellipses) with double degeneracy,

respectively. We also confirm that the $\mathbb{Z}_2$ invariant alternatively changes value when the point gap closes.Moreover, for even-chain stacked systems, the energy at the origin is always topologically trivial, whereas for odd-chain stacked systems, the energy at the origin always shows nontrivial $\mathbb{Z}_2$ topology.

At the end of Sec. 7.3.2, we show that the results are general properties by using the other model which is originally introduced in [54]. The Hamiltonian is given by

$$\mathcal{H}_{\mathrm{c}}(k) = \begin{pmatrix} \mathcal{H}_{\mathrm{HN}}(k) & 2\Delta \sin k \\ 2\Delta \sin k & \mathcal{H}^{T}_{\mathrm{HN}}(-k) \end{pmatrix}, \tag{7.25}$$

where

$$\mathcal{H}_{\mathrm{HN}}(k) = (t+g)e^{ik} + (t-g)e^{-ik} \tag{7.26}$$

describes the Hatano-Nelson model without disorder. The parameters t and g represent the asymmetric hopping terms, while Δ denotes the coupling strength. Such a system belongs to the AII† symmetry class, and $\mathbb{Z}_2$ point gaps remain open as long as $g \neq 0$.

Similar to Eq. (7.3), we define the stacked system $\mathcal{H}_{\mathrm{s}}(k)$ as

$$\mathcal{H}_{\mathrm{s}}(k) = \begin{pmatrix} \mathcal{H}_{\mathrm{c}}(k) & \delta_0\sigma_0 + i\boldsymbol{\delta}\cdot\boldsymbol{\sigma} \\ \delta_0\sigma_0 - i\boldsymbol{\delta}\cdot\boldsymbol{\sigma} & \mathcal{H}_{\mathrm{c}}(k) \end{pmatrix}, \tag{7.27}$$

where the parameters are defined as in Eq. (7.18). For simplicity, we still consider the case where $\delta_x = \delta_y = 0$, and the energy spectrum is solved as follows:

$$E_{\eta\epsilon}(k) = 2t\cos k + i\eta r(k) e^{i\varepsilon\phi(k)}, \tag{7.28}$$

where

$$r(k) = \left\{ \left[4(g^2-\Delta^2)\sin^2 k - (\delta_0^2+\delta_z^2) \right]^2 - (4\sin k)^2 \left[\delta_0^2(g^2-\Delta^2) + \delta_z^2 g^2 \right] \right\}^{\frac{1}{4}} \tag{7.29}$$

$$\phi(k) = \frac{1}{2}\arctan \frac{4\sin k \sqrt{\delta_0^2(g^2-\Delta^2)+\delta_z^2 g^2}}{(g^2-\Delta^2)\sin^2 k - (\delta_0^2+\delta_z^2)} \in \left(-\frac{\pi}{2}, \frac{\pi}{2}\right). \tag{7.30}$$

Here, $\eta, \varepsilon = \pm$ represent the four energy bands $E_{\pm\pm}$ of $\mathcal{H}_{\mathrm{s}}(k)$. We notice that for $\delta_0 \neq 0$ or $\delta_z \neq 0$, the complex energy spectrum of $\mathcal{H}_{\mathrm{c}}(k)$ splits into a double degeneracy because of $E_{++} \neq E_{-+}$.

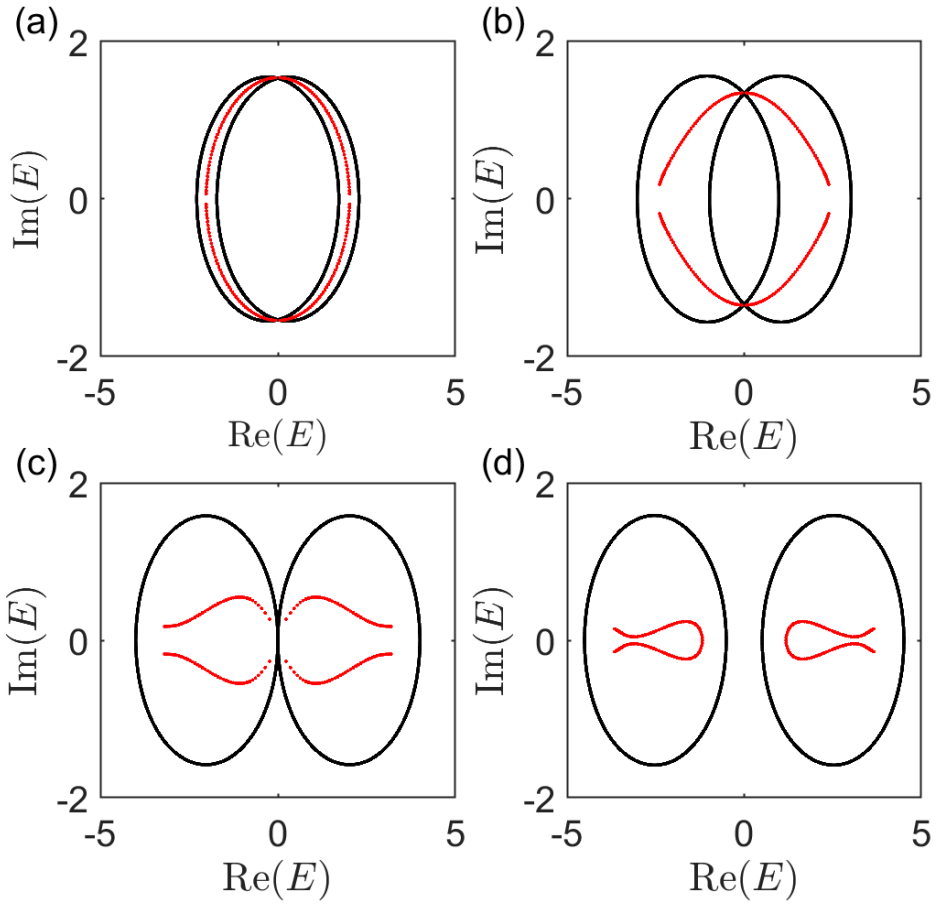

Figure 7.6: Complex energy spectrum of stacked coupled HN model $\mathcal{H}_s$ under PBC (black curves) and OBC (red curves), with parameters $t = 1$, $g = 0.8$, $\Delta = 0.2$ and $\delta_0 = 0.2$ (a) $\delta_z = 0.2$ (b) $\delta_z = 1$ (c) $\delta_z = \sqrt{3.96}$ (d) $\delta_z = 2.5$.

Figure 7.6 shows the PBC and OBC spectra of the non-Hermitian Hamiltonian $\mathcal{H}_s(k)$. The OBC spectrum is derived from the GBZ, as shown in Fig. 7.7 due to strong finite-size effects. From Fig. 7.6, we observe that the PBC spectrum forms closed curves, while the OBC spectrum forms arcs with no enclosed area, always lying within the $\mathbb{Z}_2$ nontrivial region of the PBC spectrum. This indicates the robustness of the NHSE in this model against stacking, similar to the model discussed earlier in this section.

7.3.3 Robust $\mathbb{Z}_2$ topology: Hermitian system

In this part, we show that the above-mentioned robustness of $\mathbb{Z}_2$ topological phases in non-Hermitian systems against stacking is inherited by the Hermitian systems related by the Hermi-

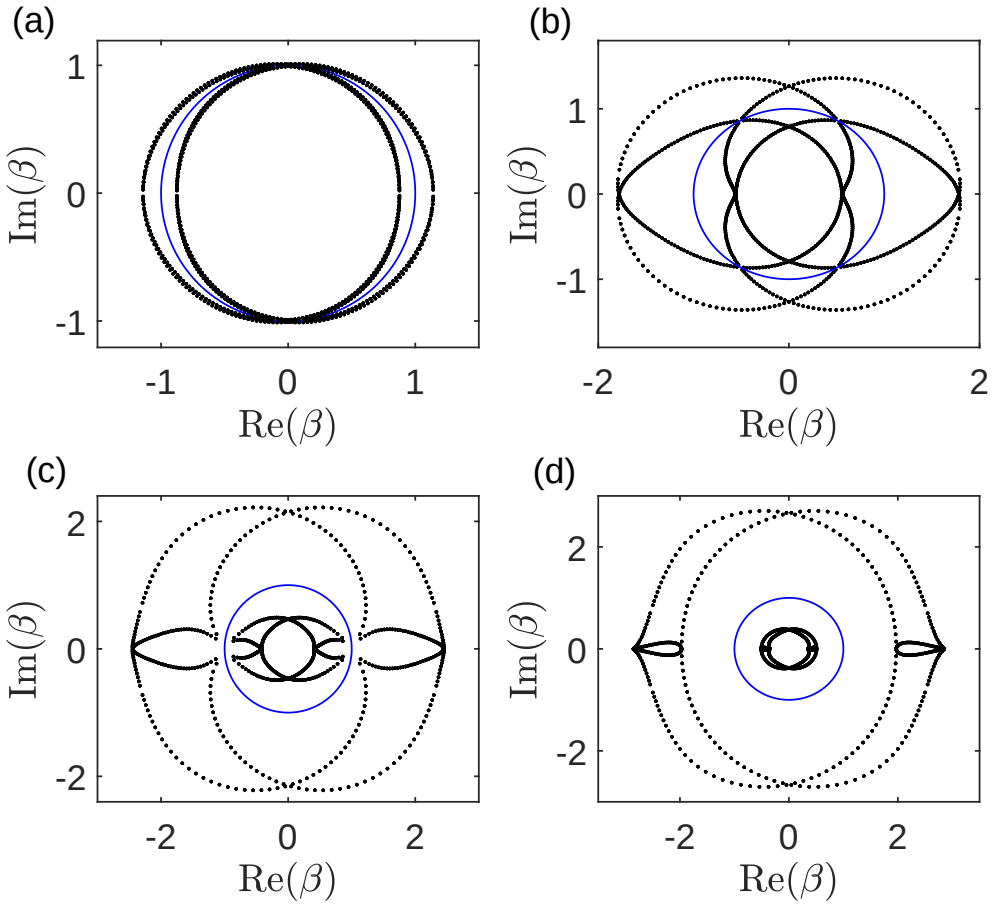

Figure 7.7: GBZ (black dots) and BZ (blue unit circle) of stacked coupled HN model $\mathcal{H}_s$, with parameters $t = 1$, $g = 0.8$, $\Delta = 0.2$ and $\delta_0 = 0.2$ (a) $\delta_z = 0.2$ (b) $\delta_z = 1$ (c) $\delta_z = \sqrt{3.96}$ (d) $\delta_z = 2.5$.

tization.

First, we introduce a Hermitian Hamiltonian by using the stacked non-Hermitian Hamiltonian in Sec. 7.3.2 through the Hermitization in Eq. (7.1) as

$$H'_s(k) = \begin{pmatrix} 0 & \mathcal{H}_s(k) - E_p\eta_0 \otimes \sigma_0 \\ \mathcal{H}_s^\dagger(k) - E_p^*\eta_0 \otimes \sigma_0 & 0 \end{pmatrix} \tag{7.31}$$

where $\mathcal{H}_s(k)$ is defined by Eq. (7.18). We note that E_p is a parameter standing for the reference point on the complex energy plain. After a unitary transformation by $H_s(k) = UH'_s(k)U^\dagger$ with

$U = e^{i\frac{\pi}{4}\eta_0\otimes\tau_y\otimes\sigma_0}$, we obtain

$$H_s(k) = \begin{pmatrix} H_{11}(k) & H_{12} \\ H_{12}^\dagger & -H_{11}^T(-k) \end{pmatrix}, \tag{7.32}$$

$$H_{11}(k) = \begin{pmatrix} h(k) - \mathrm{Re}[E_p] & \delta_0\sigma_0 + i\boldsymbol{\delta}\cdot\boldsymbol{\sigma} \\ \delta_0\sigma_0 - i\boldsymbol{\delta}\cdot\boldsymbol{\sigma} & h(k) - \mathrm{Re}[E_p] \end{pmatrix}, \tag{7.33}$$

$$H_{12} = \begin{pmatrix} i\boldsymbol{d}(k)\cdot\boldsymbol{\sigma}\sigma_y - i\mathrm{Im}[E_p] & 0 \\ 0 & i\boldsymbol{d}(k)\cdot\boldsymbol{\sigma}\sigma_y - i\mathrm{Im}[E_p] \end{pmatrix}, \tag{7.34}$$

where $h(k)$ and $\boldsymbol{d}(k)$ are defined by Eq. 7.7 and Eqs. 7.8, respectively. Here we assume that E_p is real. Rewriting E_p as a parameter μ and rearranging the order of the basis, Eq. (7.32) can be written as

$$H_s(k) = \begin{pmatrix} h(k) - \mu & i\boldsymbol{d}(k)\cdot\boldsymbol{\sigma}\sigma_y & \delta_0 + i\boldsymbol{\delta}\cdot\boldsymbol{\sigma} & 0 \\ -i\boldsymbol{d}^*(k)\cdot\boldsymbol{\sigma}\sigma_y & -h^T(-k) + \mu & 0 & -\delta_0 - i\boldsymbol{\delta}\cdot\boldsymbol{\sigma} \\ \delta_0 - i\boldsymbol{\delta}\cdot\boldsymbol{\sigma} & 0 & h(k) - \mu & i\boldsymbol{d}(k)\cdot\boldsymbol{\sigma}\sigma_y \\ 0 & -\delta_0 + i\boldsymbol{\delta}\cdot\boldsymbol{\sigma} & -i\boldsymbol{d}^*(k)\cdot\boldsymbol{\sigma}\sigma_y & -h^T(-k) + \mu \end{pmatrix}. \tag{7.35}$$

The above Hamiltonian can be interpreted as the two stacked chains of the DIII Hermitian Hermitonian in Eq. (7.9), in which each symmetry is given by

$$\mathrm{TRS} : TH^*(k)T^{-1} = H(-k),\ T = \eta_0 \otimes \tau_z \otimes \sigma_y, \tag{7.36}$$

$$\mathrm{PHS} : PH^*(k)P^{-1} = -H(-k),\ P = \eta_0 \otimes \tau_y \otimes \sigma_y, \tag{7.37}$$

$$\mathrm{CS} : \Gamma H(k)\Gamma^{-1} = -H(k),\ \Gamma = \eta_0 \otimes \tau_x \otimes \sigma_0. \tag{7.38}$$

We emphasize that we introduce E_p as the reference point in Eq. (7.31). In Sec. 7.3.1, the reference point E_p appears in Eq. (7.17) and we explain that if the non-Hermitian Hamiltonian is topologically nontrivial at the reference energy point E_p, the corresponding Hermitian Hamiltonian is also nontrivial in Fig. 7.2. Then, in Sec. 7.3.2, we show that the $\mathbb{Z}_2$ point-gap topological phase remains robust against stacking if E_p takes a proper values on the complex plain. Combining these facts, we can predict that if E_p locates at the nontrivial region for the $\mathbb{Z}_2$ index of the non-Hermitian Hamiltonian $\mathcal{H}_\mathrm{s}(k)$, the corresponding Hermitian DIII Hamiltonian $H_\mathrm{s}(k)$ should also have a nontrivial $\mathbb{Z}_2$ topological phase even in the stacked system. We verify this prediction below.

While in Sec. 7.3.2, $\delta_x = \delta_y = 0$ is studied for simplicity, we consider all the coupling terms here. Figures 7.8 (a-1) and (b-1) shows the PBC spectrum of the stacked non-Hermitian Hamiltonian $\mathcal{H}_s(k)$ with $\delta_i = 0.2$ and 0.5 for $i = 0, x, y, z$, respectively. Similar to Fig. 7.3, we observe two closed curves intersecting each other at $\delta_i = 0.2$ and attaching at $E = 0$ at $\delta_i = 0.5$, which arise from level repulsion. Note that the closed curves are not ellipses because of contributes of δ_x and δ_y. Calculating the $\mathbb{Z}_2$ invariant of $\mathcal{H}_s(k)$, we confirm that only the non-overlapping region exhibits nontrivial $\mathbb{Z}_2$ topology.

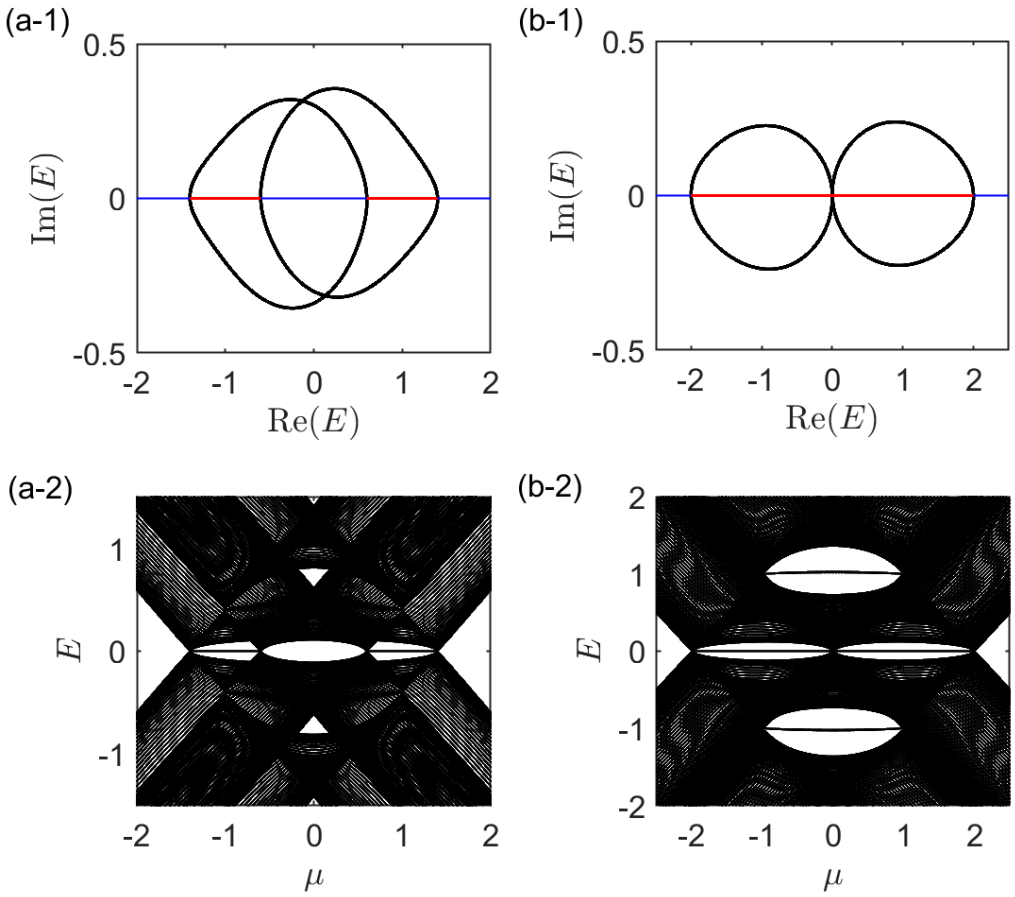

Figure 7.8: Energy spectrum of (a-1,b-1) non-Hermitian stacked coupled HN model $\mathcal{H}_s(k)$ and (a-2,b-2) the corresponding stacked DIII superconductor $H_s(k)$, with $t = 0.5$, $\alpha_R = 0.2$, $d_x = 0.4$, and $d_z = 0.3$. Panels (a-1) and (a-2) correspond to the stacking strengths $\delta_i = 0.2$ ($i = 0, x, y, z$), while panels (b-1) and (b-2) correspond to $\delta_i = 0.5$ ($i = 0, x, y, z$). When μ takes values from red line segments in (a-1) or (b-1), the corresponding Hermitian system (a-2) or (b-2) exhibits zero-energy states.

Now we study the corresponding Hermitian DIII Hamiltonian in Eq. (7.35) with OBC and

verify the stability of the zero-energy states originating from the $\mathbb{Z}_2$ topological phase. To begin with, we note the energy-gap around E 0 of the Hamiltonian close to $|\mu| = 2t \pm \sqrt{\sum_{i=0,x,y,z} \delta_i^2}$ which can be obtained as the fact that the Hamiltonian closes the gap at $k = 0, \pi$. The OBC spectra are shown in Figs. 7.8 (a-2) and (b-2). As depicted in Fig.7.8 (a-2) for $\delta_i = 0.2$, for $|\mu| < 2t - \sqrt{\sum_i \delta_i^2} = 0.9$, $H_s(k)$ exhibits trivial $\mathbb{Z}_2$ topology, and no states appear in the energy gap around $E = 0$. On the other had, for $2t - \sqrt{\sum_i \delta_i^2} < |\mu| < 2t + \sqrt{\sum_i \delta_i^2}$, $H_s(k)$ exhibits nontrivial $\mathbb{Z}_2$ topology, and fourfold-degenerate zero-energy edge states emerge even in the stacked DIII system under OBC. This demonstrates the robustness of $\mathbb{Z}_2$ topology and zero-energy edge states in a stacked system. Particularly, when the stacking strengths reach a critical value such that $\sum_i \delta_i^2 = 4t^2$, all energy points inside the PBC spectra exhibit nontrivial $\mathbb{Z}_2$ topology as shown in Fig. 7.8 (b-1). Accordingly, for all μ satisfying $0 < |\mu| < 4t$ ($\mu \neq 0$), the DIII Hermitian Hamiltonian exhibits zero-energy states as shown in Fig. 7.8 (b-2).

We can naively extend the above result to an n-chain stacked Hermitian system. Taking into account the results in Fig. 7.6 for the multi-stacked non-Hermitian Hamiltonian, the trivial and nontrivial $\mathbb{Z}_2$ invariant of the corresponding Hermitian Hamiltonian alternatively appears as the function of the (real) chemical potential μ which moves on the real axis in Fig. 7.6.

7.3.4 Revisiting previous work

So far, we have explained that the $\mathbb{Z}_2$ point-gap topology is robust against stacking due to level repulsion and then the corresponding Hamiltonian derived through the Hermitization inherits the robustness of the $\mathbb{Z}_2$ topology. We demonstrated the robustness by focusing on the specific Hamiltonian belonging to class DIII.

As we mentioned in the introduction, several works reported the nontrivial $\mathbb{Z}_2$ topology in the stacked Hermitian systems[180, 190, 191], while the reason has not yet been understood. Here we clarify that these results can by explained by non-Hermitian level repulsion.

Here we focus on Refs. [190, 191] in which the stacking of the 2D QSH insulator approaching to the 3D Wilson-Dirac-type Hamiltonian is studied. It is shown that the $\mathbb{Z}_2$ invariant defined for the 2D QSH insulator remains robust against the number of stacked systems as a function of a mass parameter (equivalent to μ in our model). While the QSH insulator generally belongs to class AII, the on-site random potential term is ignored for the calculation of the $\mathbb{Z}_2$ invariant. In

this case, the Hamiltonian recovers chiral symmetry and belongs to class DIII which makes it possible to derive the corresponding non-Hermitian Hamiltonian belonging to class AII†. Thereby, the robustness of the $\mathbb{Z}_2$ invariant in Refs. [190, 191] can be explained by level repulsion of the non-Hermitian Hamiltonian.

7.4 Influence of stacking configuration on topology

In this section, we explain why we need to consider, at least, two terms of the stacking terms $\delta_0 + i\boldsymbol{\delta}\cdot\boldsymbol{\sigma}$ when defining the stacked system in Sec. 7.3.3. We show that the Hamiltonian is decoupled into two independent ones and the symmetry class may also change if we consider only a single stacking term.

7.4.1 $\delta_0 \neq 0$, $\delta_x = \delta_y = \delta_z = 0$

First, we consider the simplest case by focusing only on a spin-independent stacking term, δ_0. The stacked non-Hamiltonian, $\mathcal{H}_{s0}(k)$, is expressed as follows:

$$\mathcal{H}_{s0}(k) = \begin{pmatrix} \mathcal{H}(k) & \delta_0\sigma_0 \\ \delta_0\sigma_0 & \mathcal{H}(k) \end{pmatrix}. \tag{7.39}$$

By applying a unitary transformation with $\mathcal{U}_0 = e^{-i\frac{\pi}{4}\eta_y\otimes\sigma_0}$, we can obtain a diagonal block Hamiltonian

$$\begin{aligned} \mathcal{H}'_{s0}(k) &= \mathcal{U}_0\mathcal{H}_{s0}(k)\mathcal{U}_0^{-1} \\ &= \begin{pmatrix} \mathcal{H}(k) - \delta_0\sigma_0 & \\ & \mathcal{H}(k) + \delta_0\sigma_0 \end{pmatrix} \\ &= \begin{pmatrix} \mathcal{H}_0^{(1)}(k) & \\ & \mathcal{H}_0^{(2)}(k) \end{pmatrix}. \end{aligned} \tag{7.40}$$

$\mathcal{H}_0^{(1)}(k)$ and $\mathcal{H}_0^{(2)}(k)$ represent two decoupled systems belonging to the AII† class, each acquiring nontrivial $\mathbb{Z}_2$ topology at the energy points enclosed by their own spectrum [Fig.7.9(a)]. As illustrated in Fig.7.9(b), the corresponding Hermitian Hamiltonian H_{s0} exhibits zero-energy edge states in both regions $|\mu| < 2t - |\delta_0|$ and $2t - |\delta_0| < |\mu| < 2t + |\delta_0|$, protected by nontrivial $\mathbb{Z}_2$ topology.

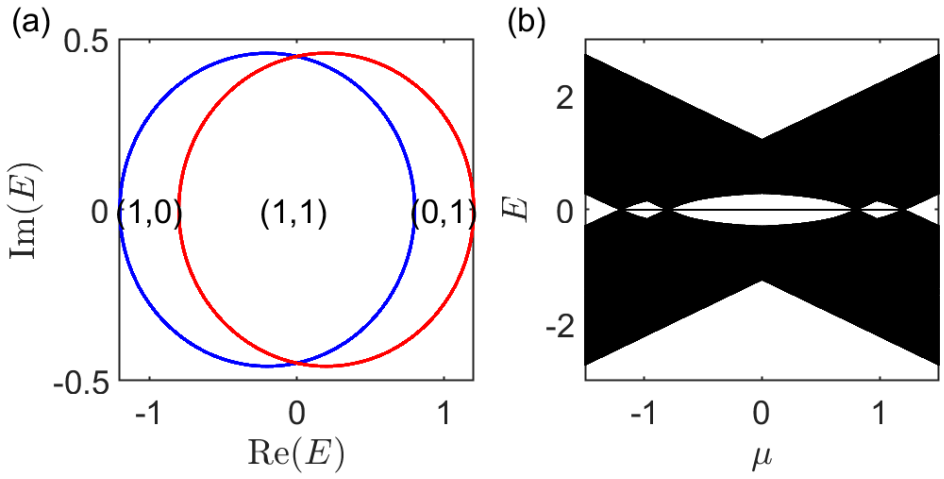

Figure 7.9: (a) Energy spectrum of $\mathcal{H}_0^{(1)}(k)$ (blue curve) and $\mathcal{H}_0^{(2)}(k)$ (red curve). The numbers present the $\mathbb{Z}_2$ topological number of $\mathcal{H}_0^{(1)}(k)$ and $\mathcal{H}_0^{(2)}(k)$, respectively. (b) Real energy spectrum of the corresponding stacked Hermitian system, with $t = 0.5$, $\alpha_R = 0.2$, $d_x = 0.4$, $d_z = 0.3$, $\delta_0 = 0.2$ and $\delta_x = \delta_y = \delta_z = 0$. The system exhibits zero-energy edge states in both regions $|\mu| < 0.8$ and $0.8 < |\mu| < 1.2$.

7.4.2 $\delta_z \neq 0$, $\delta_0 = \delta_x = \delta_y = 0$

Here, we consider the case of focusing solely on the spin-dependent stacking term σ_z. The stacked non-Hermitian Hamiltonian, $\mathcal{H}_{sz}(k)$, is expressed as follows:

$$\mathcal{H}_{sz}(k) = \begin{pmatrix} \mathcal{H}(k) & i\delta_z\sigma_z \\ -i\delta_z\sigma_z & \mathcal{H}(k) \end{pmatrix}, \tag{7.41}$$

By applying a unitary transformation with $\mathcal{U}_z = e^{-i\frac{\pi}{4}\eta_x\otimes\sigma_0}$, we can obtain a diagonal block Hamiltonian

$$\begin{aligned} \mathcal{H}'_{sz}(k) &= \mathcal{U}_z\mathcal{H}_{sz}(k)\mathcal{U}_z^{-1} \\ &= \begin{pmatrix} \mathcal{H}(k) - \delta_z\sigma_z & \\ & \mathcal{H}(k) + \delta_z\sigma_z \end{pmatrix} \\ &= \begin{pmatrix} \mathcal{H}_z^{(1)}(k) & \\ & \mathcal{H}_z^{(2)}(k) \end{pmatrix}. \end{aligned} \tag{7.42}$$

$\mathcal{H}_z^{(1)}(k)$ and $\mathcal{H}_z^{(2)}(k)$ are two decoupled systems, both belonging to the class A symmetry class, without TRS, PHS, or CS. Such systems achieve $\mathbb{Z}$ point-gap topology in 1D systems.

As shown in Fig. 7.10, the energy spectra of $\mathcal{H}_z^{(1)}(k)$ and $\mathcal{H}_z^{(2)}(k)$ coincide with each other,

given by $E_{\eta,\varepsilon} = 2t\cos k + \eta\sqrt{(id_x \sin k + \varepsilon d_z)^2 + (\alpha_R^2 - d_z^2)\sin k^2}$, where $\eta, \varepsilon = \pm 1$. However, they consistently exhibit opposite winding numbers at the same energy point, leading to the emergence of zero-energy edge states in the region $2t - |\delta_z| < |\mu| < 2t + |\delta_z|$, protected by nontrivial $\mathbb{Z}$ topology, but not $\mathbb{Z}_2$ topology.

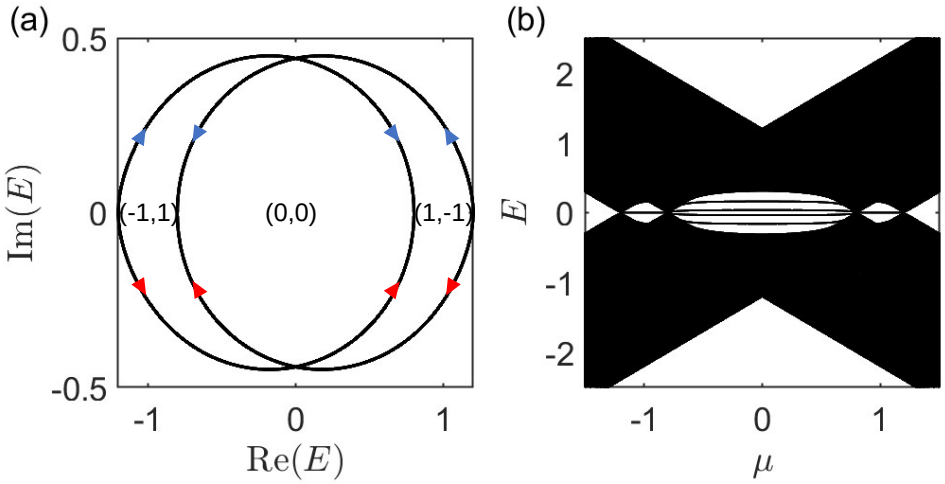

Figure 7.10: Energy spectrum of (a) coincident $\mathcal{H}_z^{(1)}(k)$ and $\mathcal{H}_z^{(2)}(k)$ and (b) the corresponding Hermitian system, with $t = 0.5$, $\alpha_R = 0.2$, $d_x = 0.4$, $d_z = 0.3$, $\delta_z = 0.2$ and $\delta_0 = \delta_x = \delta_y = 0$. The numbers in (a) indicate the winding number of $\mathcal{H}_z^{(1)}(k)$ and $\mathcal{H}_z^{(2)}(k)$ in the corresponding areas, while the direction of rotation of the energy spectrum is marked by blue arrows ($\mathcal{H}_z^{(1)}(k)$) and red arrows ($\mathcal{H}_z^{(2)}(k)$). The Hermitian system H_{sz} exhibits zero-energy edge states in the region $0.8 < |\mu| < 1.2$.

7.4.3 $\delta_x \neq 0$, $\delta_0 = \delta_y = \delta_z = 0$

In the case of only the spin-dependent stacking term $\delta_x \neq 0$, we employ the same method as when $\delta_z \neq 0$. The stacked Hamiltonian, $\mathcal{H}_{sx}(k)$, is expressed as follows:

$$\mathcal{H}_{sx}(k) = \begin{pmatrix} \mathcal{H}(k) & i\delta_x\sigma_x \\ -i\delta_x\sigma_x & \mathcal{H}(k) \end{pmatrix}, \tag{7.43}$$

By a unitary transform by $\mathcal{U}_x = e^{-i\frac{\pi}{4}\eta_x\otimes\sigma_0}$, we can get a diagonal block Hamiltonian

$$\begin{aligned}\mathcal{H}'_{sx}(k) &= \mathcal{U}_x\tilde{H}_{sx}(k)\mathcal{U}_x^{-1} \\ &= \begin{pmatrix}\mathcal{H}(k)-\delta_x\sigma_x & \\ & \mathcal{H}(k)+\delta_x\sigma_x\end{pmatrix} \\ &= \begin{pmatrix}\mathcal{H}_x^{(1)}(k) & \\ & \mathcal{H}_x^{(2)}(k)\end{pmatrix}.\end{aligned} \tag{7.44}$$

Here, neither $\mathcal{H}_x^{(1)}(k)$ nor $\mathcal{H}_x^{(2)}(k)$ possess any symmetries, which results in the A symmetry class. Since the symmetry of $\mathcal{H}_{sx}$ is the same as that of $\mathcal{H}_{sz}$, H_{sx} also achieves zero-energy edge states in the region $2t-|\delta_x|<|\mu|<2t+|\delta_x|$, protected by nontrivial $\mathbb{Z}$ topology.

7.4.4 $\delta_y \neq 0$, $\delta_0=\delta_x=\delta_z=0$

Here, we focus on the spin-dependent stacking term, σ_y. The corresponding stacked non-Hamiltonian, $\mathcal{H}_{sy}(k)$, is expressed as follows:

$$\mathcal{H}_{sy}(k) = \begin{pmatrix}\mathcal{H}(k) & i\delta_y\sigma_y \\ -i\delta_y\sigma_y & \mathcal{H}(k)\end{pmatrix}, \tag{7.45}$$

by a unitary transform by $\mathcal{U}_y = e^{-i\frac{\pi}{4}\eta_x\otimes\sigma_0}$, we can get a diagonal block Hamiltonian

$$\begin{aligned}\mathcal{H}'_{sy}(k) &= \mathcal{U}_y\mathcal{H}_{sy}(k)\mathcal{U}_y^{-1} \\ &= \begin{pmatrix}\mathcal{H}(k)-\delta_y\sigma_y & \\ & \mathcal{H}(k)+\delta_y\sigma_y\end{pmatrix} \\ &= \begin{pmatrix}\mathcal{H}_y^{(1)}(k) & \\ & \mathcal{H}_y^{(2)}(k)\end{pmatrix}.\end{aligned} \tag{7.46}$$

Similar to the case discussed in Appendix 7.4.3, neither $\mathcal{H}_y^{(1)}(k)$ nor $\mathcal{H}_y^{(2)}(k)$ possess any symmetries. The eigenenergies can be obtained by solving the characteristic equation, as shown here:

$$E_{\eta,\varepsilon} = 2t\cos k + \eta\sqrt{(\alpha_R\sin k+\varepsilon\delta_y)^2-(d_x^2+d_y^2)\sin^2 k}, \tag{7.47}$$

where $\eta,\epsilon=\pm1$. There must be a critical value k_c, such that for $k\in(0,k_c)$, $(\alpha_R\sin k\pm\delta_y)^2-(d_x^2+d_y^2)\sin^2 k>0$, leading to the emergence of real eigenenergies $E\in(\pm2t-|\sigma_y|,\pm2t+|\sigma_y|)$. The

energy gap always closes for $2t-|\delta_y| < |\mu| < 2t+|\delta_y|$ in our model. As for the region $|\mu| < 2t-|\delta_y|$, there is no zero-energy edge states due to the trivial topology.

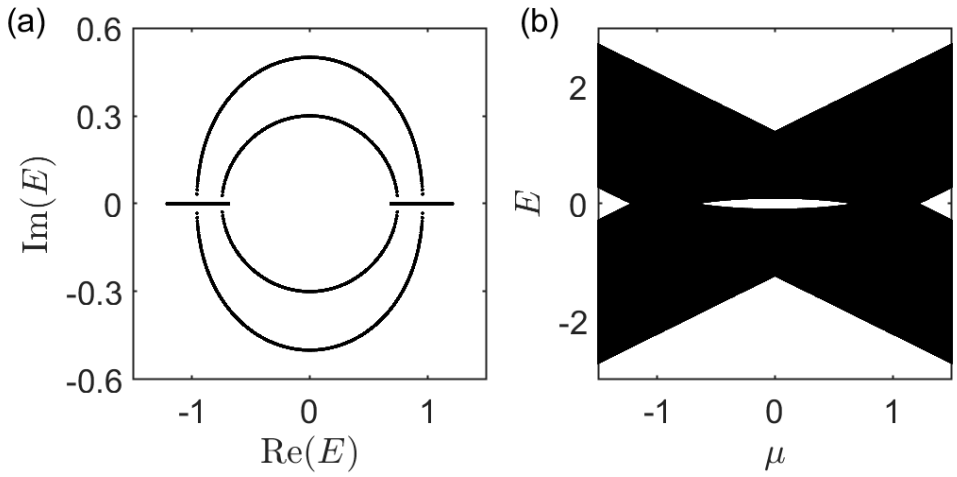

Figure 7.11: Energy spectrum of (a) non-Hermitian Hamiltonian $\mathcal{H}_{sy}(k)$ and (b) stacked Hermitian Hamiltonian H_{sy}, with $t = 0.5$, $\alpha_R = 0.2$, $d_x = 0.4$, $d_z = 0.3$, $\delta_y = 0.2$ and $\delta_0 = \delta_x = \delta_z = 0$. The point-gap is closed in the region of $0.8 < |\mu| < 1.2$, and no zero-energy edge states emerge in Hermitian system H_{sy}.

In summary, if we introduce only the spin-independent stacking term δ_0, the non-Hermitian Hamiltonian can be represented by two decoupled subsystems with $\mathbb{Z}_2$ point-gap topology using the unitary operator $e^{-i\frac{\pi}{4}\eta_y\otimes\sigma_0}$. If we introduce only σ_x or σ_z, the non-Hermitian Hamiltonian can be achieved by two decoupled subsystems with opposite winding numbers using the unitary operator $e^{-i\frac{\pi}{4}\eta_x\otimes\sigma_0}$, and the edge states are protected by nontrivial $\mathbb{Z}$ topology. If we introduce only σ_y stacking, the point gap of the non-Hermitian Hamiltonian will close on the real axis, causing the zero-energy states to disappear. By introducing both the stacking term δ_0 and $\delta_{x/y/z}$ simultaneously, we can avoid the system decoupling into two subsystems and ensure that the zero-energy edge states are protected by $\mathbb{Z}_2$ topology.

7.5 Summary and discussion

As a summary, in this work, we proposed the perspective that non-Hermitian level repulsion is the fundamental reason behind the robustness of $\mathbb{Z}_2$ topology in Hermitian systems. Our main methodology involves connecting the topological properties of Hermitian systems with those of non-Hermitian systems through a transformation called Hermitization. While the $\mathbb{Z}_2$ invariant

of stacked Hermitian systems becomes trivial or nontrivial depending on system parameters, the energy region of the nontrivial $\mathbb{Z}_2$ invariant in the non-Hermitian Hamiltonian originates from level repulsion which can be easily understood since only the two-fold degeneracy is guaranteed by Kramers pairs.

To demonstrate our general argument, we studied the 1D DIII topological superconductor with chiral symmetry. Through unitary transformations and inverse Hermitization, we establish a connection with a stacked coupled Hatano-Nelson model in the AII† symmetry class. As predicted, the energy spectrum of the stacked non-Hermitian system shows level repulsion and we confirmed the existence of $\mathbb{Z}_2$ nontrivial regions on the energy complex plain. Then, we clarified that the corresponding stacked Hermitian system also become $\mathbb{Z}_2$ topologically nontrivial when the chemical potential μ locates at the real axis on the nontrivial regions.

Furthermore, we showed that the robustness of the $\mathbb{Z}_2$ topological invariant of the stacked QSH insulators studied in Refs. [190, 191] can be well explained by level repulsion of the corresponding non-Hermitian system since the system without on-site disordered potential has chiral symmetry and belongs to class DIII in 2D. We emphasize again that the nontrivial $\mathbb{Z}_2$ topology can be easily understood as the consequence of level repulsion in the case of non-Hermitian Hamiltonians.

Finally, we note several open questions. We explained that Ref. [180], which studies the stacked Kitaev chains belonging to class D also observed the robustness of the $\mathbb{Z}_2$ topological invariant against disorder, while there is no chiral symmetry in class D. While the kitaev model can be transformed into class BDI which possesses chiral symmetry after a proper gauge transformation, the corresponding non-Hermitian system belongs to class AI and has $\mathbb{Z}$ point-gap topology. Thereby, we cannot apply our theory to this system. The system studied by Refs. [190, 191] also loses chiral symmetry if the system has on-site disorder potential, but nevertheless the conductance is well quantized. These results might be able to be explained by generalizing the current theory, which will be addressed in future work.

Chapter 8

Summary and Outlook

In this doctoral thesis, we investigate the $\mathbb{Z}_2$ point-gap topology in non-Hermitian systems from three interrelated perspectives: theoretical analysis, experimental realization, and potential applications. Our research focuses on two distinct yet complementary platforms: Floquet systems, represented by nonunitary quantum walks, and stacked systems. Each platform is studied independently yet complementarily to provide a comprehensive and cohesive understanding of the $\mathbb{Z}_2$ point-gap topology.

In the first part of our research, we propose an extension of the symmetry classification of non-Hermitian systems. We show that non-Hermitian systems can always be classified in two distinct ways: based on the symmetry relations for non-Hermitian Hamiltonians and those for nonunitary time-evolution operators. This is based on the fact that there is no strict difference in the mathematical definition between non-Hermitian Hamiltonians and nonunitary time-evolution operators. We call the proposed method "*dual symmetry classification*." This classification approach enables non-Hermitian systems to exhibit a broader range of nontrivial topological phases than those considered in previous classification methods.

In addition, we apply the dual symmetry classification to a time-evolution operator defined for nonunitary quantum walks, which provides a novel arena for studying non-Hermitian physics even within the quantum realm. By treating the time-evolution operator as a non-Hermitian Hamiltonian, we successfully define a nonunitary quantum walk with spinful time-reversal symmetry and confirm that the nonunitary quantum walk exhibits $\mathbb{Z}_2$ point gaps and the $\mathbb{Z}_2$ non-Hermitian skin effect.

In the second part of our research, we highlight the advantages of leveraging non-Hermitian

perspectives to explore Hermitian topological systems. As an application, we use $\mathbb{Z}_2$ point-gap topology to provide a systematic understanding of why the $\mathbb{Z}_2$ topological phase remains robust against stacking in the presence of chiral symmetry. We show that this robustness originates from the level repulsion of the corresponding non-Hermitian Hamiltonian derived through a Hermitization procedure. Considering the spectrum of the non-Hermitian Hamiltonian, we can clearly understand the emergence of the robust $\mathbb{Z}_2$ topological invariant by determining whether the energy winding around a reference point on the complex energy plane is even or odd. Our analysis relies on a novel correspondence through Hermitization, showing that the reference point E_p on the complex energy plane of the non-Hermitian system is mapped to the chemical potential μ of the Hermitian system with chiral symmetry. This relationship implies that the energy region for nontrivial $\mathbb{Z}_2$ point-gap topology aligns precisely with the range of μ where the $\mathbb{Z}_2$ topological phase of the Hermitian system is nontrivial and zero-energy states appear.

We further substantiated our theoretical findings by studying a class DIII superconductor with $\mathbb{Z}_2$ topology and its corresponding non-Hermitian system in symmetry class AII†, which exhibits $\mathbb{Z}_2$ point-gap topology. In the non-Hermitian system, when two layers are stacked, the fourfold degeneracy of the spectrum reduces to a twofold degeneracy due to level repulsion between Kramers pairs. Crucially, the $\mathbb{Z}_2$ point-gap topology persists, ensuring the robustness of the corresponding DIII superconductor against stacking within the range of μ corresponding to E_p, and the system continues to exhibit zero-energy states.

Through this series of studies, we have expanded the symmetry classification methods for non-Hermitian systems, revealed the unique topological and dynamical properties of $\mathbb{Z}_2$ point-gap topology, and demonstrated the advantages of adopting a non-Hermitian perspective to investigate Hermitian topological systems. These discoveries provide a theoretical foundation for novel topological phenomena in non-Hermitian systems, propelling the development of non-Hermitian topological phases. Looking ahead, we hope that these theoretical results can be experimentally validated and applied in real physical systems, further deepening our understanding of non-Hermitian topological phases.

Acknowledgements

This thesis is dedicated to all those who have supported me throughout this journey.

First and foremost, I would like to express my heartfelt gratitude to my advisor, Prof. Hideaki Obuse, whose guidance and mentorship have been invaluable throughout my doctoral research. I am also deeply thankful to my collaborators, Prof. Masatoshi Sato and Prof. Ryo Okamoto, for their insightful feedback and steadfast support, which significantly contributed to the development of my research.

I am profoundly grateful to Profs. Kousuke Yakubo, Yasuhiro Asano, Franco Nori, Naomichi Hatano, and Ken-Ichiro Imura for their insightful discussions, which have greatly enhanced my understanding and broadened my perspective. My thanks also extend to the members of the Laboratory of Condensed Matter Physics, the Laboratory of Solid State Physics, and the Laboratory of Theoretical Solid State Physics. Their camaraderie and support have made my three years abroad both rewarding and memorable. I would also like to acknowledge the financial support from JST SPRING (Grant No. JPMJSP2119), which has been essential for both my research and daily life.

Finally, I wish to express my deepest gratitude to my parents, Prof. Xiong Jiang and Ms. Jifang Shi; my maternal grandparents, Mr. Weihan Shi and Ms. Jine Guo; and my partner, Dr. Ting-ting Ma. Their unwavering encouragement and support have been my greatest source of strength, enabling me to dedicate myself fully to my academic pursuits.

References

[1] L. Landau, The Theory of Phase Transitions, Nature **138**, 840 (1936).

[2] V. L. Ginzburg and L. Landau, *On the Theory of Superconductivity* (Springer, 2009).

[3] K. v. Klitzing, G. Dorda, and M. Pepper, New Method for High-Accuracy Determination of the Fine-Structure Constant Based on Quantized Hall Resistance, Physical Review Letters **45**, 494 (1980).

[4] D. C. Tsui, H. L. Stormer, and A. C. Gossard, Two-Dimensional Magnetotransport in the Extreme Quantum Limit, Physical Review Letters **48**, 1559 (1982).

[5] R. B. Laughlin, Anomalous Quantum Hall Effect: An Incompressible Quantum Fluid with Fractionally Charged Excitations, Physical Review Letters **50**, 1395 (1983).

[6] F. D. M. Haldane, Model for a Quantum Hall Effect without Landau Levels: Condensed-Matter Realization of the "Parity Anomaly", Physical Review Letters **61**, 2015 (1988).

[7] X.-G. Wen, TOPOLOGICAL ORDERS IN RIGID STATES, International Journal of Modern Physics B **4**, 239 (1990).

[8] C. L. Kane and E. J. Mele, Z_2 Topological Order and The Quantum Spin Hall Effect, Physical Review Letters **95**, 146802 (2005).

[9] C. L. Kane and E. J. Mele, Quantum Spin Hall Effect in Graphene, Physical Review Letters **95**, 226801 (2005).

[10] C.-Z. Chang, J. Zhang, X. Feng, J. Shen, Z. Zhang, M. Guo, K. Li, Y. Ou, P. Wei, L.-L. Wang, Z.-Q. Ji, Y. Feng, S. Ji, X. Chen, J. Jia, X. Dai, Z. Fang, S.-C. Zhang, K. He, Y. Wang, L. Lu, X.-C. Ma, and Q.-K. Xue, Experimental Observation of the Quantum Anomalous Hall Effect in a Magnetic Topological Insulator, Science **340**, 167 (2013).

[11] M. Z. Hasan and C. L. Kane, Colloquium: Topological insulators, Reviews of Modern Physics **82**, 3045 (2010).

[12] X.-L. Qi and S.-C. Zhang, Topological insulators and superconductors, Reviews of Modern Physics **83**, 1057 (2011).

[13] M. Konig, S. Wiedmann, C. Brune, A. Roth, H. Buhmann, L. W. Molenkamp, X.-L. Qi, and S.-C. Zhang, Quantum spin Hall insulator state in HgTe quantum wells, Science **318**, 766 (2007).

[14] D. Hsieh, D. Qian, L. Wray, Y. Xia, Y. S. Hor, R. J. Cava, and M. Z. Hasan, A topological Dirac insulator in a quantum spin Hall phase, Nature **452**, 970 (2008).

[15] Y. Xia, D. Qian, D. Hsieh, L. Wray, A. Pal, H. Lin, A. Bansil, D. Grauer, Y. S. Hor, R. J. Cava, *et al.*, Observation of a large-gap topological-insulator class with a single Dirac cone on the surface, Nature Physics **5**, 398 (2009).

[16] H. Zhang, C.-X. Liu, X.-L. Qi, X. Dai, Z. Fang, and S.-C. Zhang, Topological insulators in Bi_2Se_3, Bi_2Te_3 and Sb_2Te_3 with a single Dirac cone on the surface, Nature Physics **5**, 438 (2009).

[17] D. Hsieh, Y. Xia, L. Wray, D. Qian, A. Pal, J. Dil, J. Osterwalder, F. Meier, G. Bihlmayer, C. Kane, *et al.*, Observation of unconventional quantum spin textures in topological insulators, Science **323**, 919 (2009).

[18] M. C. Rechtsman, J. M. Zeuner, Y. Plotnik, Y. Lumer, D. Podolsky, F. Dreisow, S. Nolte, M. Segev, and A. Szameit, Photonic Floquet topological insulators, Nature **496**, 196 (2013).

[19] L. Lu, J. D. Joannopoulos, and M. Soljačić, Topological photonics, Nature Photonics **8**, 821 (2014).

[20] G. Ma and P. Sheng, Acoustic metamaterials: From local resonances to broad horizons, Science Advances **2**, e1501595 (2016).

[21] C. He, Z. Li, X. Ni, X.-C. Sun, S.-Y. Yu, M.-H. Lu, X.-P. Liu, and Y.-F. Chen, Topological phononic states of underwater sound based on coupled ring resonators, Applied Physics Letters **108** (2016).

[22] M. Aidelsburger, M. Atala, M. Lohse, J. T. Barreiro, B. Paredes, and I. Bloch, Realization of the Hofstadter Hamiltonian with Ultracold Atoms in Optical Lattices, Physical Review Letters **111**, 185301 (2013).

[23] G. Jotzu, M. Messer, R. Desbuquois, M. Lebrat, T. Uehlinger, D. Greif, and T. Esslinger, Experimental realization of the topological Haldane model with ultracold fermions, Nature **515**, 237 (2014).

[24] Y. Ashida, Z. Gong, and M. Ueda, Non-Hermitian physics, Advances in Physics **69**, 249 (2020).

[25] N. Okuma and M. Sato, Non-Hermitian Topological Phenomena: A Review, Annual Review of Condensed Matter Physics **14**, 83 (2023).

[26] Z. Lin, H. Ramezani, T. Eichelkraut, T. Kottos, H. Cao, and D. N. Christodoulides, Unidirectional Invisibility Induced by $\mathcal{PT}$-Symmetric Periodic Structures, Physical Review Letters **106**, 213901 (2011).

[27] A. Regensburger, C. Bersch, M.-A. Miri, G. Onishchukov, D. N. Christodoulides, and U. Peschel, Parity-time synthetic photonic lattices, Nature **488**, 167 (2012).

[28] L. Feng, Y.-L. Xu, W. S. Fegadolli, M.-H. Lu, J. E. Oliveira, V. R. Almeida, Y.-F. Chen, and A. Scherer, Experimental demonstration of a unidirectional reflectionless parity-time metamaterial at optical frequencies, Nature Materials **12**, 108 (2013).

[29] S. Weimann, M. Kremer, Y. Plotnik, Y. Lumer, S. Nolte, K. G. Makris, M. Segev, M. C. Rechtsman, and A. Szameit, Topologically protected bound states in photonic parity-time-symmetric crystals, Nature Materials **16**, 433 (2017).

[30] H. Zhou, C. Peng, Y. Yoon, C. W. Hsu, K. A. Nelson, L. Fu, J. D. Joannopoulos, M. Soljačić, and B. Zhen, Observation of bulk Fermi arc and polarization half charge from paired exceptional points, Science **359**, 1009 (2018).

[31] H. Zhao, X. Qiao, T. Wu, B. Midya, S. Longhi, and L. Feng, Non-Hermitian topological light steering, Science **365**, 1163 (2019).

[32] J. Ningyuan, C. Owens, A. Sommer, D. Schuster, and J. Simon, Time- and Site-Resolved Dynamics in a Topological Circuit, Physical Review X **5**, 021031 (2015).

[33] M. Ezawa, Non-Hermitian higher-order topological states in nonreciprocal and reciprocal systems with their electric-circuit realization, Physical Review B **99**, 201411 (2019).

[34] M. Ezawa, Braiding of Majorana-like corner states in electric circuits and its non-Hermitian generalization, Physical Review B **100**, 045407 (2019).

[35] T. Helbig, T. Hofmann, S. Imhof, M. Abdelghany, T. Kiessling, L. Molenkamp, C. Lee, A. Szameit, M. Greiter, and R. Thomale, Generalized bulk-boundary correspondence in non-Hermitian topolectrical circuits, Nature Physics **16**, 747 (2020).

[36] T. Yoshida, T. Mizoguchi, and Y. Hatsugai, Mirror skin effect and its electric circuit simulation, Physical Review Research **2**, 022062 (2020).

[37] T. Hofmann, T. Helbig, F. Schindler, N. Salgo, M. Brzezińska, M. Greiter, T. Kiessling, D. Wolf, A. Vollhardt, A. Kabaši, *et al.*, Reciprocal skin effect and its realization in a topolectrical circuit, Physical Review Research **2**, 023265 (2020).

[38] S. Liu, R. Shao, S. Ma, L. Zhang, O. You, H. Wu, Y. J. Xiang, T. J. Cui, and S. Zhang, Non-Hermitian Skin Effect in a Non-Hermitian Electrical Circuit, Research (2021).

[39] S. Diehl, E. Rico, M. A. Baranov, and P. Zoller, Topology by dissipation in atomic quantum wires, Nature Physics **7**, 971 (2011).

[40] F. Song, S. Yao, and Z. Wang, Non-Hermitian Skin Effect and Chiral Damping in Open Quantum Systems, Physical Review Letters **123**, 170401 (2019).

[41] S. Lieu, M. McGinley, and N. R. Cooper, Tenfold Way for Quadratic Lindbladians, Physical Review Letters **124**, 040401 (2020).

[42] T.-t. Ma, D. B. Horoshko, C.-s. Yu, and S. Y. Kilin, Photon and phonon statistics in a qubit-plasmon-phonon ultrastrong-coupling system, Physical Review A **105**, 053718 (2022).

[43] K. Kawabata, K. Shiozaki, M. Ueda, and M. Sato, Symmetry and Topology in Non-Hermitian Physics, Physical Review X **9**, 041015 (2019).

[44] Z. Gong, Y. Ashida, K. Kawabata, K. Takasan, S. Higashikawa, and M. Ueda, Topological Phases of Non-Hermitian Systems, Physical Review X **8**, 031079 (2018).

[45] F. K. Kunst, E. Edvardsson, J. C. Budich, and E. J. Bergholtz, Biorthogonal Bulk-Boundary Correspondence in Non-Hermitian Systems, Physical Review Letters **121**, 026808 (2018).

[46] L. Jin and Z. Song, Bulk-boundary correspondence in a non-Hermitian system in one dimension with chiral inversion symmetry, Physical Review B **99**, 081103 (2019).

[47] H. Jiang, L.-J. Lang, C. Yang, S.-L. Zhu, and S. Chen, Interplay of non-Hermitian skin effects and Anderson localization in nonreciprocal quasiperiodic lattices, Physical Review B **100**, 054301 (2019).

[48] E. Edvardsson, F. K. Kunst, and E. J. Bergholtz, Non-Hermitian extensions of higher-order topological phases and their biorthogonal bulk-boundary correspondence, Physical Review B **99**, 081302 (2019).

[49] K.-I. Imura and Y. Takane, Generalized bulk-edge correspondence for non-Hermitian topological systems, Physical Review B **100**, 165430 (2019).

[50] L. Herviou, J. H. Bardarson, and N. Regnault, Defining a bulk-edge correspondence for non-Hermitian Hamiltonians via singular-value decomposition, Physical Review B **99**, 052118 (2019).

[51] X. Zhu, H. Wang, S. K. Gupta, H. Zhang, B. Xie, M. Lu, and Y. Chen, Photonic non-Hermitian skin effect and non-Bloch bulk-boundary correspondence, Physical Review Research **2**, 013280 (2020).

[52] Z. Yang, K. Zhang, C. Fang, and J. Hu, Non-Hermitian Bulk-Boundary Correspondence and Auxiliary Generalized Brillouin Zone Theory, Physical Review Letters **125**, 226402 (2020).

[53] D. S. Borgnia, A. J. Kruchkov, and R.-J. Slager, Non-Hermitian Boundary Modes and Topology, Physical Review Letters **124**, 056802 (2020).

[54] N. Okuma, K. Kawabata, K. Shiozaki, and M. Sato, Topological Origin of Non-Hermitian Skin Effects, Physical Review Letters **124**, 086801 (2020).

[55] K. Zhang, Z. Yang, and C. Fang, Correspondence Between Winding Numbers and Skin Modes in Non-Hermitian Systems, Physical Review Letters **125**, 126402 (2020).

[56] S. Longhi, Unraveling the non-Hermitian skin effect in dissipative systems, Physical Review B **102**, 201103 (2020).

[57] R. Okugawa, R. Takahashi, and K. Yokomizo, Second-order topological non-Hermitian skin effects, Physical Review B **102**, 241202 (2020).

[58] H.-G. Zirnstein, G. Refael, and B. Rosenow, Bulk-Boundary Correspondence for Non-Hermitian Hamiltonians via Green Functions, Physical Review Letters **126**, 216407 (2021).

[59] Y. Cao, Y. Li, and X. Yang, Non-Hermitian bulk-boundary correspondence in a periodically driven system, Physical Review B **103**, 075126 (2021).

[60] Q.-B. Zeng, Non-Hermitian skin effect edge, Physical Review B **106**, 235411 (2022).

[61] G. Hwang and H. Obuse, Bulk-edge correspondence for point-gap topological phases in junction systems, Physical Review B **108**, L121302 (2023).

[62] Z. Jiang, R. Okamoto, and H. Obuse, Dual symmetry classification of non-Hermitian systems and $\mathbb{Z}_2$ point-gap topology of a nonunitary quantum walk, Physical Review B **109**, 235408 (2024).

[63] Z. Jiang, M. Sato, and H. Obuse, Origin of robust $\mathbb{Z}_2$ topological phases in stacked Hermitian systems: Non-Hermitian level repulsion, Physical Review B **110**, 245404 (2024).

[64] N. Hatano and D. R. Nelson, Localization Transitions in Non-Hermitian Quantum Mechanics, Physical Review Letters **77**, 570 (1996).

[65] N. Hatano and D. R. Nelson, Vortex pinning and non-Hermitian quantum mechanics, Physical Review B **56**, 8651 (1997).

[66] N. Hatano and D. R. Nelson, Non-Hermitian delocalization and eigenfunctions, Physical Review B **58**, 8384 (1998).

[67] W. Wu, S. Rachel, W.-M. Liu, and K. Le Hur, Quantum spin Hall insulators with interactions and lattice anisotropy, Physical Review B **85**, 205102 (2012).

[68] Y. Xu, B. Yan, H.-J. Zhang, J. Wang, G. Xu, P. Tang, W. Duan, and S.-C. Zhang, Large-Gap Quantum Spin Hall Insulators in Tin Films, Physical Review Letters **111**, 136804 (2013).

[69] H. Zhao, C.-w. Zhang, W.-x. Ji, R.-w. Zhang, S.-s. Li, S.-s. Yan, B.-m. Zhang, P. Li, and P.-j. Wang, Unexpected giant-gap quantum spin Hall insulator in chemically decorated plumbene monolayer, Scientific Reports **6**, 20152 (2016).

[70] Z. Pedramrazi, C. Herbig, A. Pulkin, S. Tang, M. Phillips, D. Wong, H. Ryu, M. Pizzochero, Y. Chen, F. Wang, *et al.*, Manipulating Topological Domain Boundaries in The Single-Layer Quantum Spin Hall Insulator 1T′-WSe_2, Nano Letters **19**, 5634 (2019).

[71] N. Shumiya, M. S. Hossain, J.-X. Yin, Z. Wang, M. Litskevich, C. Yoon, Y. Li, Y. Yang, Y.-X. Jiang, G. Cheng, *et al.*, Evidence of a room-temperature quantum spin Hall edge state in a higher-order topological insulator, Nature Materials **21**, 1111 (2022).

[72] J. Zhong, M. Yang, Z. Shi, Y. Li, D. Mu, Y. Liu, N. Cheng, W. Zhao, W. Hao, J. Wang, *et al.*, Towards layer-selective quantum spin hall channels in weak topological insulator $Bi_4Br_2I_2$, Nature Communications **14**, 4964 (2023).

[73] C. Nayak, S. H. Simon, A. Stern, M. Freedman, and S. Das Sarma, Non-Abelian anyons and topological quantum computation, Reviews of Modern Physics **80**, 1083 (2008).

[74] S. Vijay, T. H. Hsieh, and L. Fu, Majorana Fermion Surface Code for Universal Quantum Computation, Physical Review X **5**, 041038 (2015).

[75] S. D. Sarma, M. Freedman, and C. Nayak, Majorana zero modes and topological quantum computation, npj Quantum Information **1**, 1 (2015).

[76] S.-B. Zhang, W. Rui, A. Calzona, S.-J. Choi, A. P. Schnyder, and B. Trauzettel, Topological and holonomic quantum computation based on second-order topological superconductors, Physical Review Research **2**, 043025 (2020).

[77] J. Sau and S. Tewari, Topological superconductivity in spin-orbit-coupled semiconducting nanowires, , in *Semiconductors and Semimetals*, Vol. 108 (Elsevier, 2021) pp. 125–194.

[78] J. v. Neumann, Thermodynamik quantenmechanischer Gesamtheiten Gött (1927).

[79] P. A. M. Dirac, *The Principles of Quantum Mechanics* (Oxford university press, 1981).

[80] J. Von Neumann, *Mathematical Foundations of Quantum Mechanics: New Edition*, Vol. 53 (Princeton university press, 2018).

[81] V. Gorini, A. Kossakowski, and E. C. G. Sudarshan, Completely positive dynamical semigroups of N-level systems, Journal of Mathematical Physics **17**, 821 (1976).

[82] G. Lindblad, On the generators of quantum dynamical semigroups, Communications in Mathematical Physics **48**, 119 (1976).

[83] B. L. Hu, J. P. Paz, and Y. Zhang, Quantum Brownian motion in a general environment: Exact master equation with nonlocal dissipation and colored noise, Physical Review D **45**, 2843 (1992).

[84] M. Born, Quantenmechanik der stoßvorgänge, Zeitschrift für physik **38**, 803 (1926).

[85] E. T. Jaynes and F. W. Cummings, Comparison of quantum and semiclassical radiation theories with application to the beam maser, Proceedings of the IEEE **51**, 89 (1963).

[86] H. Weimer, R. Löw, T. Pfau, and H. P. Büchler, Quantum Critical Behavior in Strongly Interacting Rydberg Gases, Physical Review Letters **101**, 250601 (2008).

[87] I. Carusotto and C. Ciuti, Quantum fluids of light, Reviews of Modern Physics **85**, 299 (2013).

[88] M. Mirhosseini, A. Sipahigil, M. Kalaee, and O. Painter, Superconducting qubit to optical photon transduction, Nature **588**, 599 (2020).

[89] G. Ithier, E. Collin, P. Joyez, P. Meeson, D. Vion, D. Esteve, F. Chiarello, A. Shnirman, Y. Makhlin, J. Schriefl, *et al.*, Decoherence in a superconducting quantum bit circuit, Physical Review B **72**, 134519 (2005).

[90] H. J. Kimble, The quantum internet, Nature **453**, 1023 (2008).

[91] T. Yu and J. Eberly, Sudden death of entanglement, Science **323**, 598 (2009).

[92] D. Gottesman, An introduction to quantum error correction and fault-tolerant quantum computation, , in *Quantum information science and its contributions to mathematics, Proceedings of Symposia in Applied Mathematics*, Vol. 68 (2010) pp. 13–58.

[93] E. Paladino, Y. Galperin, G. Falci, and B. Altshuler, 1/f noise: Implications for solid-state quantum information, Reviews of Modern Physics **86**, 361 (2014).

[94] S. Pirandola, R. Laurenza, C. Ottaviani, and L. Banchi, Fundamental limits of repeaterless quantum communications, Nature Communications **8**, 1 (2017).

[95] R. Lo Franco and G. Compagno, Indistinguishability of Elementary Systems as a Resource for Quantum Information Processing, Physical Review Letters **120**, 240403 (2018).

[96] C.-E. Bardyn, M. A. Baranov, C. V. Kraus, E. Rico, A. İmamoğlu, P. Zoller, and S. Diehl, Topology by dissipation, New Journal of Physics **15**, 085001 (2013).

[97] F. Lange, Z. Lenarčič, and A. Rosch, Pumping approximately integrable systems, Nature Communications **8**, 15767 (2017).

[98] M. Heyl, Dynamical quantum phase transitions: a review, Reports on Progress in Physics **81**, 054001 (2018).

[99] M. B. Plenio and P. L. Knight, The quantum-jump approach to dissipative dynamics in quantum optics, Reviews of Modern Physics **70**, 101 (1998).

[100] H. Carmichael, *An open systems approach to quantum optics: lectures presented at the Université Libre de Bruxelles, October 28 to November 4, 1991*, Vol. 18 (Springer Science & Business Media, 2009).

[101] C. M. Bender and S. Boettcher, Real Spectra in Non-Hermitian Hamiltonians Having $\mathcal{PT}$ Symmetry, Physical Review Letters **80**, 5243 (1998).

[102] H. Ramezani, T. Kottos, R. El-Ganainy, and D. N. Christodoulides, Unidirectional nonlinear PT-symmetric optical structures, Physical Review A **82**, 043803 (2010).

[103] L. Feng, Z. J. Wong, R.-M. Ma, Y. Wang, and X. Zhang, Single-mode laser by parity-time symmetry breaking, Science **346**, 972 (2014).

[104] H. Hodaei, A. U. Hassan, S. Wittek, H. Garcia-Gracia, R. El-Ganainy, D. N. Christodoulides, and M. Khajavikhan, Enhanced sensitivity at higher-order exceptional points, Nature **548**, 187 (2017).

[105] X. Zhu, H. Ramezani, C. Shi, J. Zhu, and X. Zhang, PT-Symmetric Acoustics, Physical Review X **4**, 031042 (2014).

[106] R. Fleury, D. L. Sounas, and A. Alu, Parity-time symmetry in acoustics: theory, devices, and potential applications, IEEE Journal of Selected Topics in Quantum Electronics **22**, 121 (2016).

[107] J. Schindler, A. Li, M. C. Zheng, F. M. Ellis, and T. Kottos, Experimental study of active LRC circuits with PT symmetries, Physical Review A **84**, 040101 (2011).

[108] J. Schindler, Z. Lin, J. Lee, H. Ramezani, F. M. Ellis, and T. Kottos, $\mathcal{PT}$-symmetric electronics, Journal of Physics A: Mathematical and Theoretical **45**, 444029 (2012).

[109] W. D. Heiss, The physics of exceptional points, Journal of Physics A: Mathematical and Theoretical **45**, 444016 (2012).

[110] X.-L. Zhang, S. Wang, B. Hou, and C. T. Chan, Dynamically Encircling Exceptional Points: in Situ Control of Encircling Loops and The Role of the Starting Point, Physical Review X **8**, 021066 (2018).

[111] K. Kawabata, T. Bessho, and M. Sato, Classification of Exceptional Points and Non-Hermitian Topological Semimetals, Physical Review Letters **123**, 066405 (2019).

[112] W. Chen, Ş. Kaya Özdemir, G. Zhao, J. Wiersig, and L. Yang, Exceptional points enhance sensing in an optical microcavity, Nature **548**, 192 (2017).

[113] J. Doppler, A. A. Mailybaev, J. Böhm, U. Kuhl, A. Girschik, F. Libisch, T. J. Milburn, P. Rabl, N. Moiseyev, and S. Rotter, Dynamically encircling an exceptional point for asymmetric mode switching, Nature **537**, 76 (2016).

[114] R. Thomas, H. Li, F. M. Ellis, and T. Kottos, Giant nonreciprocity near exceptional-point degeneracies, Physical Review A **94**, 043829 (2016).

[115] T. Li, Z. Gao, and K. Xia, Nonlinear-dissipation-induced nonreciprocal exceptional points, Optics Express **29**, 17613 (2021).

[116] A. Laha, A. Miranowicz, R. Varshney, and S. Ghosh, Correlated nonreciprocity around conjugate exceptional points, Physical Review A **109**, 033511 (2024).

[117] F. Bloch, Zur theorie des ferromagnetismus, Zeitschrift für Physik **61**, 206 (1930).

[118] J. Van Vleck, On the theory of antiferromagnetism, The Journal of Chemical Physics **9**, 85 (1941).

[119] T. Nagamiya, K. Yosida, and R. Kubo, Antiferromagnetism, Advances in Physics **4**, 1 (1955).

[120] J. Goldstone, A. Salam, and S. Weinberg, Broken Symmetries, Physical Review **127**, 965 (1962).

[121] L. P. Gor'kov and G. Grüner, *Charge density waves in solids* (Elsevier, 2012).

[122] D. J. Thouless, M. Kohmoto, M. P. Nightingale, and M. den Nijs, Quantized Hall Conductance in A Two-Dimensional Periodic Potential, Physical Review Letters **49**, 405 (1982).

[123] F. Bloch, Über die quantenmechanik der elektronen in kristallgittern, Zeitschrift für physik **52**, 555 (1929).

[124] R. d. L. Kronig and W. G. Penney, Quantum mechanics of electrons in crystal lattices, Proceedings of the royal society of London. series A, containing papers of a mathematical and physical character **130**, 499 (1931).

[125] H. Jones and N. Chako, The theory of Brillouin zones and electronic states in crystals, Physics Today **15**, 66 (1962).

[126] N. F. Mott, The electrical conductivity of transition metals, Proceedings of the Royal Society of London. Series A-Mathematical and Physical Sciences **153**, 699 (1936).

[127] M. V. Berry, Quantal phase factors accompanying adiabatic changes, Proceedings of the Royal Society of London. A. Mathematical and Physical Sciences **392**, 45 (1984).

[128] S. Pancharatnam, Generalized theory of interference, and its applications: Part I. Coherent pencils, , in *Proceedings of the Indian Academy of Sciences-Section A*, Vol. 44 (Springer, 1956) pp. 247–262.

[129] D. Xiao, M.-C. Chang, and Q. Niu, Berry phase effects on electronic properties, Reviews of Modern Physics **82**, 1959 (2010).

[130] B. Bradlyn and M. Iraola, Lecture notes on Berry phases and topology, SciPost Physics Lecture Notes , 051 (2022).

[131] C. Yin, H. Jiang, L. Li, R. Lü, and S. Chen, Geometrical meaning of winding number and its characterization of topological phases in one-dimensional chiral non-Hermitian systems, Physical Review A **97**, 052115 (2018).

[132] B. Zhu, Y. Ke, H. Zhong, and C. Lee, Dynamic winding number for exploring band topology, Physical Review Research **2**, 023043 (2020).

[133] L. Lin, Y. Ke, and C. Lee, Real-space representation of the winding number for a one-dimensional chiral-symmetric topological insulator, Physical Review B **103**, 224208 (2021).

[134] A. Rajabpoor Alisepahi, S. Sarkar, K. Sun, and J. Ma, Breakdown of conventional winding number calculation in one-dimensional lattices with interactions beyond nearest neighbors, Communications Physics **6**, 334 (2023).

[135] B. Zhu, Z. Tan, Y. Ke, and H. Zhong, Dynamic winding number for Floquet topological insulators with arbitrarily driving frequencies, Physical Review B **109**, 224315 (2024).

[136] Y. Hatsugai, Chern Number and Edge States in The Integer Quantum Hall Effect, Physical Review Letters **71**, 3697 (1993).

[137] F. D. M. Haldane, Nobel lecture: Topological quantum matter, Reviews of Modern Physics **89**, 040502 (2017).

[138] C. Sun, A. Chen, T. Bzdusek, and J. Maciejko, Topological linear response of hyperbolic Chern insulators, SciPost Physics **17**, 124 (2024).

[139] Y. Hatsugai, Edge states in the integer quantum Hall effect and the Riemann surface of the Bloch function, Physical Review B **48**, 11851 (1993).

[140] W. P. Su, J. R. Schrieffer, and A. J. Heeger, Solitons in Polyacetylene, Physical Review Letters **42**, 1698 (1979).

[141] E. J. Meier, F. A. An, and B. Gadway, Observation of the topological soliton state in the Su–Schrieffer–Heeger model, Nature communications **7**, 13986 (2016).

[142] D. Xie, W. Gou, T. Xiao, B. Gadway, and B. Yan, Topological characterizations of an extended Su–Schrieffer–Heeger model, npj Quantum Information **5**, 55 (2019).

[143] S. Mandal and S. Kar, Topological solitons in a Su-Schrieffer-Heeger chain with periodic hopping modulation, domain wall, and disorder, Physical Review B **109**, 195124 (2024).

[144] E. Noether, Invariante variationsprobleme, , in *Gesammelte Abhandlungen-Collected Papers* (Springer, 1983) pp. 231–239.

[145] J. Hanc, S. Tuleja, and M. Hancova, Symmetries and conservation laws: Consequences of Noether's theorem, American Journal of Physics **72**, 428 (2004).

[146] A. Altland and M. R. Zirnbauer, Nonstandard symmetry classes in mesoscopic normal-superconducting hybrid structures, Physical Review B **55**, 1142 (1997).

[147] A. P. Schnyder, S. Ryu, A. Furusaki, and A. W. Ludwig, Classification of topological insulators and superconductors in three spatial dimensions, Physical Review B **78**, 195125 (2008).

[148] S. Yao and Z. Wang, Edge States and Topological Invariants of Non-Hermitian Systems, Physical Review Letters **121**, 086803 (2018).

[149] K. Yokomizo and S. Murakami, Non-Bloch Band Theory of Non-Hermitian Systems, Physical Review Letters **123**, 066404 (2019).

[150] K. Kawabata, N. Okuma, and M. Sato, Non-Bloch band theory of non-Hermitian Hamiltonians in the symplectic class, Physical Review B **101**, 195147 (2020).

[151] M. Kawasaki, K. Mochizuki, N. Kawakami, and H. Obuse, Bulk-edge correspondence and stability of multiple edge states of a $\mathcal{PT}$-symmetric non-Hermitian system by using non-unitary quantum walks, Progress of Theoretical and Experimental Physics **2020**, 12A105 (2020).

[152] C.-H. Liu, H. Hu, and S. Chen, Symmetry and topological classification of Floquet non-Hermitian systems, Physical Review B **105**, 214305 (2022).

[153] J. Cayssol, B. Dóra, F. Simon, and R. Moessner, Floquet topological insulators, physica status solidi (RRL)–Rapid Research Letters **7**, 101 (2013).

[154] S. Afzal, T. J. Zimmerling, Y. Ren, D. Perron, and V. Van, Realization of Anomalous Floquet Insulators in Strongly Coupled Nanophotonic Lattices, Physical Review Letters **124**, 253601 (2020).

[155] J. Lu, L. He, Z. Addison, E. J. Mele, and B. Zhen, Floquet Topological Phases in One-Dimensional Nonlinear Photonic Crystals, Physical Review Letters **126**, 113901 (2021).

[156] L. Zhou and D.-J. Zhang, Non-Hermitian Floquet Topological Matter—A Review, Entropy **25**, 1401 (2023).

[157] K. Shi, X. Zhang, and W. Zhang, Floquet topological phases with large winding number, Physical Review A **109**, 013324 (2024).

[158] K. Mochizuki, D. Kim, and H. Obuse, Explicit definition of $\mathcal{PT}$ symmetry for nonunitary quantum walks with gain and loss, Physical Review A **93**, 062116 (2016).

[159] L. Xiao, X. Zhan, Z. H. Bian, K. K. Wang, X. Zhang, X. P. Wang, J. Li, K. Mochizuki, D. Kim, N. Kawakami, W. Yi, H. Obuse, B. C. Sanders, and P. Xue, Observation of topological edge states in parity–time-symmetric quantum walks, Nature Physics **13**, 1117–1123 (2017).

[160] K. Mochizuki, D. Kim, N. Kawakami, and H. Obuse, Bulk-edge correspondence in nonunitary Floquet systems with chiral symmetry, Physical Review A **102**, 062202 (2020).

[161] L. Xiao, T. Deng, K. Wang, G. Zhu, Z. Wang, W. Yi, and P. Xue, Non-Hermitian bulk-boundary correspondence in quantum dynamics, Nature Physics **16**, 761 (2020).

[162] M. Yamagishi, N. Hatano, and H. Obuse, Proposal of a quantum version of active particles via a nonunitary quantum walk, Scientific Reports **14**, 28648 (2024).

[163] Y. Aharonov, L. Davidovich, and N. Zagury, Quantum random walks, Physical Review A **48**, 1687 (1993).

[164] B. Tregenna, W. Flanagan, R. Maile, and V. Kendon, Controlling discrete quantum walks: coins and initial states, New Journal of Physics **5**, 83 (2003).

[165] C. M. Chandrashekar, R. Srikanth, and R. Laflamme, Optimizing the discrete time quantum walk using a SU(2) coin, Physical Review A **77**, 032326 (2008).

[166] N. B. Lovett, S. Cooper, M. Everitt, M. Trevers, and V. Kendon, Universal quantum computation using the discrete-time quantum walk, Physical Review A **81**, 042330 (2010).

[167] A. Schreiber, K. N. Cassemiro, V. Potoček, A. Gábris, P. J. Mosley, E. Andersson, I. Jex, and C. Silberhorn, Photons Walking The Line: A Quantum Walk with Adjustable Coin Operations, Physical Review Letters **104**, 050502 (2010).

[168] J. K. Asbóth and H. Obuse, Bulk-boundary correspondence for chiral symmetric quantum walks, Physical Review B **88**, 121406 (2013).

[169] M. Yamagishi, N. Hatano, K.-I. Imura, and H. Obuse, Proposal of multidimensional quantum walks to explore Dirac and Schrödinger systems, Physical Review A **107**, 042206 (2023).

[170] S. Dadras, A. Gresch, C. Groiseau, S. Wimberger, and G. S. Summy, Experimental realization of a momentum-space quantum walk, Physical Review A **99**, 043617 (2019).

[171] B. A. Bernevig and S.-C. Zhang, Quantum Spin Hall Effect, Physical Review Letters **96**, 106802 (2006).

[172] H. Obuse, A. Furusaki, S. Ryu, and C. Mudry, Two-dimensional spin-filtered chiral network model for the Z_2 quantum spin-Hall effect, Physical Review B **76**, 075301 (2007).

[173] L. Fu and C. L. Kane, Josephson current and noise at a superconductor/quantum-spin-Hall-insulator/superconductor junction, Physical Review B **79**, 161408 (2009).

[174] M. Hohenadler, T. Lang, and F. Assaad, Correlation Effects in Quantum Spin-Hall Insulators: A Quantum Monte Carlo Study, Physical Review Letters **106**, 100403 (2011).

[175] Y. Liu, Z. Wang, T. Sato, M. Hohenadler, C. Wang, W. Guo, and F. F. Assaad, Superconductivity from the condensation of topological defects in a quantum spin-Hall insulator, Nature Communications **10**, 2658 (2019).

[176] C. L. Wong and K. T. Law, Majorana Kramers doublets in $d_{x^2-y^2}$-wave superconductors with Rashba spin-orbit coupling, Physical Review B **86**, 184516 (2012).

[177] J. C. Budich and E. Ardonne, Topological invariant for generic one-dimensional time-reversal-symmetric superconductors in class DIII, Physical Review B **88**, 134523 (2013).

[178] C. Reeg, C. Schrade, J. Klinovaja, and D. Loss, DIII topological superconductivity with emergent time-reversal symmetry, Physical Review B **96**, 161407 (2017).

[179] A. Y. Kitaev, Unpaired Majorana fermions in quantum wires, Physics-uspekhi **44**, 131 (2001).

[180] B. Zhou and S.-Q. Shen, Crossover from Majorana edge-to end-states in quasi-one-dimensional p-wave superconductors, Physical Review B **84**, 054532 (2011).

[181] J. C. Budich and E. Ardonne, Equivalent topological invariants for one-dimensional Majorana wires in symmetry class D, Physical Review B **88**, 075419 (2013).

[182] K. Esaki, M. Sato, K. Hasebe, and M. Kohmoto, Edge states and topological phases in non-Hermitian systems, Physical Review B **84**, 205128 (2011).

[183] M. Sato, K. Hasebe, K. Esaki, and M. Kohmoto, Time-Reversal Symmetry in Non-Hermitian Systems, Progress of Theoretical Physics **127**, 937 (2012).

[184] A. Ghatak and T. Das, New topological invariants in non-Hermitian systems, Journal of Physics: Condensed Matter **31**, 263001 (2019).

[185] J. Cai, E. Anderson, C. Wang, X. Zhang, X. Liu, W. Holtzmann, Y. Zhang, F. Fan, T. Taniguchi, K. Watanabe, *et al.*, Signatures of fractional quantum anomalous Hall states in twisted $MoTe_2$, Nature **622**, 63 (2023).

[186] B. Rasche, A. Isaeva, M. Ruck, S. Borisenko, V. Zabolotnyy, B. Büchner, K. Koepernik, C. Ortix, M. Richter, and J. Van Den Brink, Stacked topological insulator built from bismuth-based graphene sheet analogues, Nature Materials **12**, 422 (2013).

[187] J.-i. Inoue, Electromagnetic waves in a topological insulator thin film stack: helicon-like wave mode and photonic band structure, Optics Express **21**, 21317 (2013).

[188] S. K. Das, B. Yan, J. van den Brink, and I. C. Fulga, Topological crystalline insulators from stacked graphene layers, Physical Review B **99**, 165418 (2019).

[189] X. Li, X. Xu, H. Zhou, H. Jia, E. Wang, H. Fu, J.-T. Sun, and g. Meng, Tunable Topological States in Stacked Chern Insulator Bilayers, Nano Letters **23**, 2839 (2023).

[190] K. Kobayashi, Y. Yoshimura, K.-I. Imura, and T. Ohtsuki, Dimensional crossover of transport characteristics in topological insulator nanofilms, Physical Review B **92**, 235407 (2015).

[191] Y. Yoshimura, W. Onishi, K. Kobayashi, T. Ohtsuki, and K.-I. Imura, Comparative study of Weyl semimetal and topological/Chern insulators: Thin-film point of view, Physical Review B **94**, 235414 (2016).

[192] J. Feinberg and A. Zee, Non-hermitian random matrix theory: Method of hermitian reduction, Nuclear Physics B **504**, 579 (1997).

[193] L. Fu, C. L. Kane, and E. J. Mele, Topological Insulators in Three Dimensions, Physical Review Letters **98**, 106803 (2007).

[194] Z. Ringel, Y. E. Kraus, and A. Stern, Strong side of weak topological insulators, Physical Review B **86**, 045102 (2012).

[195] K. Kobayashi, T. Ohtsuki, and K.-I. Imura, Disordered Weak and Strong Topological Insulators, Physical Review Letters **110**, 236803 (2013).

Achievements of the Author

(A) **Journal**

[**A-1**] Z. Jiang, R. Okamoto, and H. Obuse, "Dual symmetry classification of non-Hermitian systems and $\mathbb{Z}_2$ point-gap topology of a nonunitary quantum walk", *Physical Review B*, **109**, 235408 (2024).

[**A-2**] Z. Jiang, M. Sato, and H. Obuse, "Origin of robust $\mathbb{Z}_2$ topological phases in stacked Hermitian systems: Non-Hermitian level repulsion", *Physical Review B*, **110**, 245404 (2024).

(B) **International Conference**

[**B-1**] Z. Jiang, and H. Obuse, "Point-Gap Topology of a Non-unitary Quantum Walk with Time-Reversal Symmetry", in *Physics of Open Systems and Beyond*, Sapporo, Japan, 2023.

[**B-2**] Z. Jiang, and H. Obuse, "$\mathbb{Z}_2$ point-gap topology of a non-unitary quantum walk with time-reversal symmetry", in *10th International Workshop of Quantum Simulation and Quantum Walks*, Tsukuba, Japan, 2023.

[**B-3**] Z. Jiang, and H. Obuse, "$\mathbb{Z}_2$ point-gap topology of a non-unitary quantum walk with time-reversal symmetry", in *95th RIKEN Quantum Computing Seminar*, Wako, Japan, 2023.

[**B-4**] Z. Jiang, and H. Obuse, "$\mathbb{Z}_2$ point-gap topology of a non-unitary quantum walk with time-reversal symmetry", in *Quantum Innovation 2023*, Tokyo, Japan, 2023.

[**B-5**] Z. Jiang, M. Sato, and H. Obuse, "Origin of Robust $\mathbb{Z}_2$ Topological Phases in Stacked Hermitian system: Non-Hermitian Level Repulsion", in *Workshop Non-Hermitian 2024*, Kashiwa, Japan, 2024.

[**B-6**] Z. Jiang, G. Hwang, and H. Obuse, "Dual symmetry classification of non-Hermitian systems and point-gap topology", in *META 2024*, Toyama, Japan, 2024.

[**B-7**] Z. Jiang, R. Okamoto, M. Sato, and H. Obuse, "Dual symmetry classification of non-Hermitian systems and $\mathbb{Z}_2$ point-gap topology of a nonunitary quantum walk", in *The 8th International Coference on Quantum Information, Spacetime Simulation, and Topological State of Matter*, Dalian, China, 2024.

[**B-8**] Z. Jiang, R. Okamoto, M. Sato, and H. Obuse, "Dual symmetry classification of non-Hermitian systems and $\mathbb{Z}_2$ point-gap topology of a nonunitary quantum walk", in *New Frontiers in Advanced Magnetism 2024*, Sapporo, Japan, 2024.

(C) Domestic Conference

[**C-1**] 黄 健輝, 姜 治宇, 小布施 秀明, "非エルミート・トポロジカル相と Julia による任意精度演算", 物性研究所スパコン共同利用・CCMS 合同研究会「計算の時代における物性科学」, 柏, 2023.

[**C-2**] 姜 治宇, 小布施 秀明, "時間反転対称な非ユニタリー量子ウォークのポイントギャップ・トポロジカル相", 日本物理学会第 78 回年次大会 (2023 年）, 仙台, 2023.

[**C-3**] 姜 治宇, 佐藤 昌利, 小布施 秀明, "Non-Trivial Topological Phase Induced by Stacking $\mathbb{Z}_2$ Point-Gap Systems", 2024 年春季大会, オンライン, 2024.

[**C-4**] 姜 治宇, 佐藤 昌利, 小布施 秀明, "エルミート系 $\mathbb{Z}_2$ トポロジカル相の積層に対する安定性の起源：非エルミート系準位反発", 日本物理学会第 78 回年次大会 (2024 年）, 札幌, 2024.

(D) Scholarship and Awards

[**D-1**] Hokkaido University DX Doctoral Fellowship, 2022.

[**D-2**] Hokkaido University EXEX Doctoral Fellowship, 2024.

[**D-3**] Third Prize in Poster Presentation at QuIST-VIII Conference, 2024.